Chapter 1 Introduction

1.1 Overview

Solid acid fuel cells (SAFCs) based on CsH_2PO_4 electrolyte membranes have the unique advantage of operating at warm temperatures near 250 ºC. They were first demonstrated in the laboratory in 2004[1] and today have been scaled to stacks of 1.4 kW.[2] Despite the rapid development of SAFCs, durability and cost, both of which pertain to the performance of the electrodes, are the key challenges which must be overcome in order for SAFCs to become technologically relevant.[3] Thus, the overall objective of this work is to gain a fundamental understanding of electrochemical pathways in SAFCs using model electrode systems and newly developed characterization tools.

In this chapter, we present a brief introduction of fuel cells and, in particular, the current status of SAFCs. We describe the basics of electrocatalysis in solid state electrochemical systems and how an improved understanding of electrochemical reaction kinetics can drastically advance the SAFC technology.

1.2 Fuel Cells

The need for clean, reliable and secure energy is one of the most important challenges of this century. As such, many technologies are being pursued to address this challenge. Among these, fuel cells stand to play a significant role in any renewable energy cycle because they can efficiently convert fuels to electricity. Fuel cells are devices that combine the advantages of both combustion engines and batteries. Like combustion engines, they intake fuel continuously without a need to recharge, but like batteries, they convert chemical energy directly to electricity. Consequently, fuel cells can operate with higher efficiencies and lower emissions of greenhouse gases per unit of fuel input compared to combustion engines which are limited by the Carnot efficiency. Furthermore, they have no moving parts so they are silent during operation and have the potential to operate with longer lifetimes. Finally, it has been shown that fuel cells can be scaled up to large sizes without loss in power density. Due to these advantages, fuel cells have been pursued for decades for both mobile and stationary power generation.

1.2.1 Fuel Cell Basics

A simple schematic of a fuel cell, based on a proton-conducting electrolyte, is shown in Figure 1.1. For a fuel cell operating on hydrogen as the fuel and oxygen as oxidant, the driving force for conversion of energy is the Gibbs free energy of the reaction,

$$2H_{2(g)} + O_{2(g)} \rightarrow 2H_2O_{(g)} \tag{1.1}$$

The direct reaction of hydrogen and oxygen gases cannot occur because a gas-impermeable membrane separates the two reactants. In order to utilize the energy stored in the chemical bonds, electrochemical reactions occur at the electrodes and the resulting ions (protons in this case) are transported through the electrolyte membrane, with concurrent electron transport through an external circuit to do useful work. Specifically, at the anode, hydrogen is electrochemically oxidized to protons and electrons, while at the cathode, oxygen is electrochemically reduced to form water. The half-cell reactions for a proton-conducting electrolyte are:

$$\text{anode:} \quad 2\mathrm{H}_{2(\mathrm{g})} \rightarrow 4\mathrm{H}^{+} + 4\mathrm{e}^{-} \tag{1.2}$$

$$\text{cathode:} \quad \mathrm{O}_{2(\mathrm{g})} + 4\mathrm{H}^{+} + 4\mathrm{e}^{-} \rightarrow 2\mathrm{H}_2\mathrm{O}_{(\mathrm{g})} \tag{1.3}$$

The two half-cell reactions, (1.2) and (1.3), sum to the net reaction (1.1). The standard Gibbs free energy of the reaction, ΔG°_{rxn}, as written in Equation (1.1), is –483 kJ mol^{-1} at 25 ºC, where the superscript "o" refers to standard conditions of 1 atm of the reactants and products.

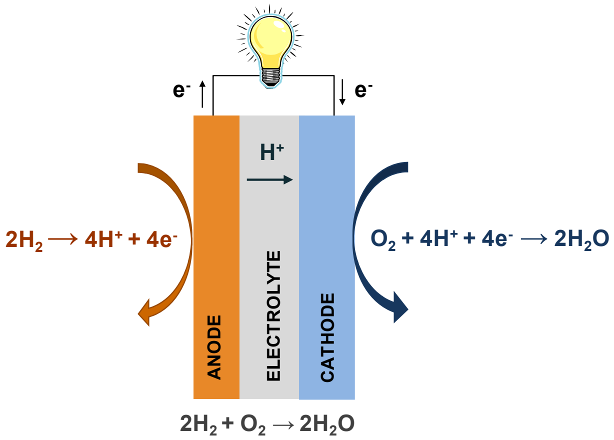

Figure 1.1 A simple schematic of a fuel cell based on a proton-conducting electrolyte membrane.

This chemical potential driving force for water formation, ΔG°_{rxn}, can be related to the electrochemical potential via the relation

$$E^{\circ}(T) = -\frac{\Delta G^{\circ}_{rxn}(T)}{nF} \tag{1.4}$$

where E° is the standard Nernst potential of the fuel cell (or the theoretical open-circuit voltage), n denotes the number of electrons transferred in the reaction (e.g., $n = 4$ in this case), and F is the Faraday constant (96,485 C mol^{-1}). The standard Nernst potential corresponding to Equations (1.1)–(1.3) can be computed to be 1.25 V. To compute the Nernst potential at more realistic conditions, one can readily show that

$$E_{eq}\left(T\right)=E^{\circ}\left(T\right)-\frac{RT}{nF}\ln\frac{p_{H_2O}^{2(c)}}{p_{H_2}^{2(a)}\,p_{O_2}^{(c)}} \tag{1.5}$$

where E_{eq} is the equilibrium/theoretical Nernst potential, p_i is the partial pressure of species i at the anode (a) or cathode (c), and R and T have their usually meanings. Values for $\Delta G_{rxn}^{\circ}\left(T\right)$ are tabulated for various reactions (or can be computed from the formation energies for the reactants and products).

1.2.2 Overpotentials in Fuel Cells

Fuel cells are evaluated by their power output, and therefore it is desirable to maintain a high cell voltage under large current loads. However, the voltage across a fuel cell during operation is less than that predicted by the Nernst voltage because of irreversible losses as current is drawn from the cell. Figure 1.2 is a schematic of representative polarization and power density curves and depicts the four common sources of voltage losses, or overpotentials. The overpotential, η_i, is best described as a drop in voltage (from equilibrium) which is used to drive a specific process. The cell voltage at any current density, j, can be expressed as

$$E\left(j\right)=E_{eq}-\eta_{L}-\eta_{act}-\eta_{iR}-\eta_{D} \tag{1.6}$$

η_L is the voltage loss due to gas leaks across the electrolyte or partial electronic conductivity of the electrolyte. η_{act} is the activation overpotential due to slow kinetics at the electrodes, that is, the driving force required to push reactions over its activation barrier. η_{iR} is the overpotential due to ohmic resistances, primarily from ion transport through the electrolyte, and is characterized by a linear regime in the polarization curve. At high currents, a drop in the cell voltage is characteristic of mass transport losses, η_D, for example, due to the depletion of reactants at the electrodes faster than they can be supplied. The ultimate goal is to minimize all the overpotentials and shift the polarization curve toward E_{eq}.

The relative contribution of each overpotential in Equation (1.6) and how it varies with current density depend on the fuel cell type and the materials used therein. For example, low-temperature fuel cells typically have large activation overpotentials while high temperature fuel cells such as SOFCs have a larger contribution from ohmic loss and cross-over.

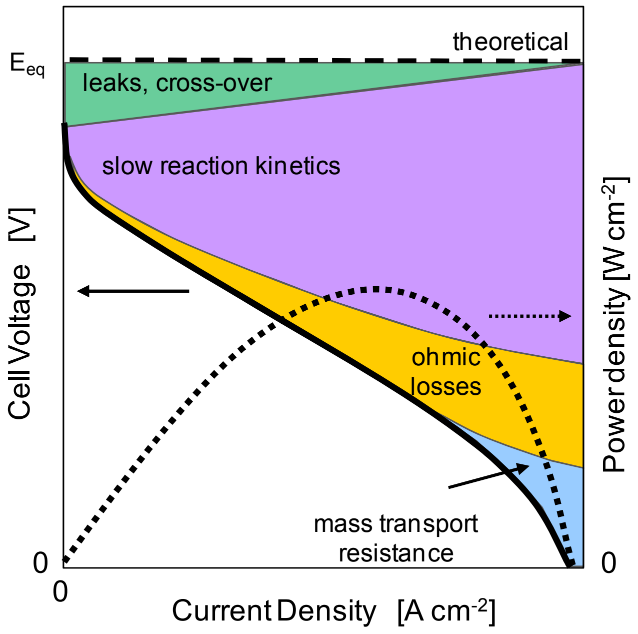

Figure 1.2 Schematic of a fuel cell polarization curve, with contributions of various overpotentials as indicated by the shaded regions. The power density (dotted line) is the product of the cell voltage and current density.

1.2.3 Component Requirements

In order to maintain a sufficiently high power density, or a sufficiently high cell voltage, for a given current density (Figure 1.2), it is necessary to minimize overpotentials. Cross-over effects can be reduced by an appropriate choice of the electrolyte material, specifically one with minimal-to-no electronic conductivity, and by optimizing its fabrication so as to obtain high density membranes with low porosity. Proper sealing of the anode and cathode chambers is also required.

The thickness of the membrane should be reduced so as to minimize the total voltage loss due to ion conduction since

$$\eta_{iR} = jR = j\frac{L}{\sigma_H} \tag{1.7}$$

where L is the membrane thickness and σ_{H} is the proton conductivity. In cases where the electrolyte membrane must be very thin, the cell is fabricated to be electrode-supported, meaning that either the anode or cathode is fabricated to be the structural support of the assembly.

The activation overpotential is related to the rate at which the half-cell reactions can occur at the electrodes and is often expressed as

$$\eta_{act} \approx \frac{RT}{\alpha nF}\ln\left(\frac{j}{j_0}\right) \tag{1.8}$$

where j_0 is the exchange current density which flows under zero overpotential, and α is termed the exchange coefficient, an indicator of the electrochemical activity under non-equilibrium conditions (i.e., at non-zero overpotentials). Equation (1.8) describes how much voltage is required to attain a specific electrochemical current flow at the electrodes. If the activity of the electrode is high, less driving force, or overpotential, is required to attain sufficient currents. From the equation, one can see that larger values of j_0 and α are desirable for lowering η_{act}. The exchange current density, which is usually normalized by the macroscopic electrode area, can be improved by increasing the number of active sites per electrode area or by improving the intrinsic activity of the electrode. On the other hand, the exchange coefficient is geometry-independent and can only be affected by changing material properties. The derivation of Equation (1.8) is detailed in Appendix A.1.

The requirements for electrodes are arguably more demanding than those for the electrolyte membrane. Because electrochemical reactions involve gas phase species, electrons and ions, electrodes are required to transport each of these species. That is, to minimize activation losses, η_{act}, electrodes must not only be catalytically active, as discussed in the previous paragraph, but must also transport participating electrons and ions to and from active sites. Furthermore, they must have sufficient porosity to reduce mass transport losses, η_D. More often than not, one material cannot satisfy all of these requirements, so a porous composite of electrolyte and (metal) catalyst particles is typically employed as the electrode (Figure 1.3). Typically, the electrolyte and catalyst are pure ion- and electron-conductors, respectively, and thus the locations at which these two solid phases come together to meet the gas phase are critical; the site at which these three phases meet is termed the triple-phase boundary (TPB). Thus, the ideal electrode structure requires interconnected ionic, electronic and gas pathways while maximizing the number of triple-phase boundary sites. Any catalyst or electrolyte particle that is isolated from its own network will not contribute to the total electrochemical current.

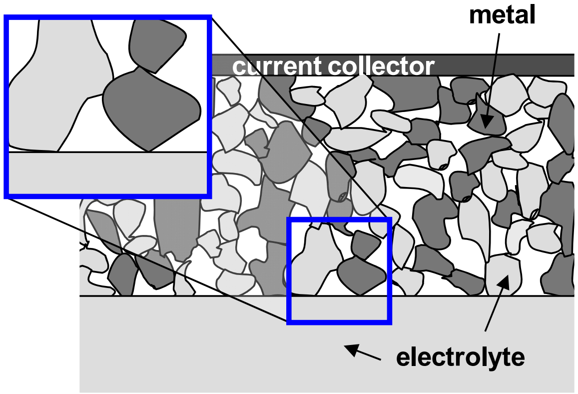

Figure 1.3 Schematic of a typical composite electrode comprised of electrolyte and catalyst/electronically-conducting particles in a porous network. Enlargement shows a triple-phase boundary site, with the electrolyte particle connected to the electrolyte membrane and the metal/catalyst particle connected to a neighboring particle (and out to the current collector).

1.2.4 Types of Fuel Cells

Several different types of fuel cells, with operating temperatures ranging from room temperature up to as high as 1000 ºC, are being actively pursued today. The operating temperature of a fuel cell is dictated by that required to attain sufficiently high ionic conductivity in the electrolyte, and thus, different fuel cell types are distinguished by their electrolytes. Table 1.1 shows a brief summary of the common fuel cells and their general characteristics. A good overview of the different types of fuel cells can be found in a review article by Carrette et al.[4] A more thorough reference is a text book by Larminie and Dicks.[5]

Table 1.1 Common types of fuel cells and their primary characteristics.[4, 5]

Fuel Cell Type	**Oper. Temp. [ºC]**	**Electrolyte**	**Mobile Ion**	**Fuel**
PEMFC polymer electrolyte membrane fuel cell proton exchange membrane fuel cell	70–110	sulfonated polymers	H_3O^+	H_2 CH_3OH
AFC alkali fuel cell	100–250	$(Na,K)OH_{(aq)}$	OH^-	H_2
PAFC phosphoric acid fuel cell	150–220	H_3PO_4	H^+	H_2
MCFC molten carbonate fuel cell	500–700	$(Na,K)_2CO_3$	CO_3^{2-}	hydrocarbons CO
SOFC solid oxide fuel cells	700–1000	$(Zr,Y)O_{2-\delta}$	O^{2-}	hydrocarbons CO

In general, operation at high temperatures improves fuel flexibility, reducing reliance on hydrogen gas as the primary fuel, and increases the efficiency of fuel cells due to faster reaction kinetics at the electrodes. However, at temperatures close to 1000 ºC, material compatibility between supporting components becomes a problem, and repeated thermal cycling is often not possible. Consequently, high temperature fuel cells, such as solid oxide fuel cells (SOFCs) and molten carbonate fuel cells (MCFCs), are typically employed for stationary power generation. At lower temperatures, rapid thermal cycling is possible, as indicated by the demonstration of fuel cell vehicles based on polymer electrolyte membrane fuel cells (PEMFCs), but operation with sufficient power output requires the use of expensive catalysts such as platinum. At intermediate temperatures, the benefits of both improved reaction kinetics and ease of thermal cycling are retained; however, fuel cells operating at these temperatures are based on corrosive liquid electrolytes. While liquid electrolytes have the benefit of high ionic conductivities, they also can cause the dissolution of catalysts, resulting in reduced activity.

Consequently, substantial effort in the fuel cell community has been directed towards lowering the temperature of operation of SOFCs to 400–600 ºC (called intermediate temperature solid oxide fuel cells, ITSOFCs) via the research and development of electrolyte and electrode materials with sufficient ionic conductivities and electrocatalytic activities at lower temperatures. A recently discovered class of fuel cells which operate in this preferred intermediate temperature range is solid acid fuel cells, the subject of this work.

1.3 Solid Acid Fuel Cells

1.3.1 Solid Acid Compounds

A relatively new addition to the fuel cell community is the solid acid fuel cell (SAFC), first demonstrated in 2001 and operable at warm temperatures of 100–300 ºC, depending on the solid acid electrolyte. Solid acid compounds have physical and chemical similarities to normal salts and normal acids; they dissolve in water like common salts but are able to donate acidic protons like typical acids. Common stoichiometries are $MHXO_4$, MH_2XO_4 and $M_3H(XO_4)_2$ where M can be Cs, Rb, K, Na, and even NH_4, and X can be P, S, Se, and As. Typical room temperature structures of solid acids consist of hydrogen-bonded XO_4 groups, with the dimensionality of the hydrogen bonding network being dictated by the H:XO_4 ratio. On heating to warm temperatures of ~ 100–300 ºC, a subset of these compounds undergo a phase transition to a high temperature disordered phase at which the proton conductivity is increased by several orders of magnitude. Since discovery of this phenomenon for $CsHSO_4$ and

$CsHSeO_4$ in 1982,[6] the so-called superprotonic transition has been identified in additional solid acid compounds, such as $Rb_3H(SeO_4)_2$,[7] $(NH_4)_3H(SO_4)_2$,[8] $Cs_2(HSO_4)(H_2PO_4)$,[9] CsH_2PO_4,[10] and even $CsHPO_3H$[11] (Figure 1.4).

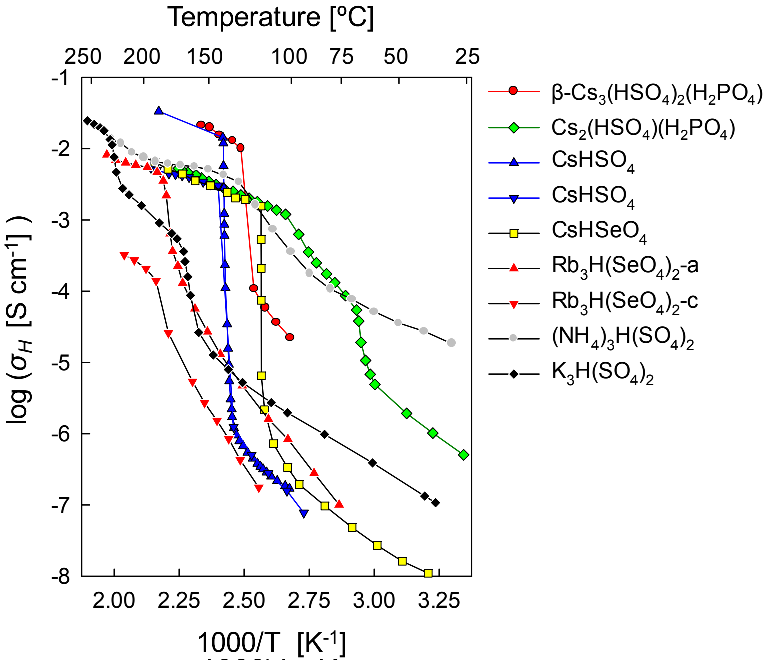

Figure 1.4 The proton conductivity, σ_H, of several solid acid compounds observed to exhibit a superprotonic phase transition, after Haile et al.[12] and references therein.

Presently, among the solid acid compounds known to have a superprotonic phase transformation, CsH_2PO_4 is the most promising as a fuel cell electrolyte.[3, 10] On heating, CsH_2PO_4 undergoes a monoclinic-to-cubic phase transition at ~ 228 ºC at which the proton conductivity jumps by almost four orders of magnitude to $> 10^{-2}$ S cm^{-1} (Figure 1.5a). The monoclinic structure (Figure 1.5b) is comprised of phosphate groups linked in chains by double-minima hydrogen bonds, charge balanced by Cs cations. On heating, the structure transforms to a CsCl-type cubic structure with Cs at the corners and a phosphate group at the center. The phosphate group is often represented (as in Figure

1.5b) as equally occupying six symmetrically-equivalent crystallographic positions, and in essence, is rapidly rotating, enabling proton transfer between neighboring phosphate groups (Figure 1.6). Despite the disorder in structural oxygen, X-ray diffraction patterns of the superprotonic phase reveal sharp diffraction peaks due to the fixed positions of the cesium and phosphorus atoms in the lattice.

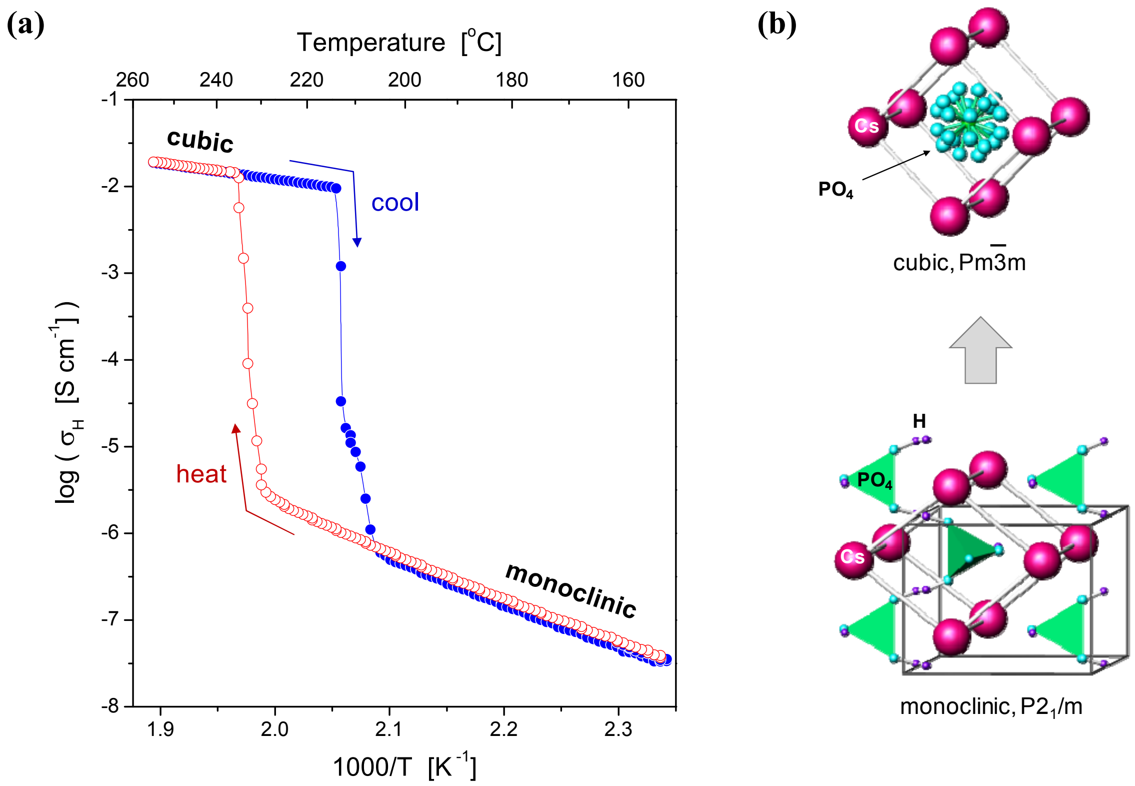

Figure 1.5 Superprotonic phase transition in CsH_2PO_4: (a) Plot of proton conductivity as a function of temperature, on heating and cooling, in flowing N_2 with ~ 0.4 atm H_2O, (b) Unit cells of monoclinic and cubic phases, the latter with high disorder in oxygen (PO_4) and hydrogen (not shown).

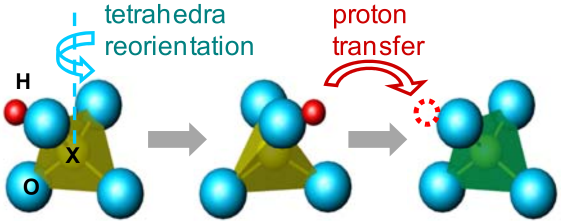

Figure 1.6 Schematic of the proton conduction mechanism in CsH_2PO_4.[13]

1.3.2 *CsH_2PO_4 as an Electrolyte: Benefits and Challenges*

Solid state electrolytes which facilitate anhydrous proton transport hold great promise for fuel cell applications. SAFCs operate at temperatures near 250 ºC using truly solid electrolytes that exhibit remarkably high, liquid-like proton conductivities. They retain the benefits of the "warm" operating temperatures while avoiding challenges associated with corrosive liquid electrolytes. The absence of corrosive liquids and the lower operating temperatures, compared to SOFCs, means that auxiliary components can be fabricated from relatively inexpensive stainless steel. The higher operating temperature of SAFCs, compared to PEMFCs, suggests higher fuel flexibility and the potential to eliminate costly precious metal catalysts in the electrodes. Equally important, solid acid electrolytes are true proton conductors and do not rely on a water molecules as carriers to transport protons, as is the case with polymer membranes. Because polymer membranes must remain sufficiently hydrated to maintain adequate proton conductivities, they require operation below 100 ºC and the use of complex water management systems to maintain sufficient hydration near the anode while minimizing flooding at the cathode.[4] SAFCs do not require such water management systems and can operate well beyond 100 ºC. The absence of water in the membrane also means that SAFCs can operate with methanol as a fuel with virtually none of the cross-over observed with polymer membranes.[3, 4, 14]

Although CsH_2PO_4 provides many advantages as an intermediate fuel cell electrolyte, it has some challenges of its own. CsH_2PO_4 reaches its superprotonic phase at relatively high temperatures, compared to other solid acid compounds, most of which transform at temperatures below 150 ºC (Figure 1.4); at the higher operating temperatures for CsH_2PO_4, dehydration has a greater tendency to occur via the reaction

$$CsH_2PO_{4(s)} \rightarrow CsPO_{3(s)} + H_2O_{(g)} \tag{1.9}$$

Therefore, a sufficient water vapor pressure must be supplied in the fuel and oxidant streams to suppress the dehydration process. A thorough study of the phase stability for CsH_2PO_4 has been carried out[15, 16] and serves as a guide for stable operating conditions. For example, a minimum water partial pressure of ~ 0.15 atm is required for reliable operation at 250 ºC. Under sufficient water partial pressures, one can observe the proton conductivity behavior (like that shown in Figure 1.5a) to be reproducible over many temperature cycles.

While solid acid compounds have tendency to dehydrate at elevated temperatures, they are readily soluble in liquid water. This is less of a concern during operation due to operating temperatures well above 100 ºC; however, during on-off cycling, humid reactant/product gases must be purged out of the system to avoid condensation.

A final challenge with solid acid compounds is related to their interesting mechanical properties. While solid acid compounds are relatively brittle in the low conductivity phase, they are highly plastic in the superprotonic phase, as has been reported specifically for $CsHSO_4$ and CsH_2PO_4.[3, 17–20] This has implications during fuel cell operation because sealing of the anode and cathode chambers are done so by the application of pressure which can cause irreversible deformation of the electrolyte over the course of operation. Avoiding this problem is not extremely difficult. It has been reported, in the case of CsH_2PO_4, that the strain rate can be reduced by a factor of five by adding ~ 10 wt% of 2 μm SiO_2 particles, with only a 20% drop in the proton conductivity at fuel cell operating temperatures.[3]

The challenges associated with CsH_2PO_4 as an electrolyte are not insurmountable by any means. CsH_2PO_4 remains, at present, the ideal electrolyte for SAFCs. Nevertheless, the search for additional application-relevant solid acid proton conductors is ongoing. Among the solid acid compounds known to undergo a superprotonic phase transition, almost all are based on sulfates and selenates which are unstable under the reducing conditions of the anode, reacting with H_2 to form H_2S or H_2Se.[21] Of the phosphate-based compounds possible, only that with Cs (the largest of the alkali metal cations) exhibits the superprotonic phase transition. A recently identified phosphite compound, $CsHPO_3H$,[11] which exhibits a relatively low phase transition temperature of ~ 140 ºC, has not been pursued extensively due to expectations that it would be unstable at oxidizing conditions, although related compounds show some promise as fuel cell electrolytes.[22, 23] Superprotonic solid acid compounds are a relatively unexplored class of materials with a rich chemistry that has not yet been fully exploited. As demonstrated in the recent report of a water-insoluble, superprotonic, barium-potassium compound[24], there is much room for the discovery and development of additional application-relevant proton conductors.

1.3.3 Solid Acid Fuel Cell Performance

Solid acid fuel cells based on CsH_2PO_4 as an electrolyte membrane, operating on humidified H_2 and O_2, have been demonstrated in literature to have peak power densities as high as 400 mW cm^{-2} at 248 ºC.[25] This demonstration was based on thin 25–36 µm CsH_2PO_4 membranes and composite electrodes comprised of a mixture of nanoparticulate Pt, carbon-supported Pt, and micron-scale CsH_2PO_4 particles. Despite the high Pt loadings used, ~ 8 mg cm^{-2} for each electrode, large activation overpotentials at the electrodes were found to limit the overall performance.[10]

Substantial progress has been made since the first demonstration of CsH_2PO_4-based SAFCs in 2004. SAFCs based on Pt-CsH_2PO_4 composite electrodes readily operate with 180 mW cm^{-2} peak power densities at ~ 250 ºC and degrade negligibly over several hundred hours of continuous operation.[3] Moreover, the power densities have been demonstrated to be scalable to 20-cell stacks, with each cell comprised of a 50 µm CsH_2PO_4 membrane and a total (anode + cathode) Pt loading of 4 mg cm^{-2}. SAFCs have also demonstrated resistance to poisoning by impurities in the fuel stream, thus improving fuel flexibility by lowering the cleanup requirements of reformed fuels. Specifically, a tolerance to H_2S, NH_3, CH_3OH, CH_4, C_3H_8 and CO at 100 ppm, 100 ppm, 5%, 5%, 3%, and 20%, respectively, have been reported.[3]

Although significant progress in SAFC development has been made, they are not yet competitive with those of conventional polymer and solid oxide fuel cells, primarily due to high activation overpotential losses at the electrodes. While it has been possible to fabricate thin electrolyte membranes to improve overall fuel cell performance, achieving electrodes with high activity or competitive platinum loadings remains a challenge. The current Pt loadings of 4 mg cm^{-2} is over an order of magnitude higher than loadings of ~ 0.1 mg cm^{-2} in PEMFC electrodes.[26] This is not necessarily surprising since the electrode requirements for SAFCs are in a class of their own, and the tools/processes required to optimize the electrode microstructure are still under development. Advancement of SAFCs requires the design of new electrode structures with improved performance and the development of new materials with high activity under SAFC operating conditions. Much of this work is presently under investigation, both by fabrication of high performing electrode structures[27, 28] and by fundamental mechanistic studies of electrocatalysis, discussed in this work.

1.4 Electrode Reactions in Solid Acid Fuel Cells

1.4.1 Hydrogen Electro-oxidation and Oxygen Electro-reduction

For a majority of fuel cells, the kinetics of oxygen electro-reduction is much slower than that of hydrogen oxidation. In the case of PEMFCs, the exchange current density, j_0 in Equation (1.8), for hydrogen oxidation is typically five to six orders of magnitude greater than that for oxygen reduction.[26, 29] There is some consensus on the hydrogen oxidation mechanism on Pt; specifically, hydrogen dissociatively adsorbs onto Pt and the resulting hydrogen is oxidized to protons and electrons, with dissociative adsorption being rate limiting.[26] On the other hand, oxygen reduction is considerably more complex. The oxygen reduction reaction, being a four electron transfer reaction, has at least four intermediate transfer steps. The reduction mechanism requires the dissociation of a strong O-O double bond and is further complicated by the formation of stable adsorbed intermediates such as M-O and M-OH (where M = metal catalyst).[26] These are a few reasons why the mechanism of oxygen reduction has not yet been fully elucidated even though it has been studied in the fuel cell community for decades. It is unclear how much information from the PEMFC literature can be translated to SAFCs due to their different operating temperatures and environmental conditions (i.e., presence of liquid water).

In the case of SAFCs, it has been shown that the electrode resistance at the cathode is roughly two orders of magnitude larger than at the anode.[10] To a first approximation, this activity difference between the anode and cathode is less drastic that that observed in PEMFCs. Thus, while most of the focus in the PEMFC community has been to improve electrocatalysis at the cathode, SAFCs stand to gain from improving the performance (and lowering the cost) of both the anode and cathode.

1.4.2 Electrochemical Reaction Pathways

Elucidation of reaction kinetics at the electrodes can provide valuable information that can be used to rationally design electrode structures and/or screen for new catalysts. However, reaction pathways for virtually every type of fuel cell remain elusive. Like heterogeneous catalysis, electrochemical catalysis relies on the intimate contact of a solid phase (catalyst) with a liquid or gas medium. However, electrocatalysis is notably more complicated because carrying out reactions that involve gas phase species, electrons and ions requires the presence of materials that can transport each of these species. Figure 1.7 shows some possible mechanisms for hydrogen oxidation and oxygen reduction via the triple-phase boundary pathway. From Figure 1.7, the complexity of the oxygen reduction mechanism is apparent simply from entertaining the number of possible reaction steps that can occur compared to hydrogen oxidation. In the case of hydrogen oxidation, hydrogen gas can adsorb (or dissociatively adsorb) directly onto the triple-phase site and undergo charge transfer, or, it can adsorb on the catalyst at some distance away in which case the adsorbed hydrogen must diffuse across the metal surface to be oxidized into protons and electrons at the triple-phase boundary. In the case of oxygen reduction, direct adsorption of O_2 and desorption of H_2O (Figure 1.7b) is the simplest pathway possible, but many other pathways are possible. For example, oxygen can adsorb as neutral (or partially reduced) species onto the metal catalyst before diffusing to the TPB site to be (further) reduced by incoming electrons and protons (Figure 1.7c). In yet another scenario, protons can be reduced to neutral hydrogen which then diffuses to the adsorbed oxygen species (Figure 1.7d). The rate at which each of these possible reaction steps can occur (if at all) depends on material properties (catalyst activity, ionic or electrical conductivity, solid or liquid), characteristics of the species (surface diffusion coefficients, bond strengths), electrode structure (number and identity of active sites) and also environmental conditions (temperature, gas environment, and partial pressure).

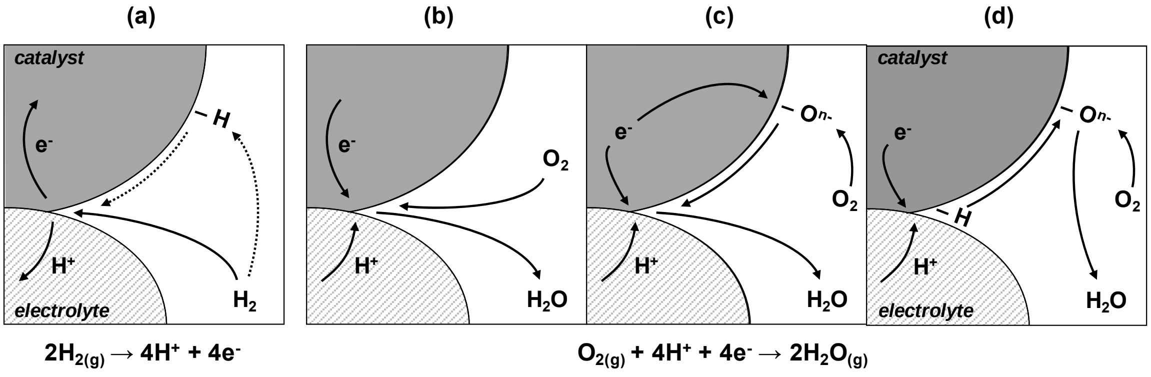

Figure 1.7 Simplified cartoon of some possible triple-phase boundary pathways in (a) hydrogen electro-oxidation and (b–d) oxygen electro-reduction.

Depending on the characteristics of the materials, it is entirely possible that the triple-phase boundary pathway is not relevant at all. While there are many systems in which the triple-phase boundary pathway is preferred, there are also a number of electrode systems which catalyze electrochemical reactions via a two-phase boundary pathway. This case can occur for electrodes which have both ionic and electronic conductivity, for example, cerium oxide and some perovskite oxides,[30] both of which are materials of interest for SOFCs. Many BCC and FCC metals, particularly palladium, are known to have a finite solubility of atomic hydrogen and therefore can transport both electrons and neutral species.[31] We present a (simple) schematic (Figure 1.8) for the latter case, comparing the triple-phase and two-phase boundary pathways for a metal catalyst in contact with a proton conductor. One can immediately see that, if the hydrogen can be transported through the metal, the active area is increased significantly, from a region confined near the TPB (Figure 1.8a) to the entire metal | electrolyte interfacial area. Whether a given electrode | electrolyte system catalyzes an electrochemical reaction via the triple-phase or two-phase pathway can have significant consequences in electrode design. In the case of an electrochemical reaction confined to TPB sites, a logical route would be to use catalyst nanoparticles to maximize the number of such sites (Figure 1.3), whereas a reaction occurring via the two-phase boundary pathway calls for maximizing the electrode | electrolyte interface.

It is clear that identification of the rate-limiting steps in electrochemical reactions is crucial to the advancement of SAFCs. Because the SAFC is the solid state system to operate at low-to-intermediate temperatures, there is a scarcity of electrochemical information the catalyst-solid acid system. In this work, we present our efforts to develop and employ novel tools to elucidate the reaction pathways in solid acid fuel cell systems.

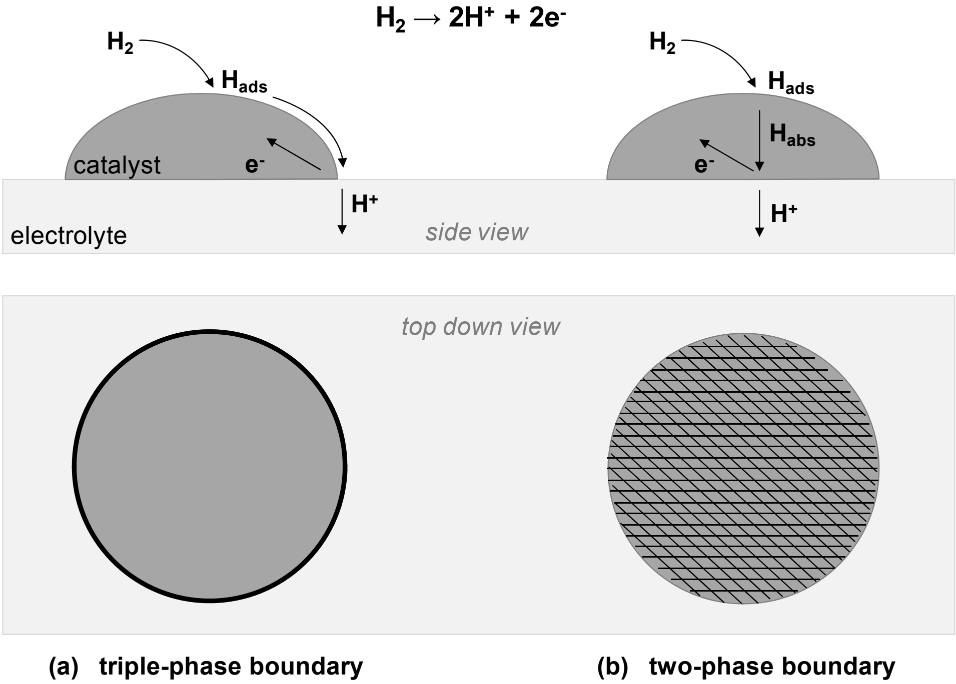

Figure 1.8 Comparison of triple-phase and two-phase boundary pathways for a metal catalyst in contact with a proton-conducting electrolyte.

Chapter 2 Experimental Methods

2.1 AC Impedance Spectroscopy

2.1.1 Basic Principles

Alternating current impedance spectroscopy (ACIS) is a powerful technique for characterizing a wide variety of electrochemical systems which undergo a great number of microscopic processes when stimulated with an electric field. The net current flowing through the system depends on the properties of the materials under investigation as well as the interfaces present. Processes occurring within the electrolyte, e.g., in the crystal lattice or across grain boundaries, as well as at electrode | electrolyte interfaces often occur with different characteristic timescales. ACIS holds the potential to distinguish between such electrochemical processes and determine the contribution of individual electrode or electrolyte processes which often elude DC techniques.[32–34]

In a typical AC impedance measurement, a low amplitude sinusoidal voltage perturbation is applied to the system of interest and the resulting current measured, or vice versa (Figure 2.1a). The effectiveness of ACIS lies in the application of a small signal perturbation of various frequencies. Each frequency stimulates a specific electrochemical response that depends on the behavior of charged species undergoing various processes, each with its own characteristic timescale. The input signal, $V(t)$, is described by the complex time-dependent wave function

$$V(t) = V_0 e^{j\omega t} \tag{2.1}$$

where V_0 is the amplitude, ω is the angular frequency ($2\pi f$), and $j = \sqrt{-1}$. For a signal small enough to probe a linear regime of the current-voltage characteristics of the system, the current response generated by this potential stimulus is sinusoidal with the same angular frequency and shifted by the phase angle, θ (Figure 2.1b). The current output, $I(t)$, can be expressed as

$$I(t) = I_0 e^{j(\omega t+\theta)} \tag{2.2}$$

where I_0 is the amplitude of the output current signal. The impedance can be written as

$$Z(\omega) = \frac{V(t)}{I(t)} = |Z| e^{-j\theta} \tag{2.3}$$

or

$$Z(\omega) = |Z|\cos\theta - j|Z|\sin\theta = Z_R - jZ_I \tag{2.4}$$

where $Z_R = |Z|\cos\theta$ and $Z_I = |Z|\sin\theta$ are the real and imaginary parts of the impedance, respectively, and $|Z|$ is the impedance modulus. A particularly useful representation of impedance spectra is the Nyquist plot, which is a plot of the impedance in the complex plane, $-Z_I$ against Z_R, both of which are parametric functions of frequency (Figure 2.2). In the Nyquist representation, electrochemical processes occurring with sufficiently different characteristic timescales (typically at least two orders of magnitude apart) are represented by separate arcs along the real axis, and the resistance associated with each arc is represented by the width of the arc on the real axis. Other common representations of impedance data are Bode-Bode plots, Figure 2.3(b–c), which are plots of $|Z|$ and θ as functions of frequency, computed using the relations

$$|Z(\omega)| = \sqrt{Z_R^{\,2} + Z_I^{\,2}} \tag{2.5}$$

$$\theta = \tan^{-1}\left(\frac{Z_I}{Z_R}\right) \tag{2.6}$$

Bode-Bode plots, although less commonly used for data presentation than Nyquist plots, are all the same employed for analysis of data. The existence of a phase shift between input voltage and output current, Figure 2.1b, (or in other words, an imaginary component in the impedance response) is a consequence of time-dependent nature of capacitive processes occurring in the system, for example, the dielectric properties of the bulk electrolyte, or the charging of interfaces. Figure 2.3 is a simple schematic illustrating how an alternating potential affects the movement of a charge species at different perturbation frequencies and the spectral features generated as a consequence of interactions between the charged species and its environment. At infinitely high frequencies, the charged species in the system samples an infinitely small distance in the bulk of the electrolyte; as such, the resistance is zero. At finite but high frequencies, the species can traverse further and interact with the bulk lattice, yielding a finite impedance. As the frequency is further lowered, interaction with grain boundaries, followed by electrode | electrolyte interfaces, occurs. For each of these processes, the corresponding arc in the spectrum describes resistive and capacitive behavior of that process. At infinitely low frequencies, all transient processes have reached steady state; the impedance of the system corresponds to the resistance of all the processes in the system, equivalent to that measured under DC conditions. Grain bulk and grain interior processes typically have characteristic frequencies that are relatively high and therefore yield arcs that are well-separated from electrode arcs. It should be noted that while only one electrode arc is shown in Figure 2.2, it is possible and even common to observe multiple electrode arcs.

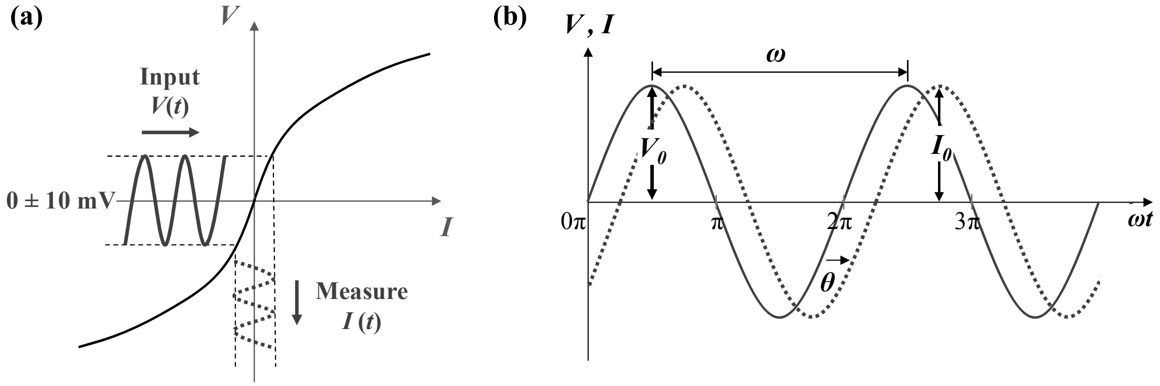

Figure 2.1 Basics of ACIS: (a) Depiction of an alternating voltage source and current response in relation to a generic polarization curve and (b) the relationship between input voltage and output current.

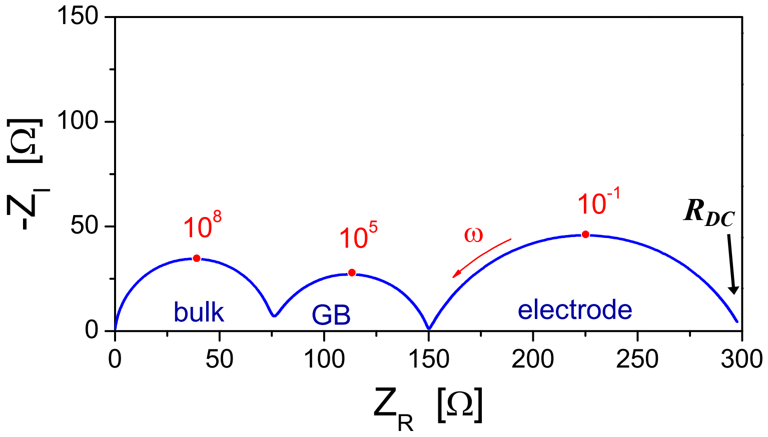

Figure 2.2 Simulated impedance spectrum, in a Nyquist representation, for a generic electrochemical system showing arcs for electrolyte processes (bulk and grain boundary, GB) and electrode processes. At low frequencies, the impedance approaches the DC limit (R_{DC}), that is, the slope of the polarization curve, Figure 2.1a.

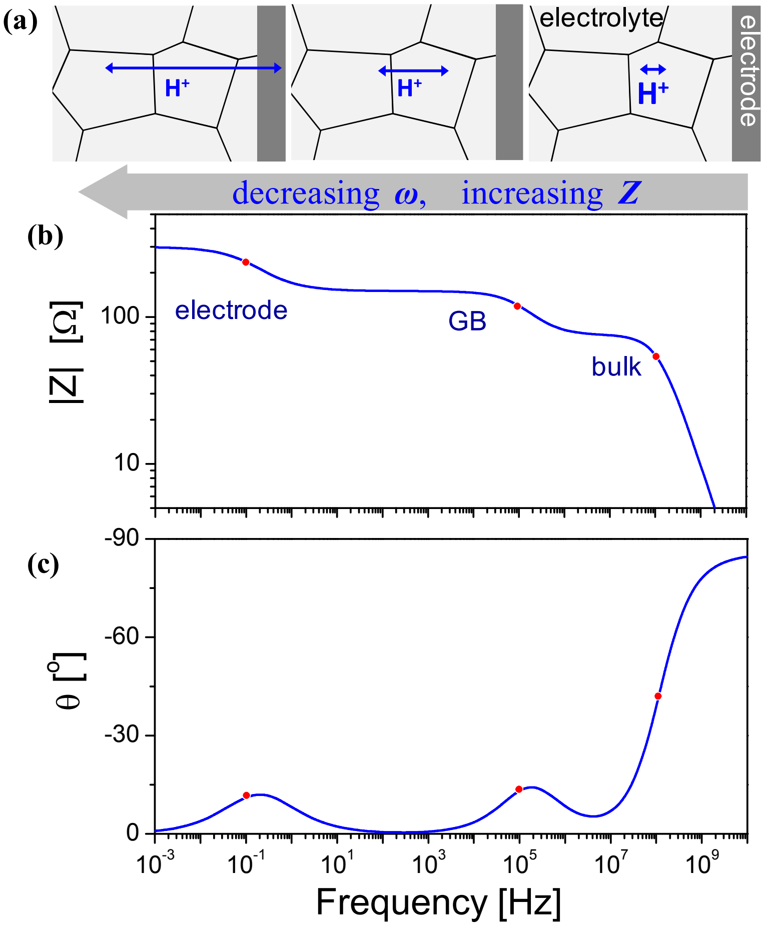

Figure 2.3 A simple cartoon depicting the movement of a proton under a perturbed electric field at various frequencies and how it gives rise to the shape of $|Z|$ and θ in the Bode-Bode plots. By convention, data are plotted as a function of f rather than ω.

2.1.2 Data Analysis: Equivalent Circuit Models

Because the fundamental principles that govern charge are similar between electrons and ions, it is possible to use electrical circuits to represent processes occurring in electrochemical systems. Table 2.1 shows some common circuit elements and their impedance responses. To analyze electrochemical data, one can build a circuit models comprised of a combination of discrete circuit elements.

Table 2.1 Impedance response of frequently encountered circuit elements.

	(a)	**(b)**	**(c)**	**(d)**
Circuit		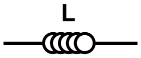	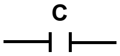	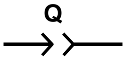
Impedance $Z(\omega)$	R	$j\omega L$	$\frac{1}{j\omega C}$	$\frac{1}{C_Q\left(j\omega\right)^n}$
Nyquist plot ($-Z_I$ vs. Z_R)	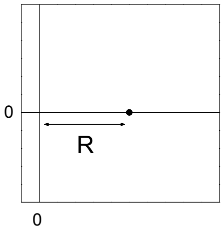	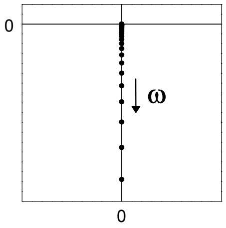	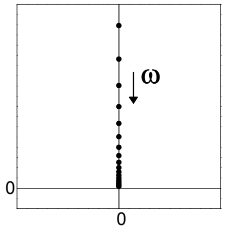	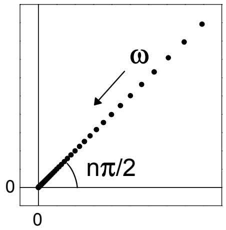

Table 2.2 shows the impedance response for several commonly used electrical sub-circuits. One particular sub-circuit frequently employed for data analysis is comprised of a resistor and capacitor in parallel, denoted here as RC. The RC sub-circuit generates a perfect semi-circle on the Nyquist plot with the center of the semi-circle lying on the real axis (Table 2.2a). The impedance of the RC circuit can computed readily from their individual elements.

$$Z_{RC}\left(\omega\right)=\left(\frac{1}{R}+j\omega C\right)^{-1}=\frac{R}{1+\omega^2C^2R^2}-j\frac{\omega CR^2}{1+\omega^2C^2R^2} \tag{2.7}$$

The width of the arc corresponds to resistance, R, and the capacitance, C, can be determined using the relation

$$\omega_0=\frac{1}{\tau_0}=\frac{1}{RC} \tag{2.8}$$

where ω_0 is the characteristic frequency, located at the apex of the semi-circle (Table 2.2a), and τ_0 is the characteristic timescale. It can be shown that multiple such sub-circuits, constructed in series, will yield separate arcs in the spectrum, provided that the characteristic frequencies are sufficiently different from one another, as illustrated in Figure 2.4a for three parallel RC sub-circuits in series. The resistances and the characteristic frequencies of each process can be extracted directly from the plot, and the corresponding capacitances can be computed using Equation (2.8). Table 2.2 shows several additional useful sub-circuits, for example, the R-RC (resistor in series with RC), which results in an offset of the arc from the origin along the real axis (Table 2.2b).

Table 2.2 Impedance response of frequently encountered sub-circuits. The unfilled data marker in each plot corresponds to the characteristic frequency, ω_0.

	Circuit	**Impedance** $Z(\omega)$	**Nyquist plot** ($-Z_I$ vs. Z_R)
(a)	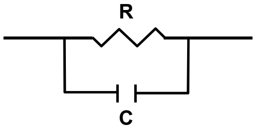	$\frac{R}{1+\omega^2C^2R^2} - j\frac{\omega C R^2}{1+\omega^2C^2R^2}$	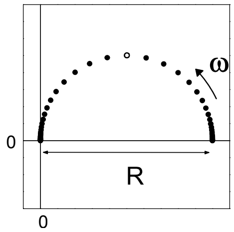
(b)	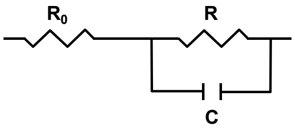	$R_0+\frac{R}{1+\omega^2C^2R^2} - j\frac{\omega C R^2}{1+\omega^2C^2R^2}$	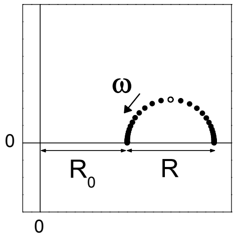
(c)	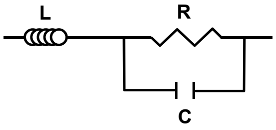	$\frac{R}{1+\omega^2C^2R^2} - j\omega\frac{R^2C-\omega^2C^2R^2L-L}{1+\omega^2C^2R^2}$	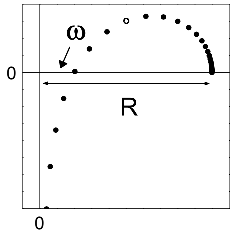
(d)	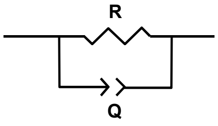	$\left(\frac{1}{R}+Y\left(j\omega\right)^n\right)^{-1}$	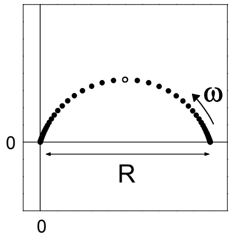

Of note is the L-RC circuit (inductor in series with RC) since this is commonly observed in experimental systems. In electrochemical measurements, electrical leads attached to (or in series with) the sample of interest can behavior like inductors. Because the impedance of an inductor increases with frequency ($Z_L = j\omega L$), the contribution of inductance is greater at higher frequencies at which the cell impedance (described by RC in this case) can often be "pulled" below the real axis (Table 2.2c). Such an effect may not only mask the true resistance (which is higher than the experimentally observed arc width) but also shift the characteristic frequency from the apparent apex of the arc.

In practice, impedance arcs are rarely perfect semi-circles but, rather, are slightly depressed. Graphically, this means that the arc can be visualized as a portion of a circle whose center lies below the real axis (Table 2.2d). This experimental observation has been treated by introducing an empirical circuit element, called the constant phase element, denoted as Q. The impedance response of the constant phase element is

$$Z_Q = \frac{1}{Y\left(j\omega\right)^n} \tag{2.9}$$

where Y is a constant and $0 \le n \le 1$. The constant phase element can be thought of as having resistive and capacitive character; Equation (2.9) corresponds to a capacitor with capacitance Y when $n = 1$, and a resistor with resistance Y^{-1} when $n = 0$. Like the RC circuit, the RQ circuit generates an arc in the Nyquist plot, but for $n < 1$, the arc appears depressed (Figure 2.4b). It can be shown that the characteristic frequency, ω_{Q0}, and equivalent capacitance, C_{equiv}, of the RQ sub-circuit are

$$\omega_{Q0} = \left(\frac{1}{RY} \right)^{1/n} \tag{2.10}$$

and

$$C_{equiv} = Y^{\frac{1}{n}} R^{\frac{1}{n}-1} \tag{2.11}$$

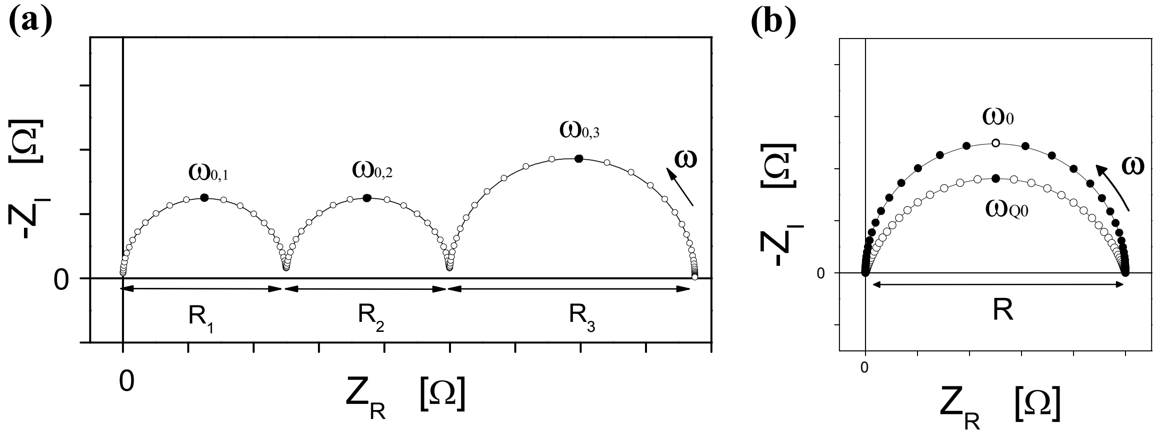

Figure 2.4 Impedance spectrum for (a) three serial RC sub-circuits with resistances and (b) a single RQ circuit plotted alongside a RC circuit.

Although the physical origin of a depressed arc in the impedance spectrum has not been fully established, there are some indications that surface roughness or spatial heterogeneities at interfaces are key factors.[34, 35] That is, heterogeneities at an interface results in a dispersion of characteristic frequencies of a process and the spreading, or depression, of the resulting arc. This explanation is consistent with typical n values of 0.95 and 0.75–0.85 for bulk and grain boundary processes, respectively; such values for n reflect the structural variety of grain boundary types as well as the expectation that ion transport across grain boundaries is more readily affected by impurities than bulk transport. The behavior of the electrode response varies widely and depends heavily on the electrode structure and the nature of the processes probed, however, n values as low as 0.6 are not uncommon.[36–40] Thus the Nyquist plot shown in Figure 2.2 can be represented by an equivalent circuit comprised of three RQ sub-circuits (Figure 2.5), with n values below 1.

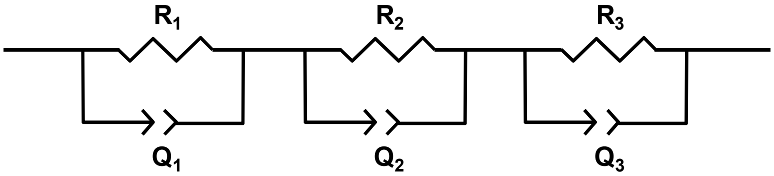

Figure 2.5 Equivalent circuit for describing three electrochemical processes occurring in series, such as those for grain interior, grain boundary, and electrode, shown in Figure 2.2.

While ion transport through the bulk of an electrolyte material, i.e., though grain interior and grain boundaries, is relatively straightforward to analyze, electrode processes are much more complicated because multiple parallel and serial pathways can be operative (Figure 1.7) and generate an ambiguous impedance response comprised of multiple arcs in the Nyquist plot (unlike the simplified single-arc electrode response shown Figure 2.2). In the absence of a physical model derived from appropriate transport equations and/or kinetic expressions, equivalent circuits are tremendously useful for analyzing impedance spectra and extracting parameters of interest. However, a given electrode response can be described by multiple equivalent circuits, each comprised of a discrete set of circuit elements in a specific configuration, and thus the choice of an equivalent circuit for analyzing data is not unique. Consequently, while equivalent circuits are extremely useful for preliminary analysis and the extraction of relevant kinetic parameters, it is not possible, without additional information about the system, to determine how these parameters relate to the physical processes of interest.

2.1.3 Data Analysis: Physical Models

There are several frequently used circuit elements which are based on physical processes. We present here the elements based on the Warburg impedance which describes an electrode process that is rate-limited by the diffusion of a reactant species to (or a product species from) the site at which an electrochemical step occurs. Consider the process shown in Figure 2.6, in which an uncharged species, R, diffuses from an interface at $x = L$ through some medium to an interface at $x = 0$ at which it undergoes a charge transfer reaction. (The medium in which R diffuses is one that is not affected by an electric field.) The Warburg impedances (Table 2.3) can be derived from Fick's second law,

$$\frac{\partial c_R}{\partial t} = D\frac{\partial^2 c_R}{\partial x^2} \tag{2.12}$$

where c_R is the concentration of species R, and D is the diffusion coefficient of R in the medium/electrolyte. In the simplest cases (as are presented here), it is assumed that charge transfer at $x = 0$ is infinitely fast such that the impedance response for the electrochemical step occurring at $x = 0$ is governed by the diffusion of R and the interfacial processes at $x = L$ at which R is supplied. Each spectrum shown in Table 2.3 is obtained by solving Equation (2.12), under a small perturbation about the equilibrium concentration, for different boundary conditions (also indicated in the table). Derivation of the Warburg impedance expressions in Table 2.3 can be found in the textbook by Orazem and Tribollet.[33] Note that the solutions to Equation (2.12) yield $n = 0.5$, but in practice, n is often allowed to vary freely during fitting of impedance data to provide an indication of non-idealities in the system.

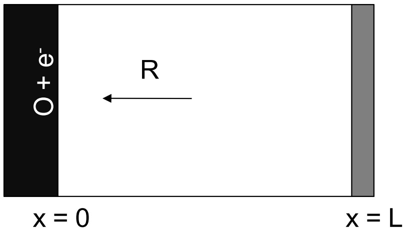

Figure 2.6 Schematic for the diffusion of R from an interface at $x = L$ to undergo charge transfer, $R \rightleftharpoons O + e^-$, at $x = 0$.

Table 2.3 Warburg impedance: solutions to Fick's second law for diffusion of an uncharged species, R. $\tau = L^2/D$ is the characteristic timescale of the diffusion process.

	(a) **Infinite-length Warburg**	**(b)** **Finite-length Warburg**	**(c)** **Blocked Warburg**
Circuit	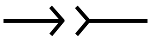		
Impedance $Z(\omega)$ (where $\tau = L^2/D$)	$\frac{R_0}{(j\omega\tau)^n}$	$R_0\frac{\tanh\left[(j\omega\tau)^n\right]}{(j\omega\tau)^n}$	$R_0\frac{\coth\left[(j\omega\tau)^n\right]}{(j\omega\tau)^n}$
Nyquist plot ($-Z_I$ vs. Z_R)	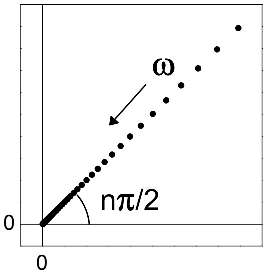	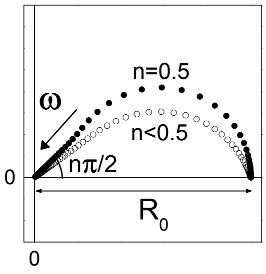	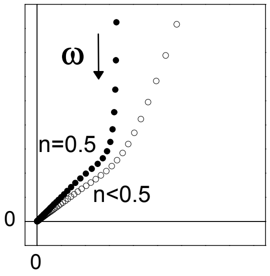
boundary conditions			
at $x = 0$	reversible/ fast charge transfer	reversible/ fast charge transfer	reversible/ fast charge transfer
at $x = L$	$L = \infty$, unbounded	reversible/ fast supply of R	irreversible/ slow supply of R

A characteristic feature of Warburg diffusion is a straight line, with a phase angle close to 45°, in the Nyquist plot at high frequencies. In the case of unbounded diffusion for which the boundary at $x = L$ is infinitely far away (Table 2.3a), the solution to

Equation (2.12) has the same form as the constant phase element, Equation (2.9) for $n \approx 0.5$, that is, the response approaches zero impedance at high frequencies and an infinitely large impedance at low frequencies. This is consistent with unbounded diffusion, since at zero frequency, the diffusion length (and therefore, the effective resistance) is infinitely large. In the case of bounded diffusion, i.e., $L \neq \infty$, and reversible boundary conditions, the impedance reaches a finite impedance at zero frequency (Table 2.3b) while retaining a similar linear response at high frequencies, giving it the characteristic half-teardrop shape (derivation shown in Appendix A.2). On the other hand, when diffusion is irreversibly bounded at $x = L$ (Table 2.3c), a linear regime is still evident at high frequencies, but the impedance increases suddenly at lower frequencies because the supply of the diffusing species is blocked at $x = L$.

It must be noted, again, that the use of any circuit is not unique and additional supporting evidence is required before employing any particular circuit element. In this particular case, the observation of a half-teardrop shape alone is not sufficient evidence of a process rate-limited by diffusion. For example, two (or more) electrode processes which have similar characteristic frequencies can manifest themselves as a single arc with a half-teardrop shape.

2.1.4 Experimental Corrections

Depending on the specific measurement of interest, it may be necessary to perform corrections to experimental data. If a high-frequency process is of interest, it is common to account for the inevitable inductance of the instrumentation by adding an inductor in series to the total circuit (assuming that inductance has been confirmed to be the culprit), as in Table 2.2c, or by applying a short-circuit correction. In the latter case, the electrical leads are connected together, or shorted, the impedance response measured at the same frequency points as used in the experiment, and the experimental data adjusted by subtracting the short correction measurement which is typically comprised of the resistance of the electrical leads and inductance of the system (wires and instrument). This option is available in some instruments for convenience, although a user-applied correction is relatively straightforward. Similarly, "open" corrections are also available; in this case, the sample is removed and the impedance response measured. Such a correction is particularly useful for samples which have small capacitances (as is the case for electrochemical AFM measurements, Chapter 4).

2.2 Potential Sweep (DC) Methods

Potential sweep voltammetry is a versatile technique for probing both transient and steady-state processes in electrochemical systems and is commonly used to examine processes such as adsorption/desorption or charging/discharging. In linear sweep voltammetry, the voltage is varied linearly with time at a defined rate from an initial voltage, V_1, to some final voltage, V_2, and the current response is measured. Data are typically presented as plots of the measured current as a function of the applied voltage. The simplest response one can obtain is at infinitely slow scan rates; in this case, the current measured contains no transient information. At non-zero scan rates, transient processes surface as peaks, that is, currents in excess of the steady-state (Faradaic) current. The position, size, and shape of the peak can provide a great deal of information about the process, such as the amount of charge passed or the kinetics of the process.[41] Using linear sweep voltammetry, one can capture the behavior of the system over a voltage range of interest and vary the scan rate to gauge the relative kinetics of transient processes.

One can also extend the process by reversing the voltage ramp after reaching a specified voltage (Figure 2.7). This method, called cyclic voltammetry, is commonly employed, particularly in aqueous electrochemistry, and gives additional information about the reversibility of the processes in the system. The shape of the voltammogram generated depends on the processes that are occurring in the system (Faradaic and/or non-Faradaic), the degree of reversibility, the kinetics and the chosen sweep rate. Figure 2.8 shows cyclic voltammograms for some common electrical circuit elements and circuits although real electrochemical systems often generate much more complicated responses because the resistance and capacitance of the process (R and C in the circuits of Figure 2.8) can vary with voltage.

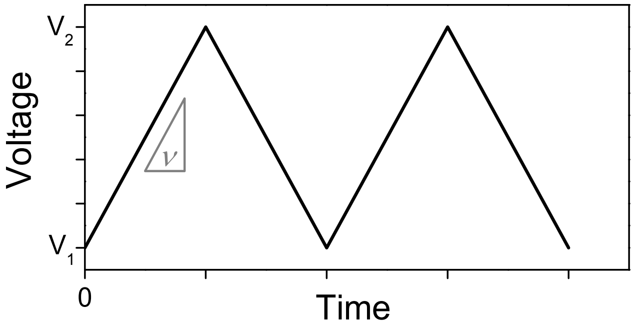

Figure 2.7 Example of a potential profile used in cyclic voltammetry for probing electrochemical processes occurring between V_1 and V_2. Here, two cycles are shown. The scan rate, ν, is the absolute value of the ramp rates.

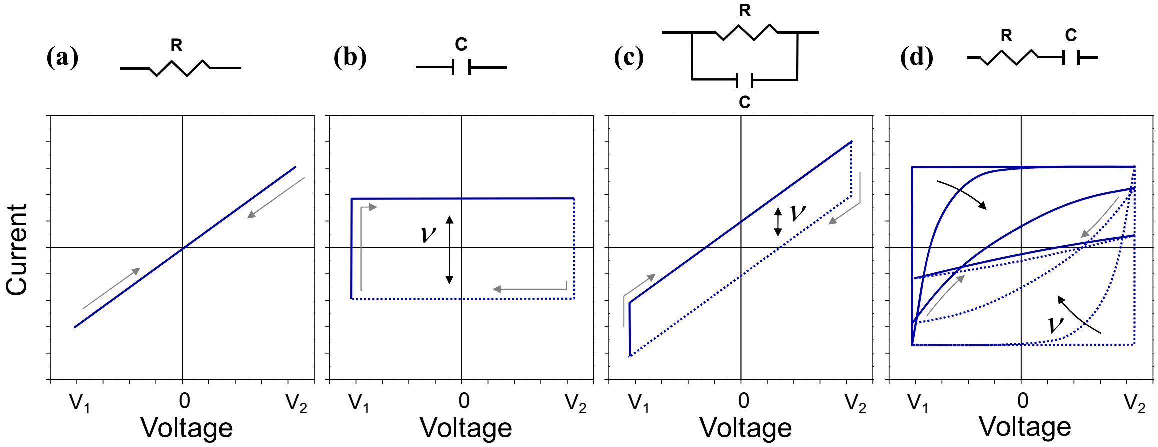

Figure 2.8 Schematic of cyclic voltammograms (one cycle) for a (a) resistor, (b) capacitor, (c) resistor in parallel with a capacitor, and (d) resistor in series with a capacitor. The scan rate is denote by ν.

Note that ohmic contributions can greatly affect the data quality, more so in sweep voltammetry techniques than ACIS. If the resistance of the electrolyte is large and dominates the total resistance, it can mask the electrochemical response of interest. In aqueous systems, the ohmic contribution can be minimized due to flexibility in the placement of electrodes, but in solid state systems, a high ohmic contribution cannot be avoided due to geometry constraints. It is, in principle, possible to manually subtract the ohmic contributions since the electrolyte conductivity is usually known, but if the electrolyte resistance is much higher than the electrode resistances, the correction may result in large errors.

2.3 AC vs. DC Measurements

The total resistance of the processes as measured by ACIS (real impedance at zero frequency) corresponds to the slope of the DC polarization curve, i.e., a sweep voltammogram collected at zero scan rate (Figure 2.1a). Thus, one can extract the entire polarization curve by performing impedance measurements at a range of voltages. In such measurements, one obtains not only the slope of the polarization curve but also the electrochemical behavior of individual processes. Furthermore, given a particular electrode process, it is possible to relate key parameters obtained using AC and DC methods. The electrode impedance at zero bias can be related to the exchange current, i_0, in the Butler-Volmer expression (Appendix A.1), which can extracted from the polarization curve to describe the kinetics of the electrode process at equilibrium conditions,

$$R_0 = \frac{RT}{i_0 F} \tag{2.13}$$

where R_0 is the total electrode resistance and i_0 is the exchange current density.

2.4 Scanning Probe Microscopy for Electrochemistry

Scanning probe microscopy is a class of mapping techniques based on the interaction between a nanosized probe and a surface of interest. Among these are scanning tunneling microscopy and atomic force microscopy, the most well-known and among the first developed (in 1981 and 1986, respectively). As there are many extensive textbooks on scanning probe techniques, we will only briefly provide some background information on atomic force microscopy, used in this work, and its relevance in solid state electrochemical systems.

2.4.1 Atomic Force Microscopy

Atomic force microscopy (AFM) relies on the interaction force between a nanoscale probe and a surface. In the simplest terms, it operates by dragging a sharp tip across a surface while monitoring the tip's lateral and vertical position; if the size of the tip is smaller than the features on the surface, then one can obtain a well-resolved image of the topography of that surface. AFM tips today can be fabricated with radii below 5 nm, and one need not rely on mechanical contact between tip and sample in order to obtain an image. When a probe is brought close to the sample surface, the atoms on the very tip of the probe and atoms at the sample's surface exhibit various interaction forces depending on their separation distance (Figure 2.9a). These forces include but are not limited to van der Waals, capillary, electrostatic, and chemical forces and are frequently exploited for mapping surface properties.

AFM tips/probes are usually made from silicon or silicon nitride and vary in shape and size. A probe is usually comprised of a finely etched tip which extends from the apex of a pyramid/cone (Figure 2.9b); the latter, in turn is supported on a beam, commonly a rectangular or triangular cantilever which extends from a silicon chip (Figure 2.9c). The tip radius, cantilever dimensions, and material properties are all design parameters which dictate the imaging capabilities of the probe. Generally, the tip radius controls the image resolution, and the beam characteristics give the spring constant of the probe and therefore the range of forces that can be probed during measurement. The interaction force between the tip and sample, F, is related to the cantilever characteristics via the relation

$$F = k_{cantilever} \Delta x \tag{2.14}$$

where $k_{cantiliver}$ is the spring constant of the probe and Δx is the deflection of the cantilever. Probes with spring constants ranging from 0.01 to 40 N m^{-1} are available commercially; the choice of probe depends on the application and imaging mode of interest.

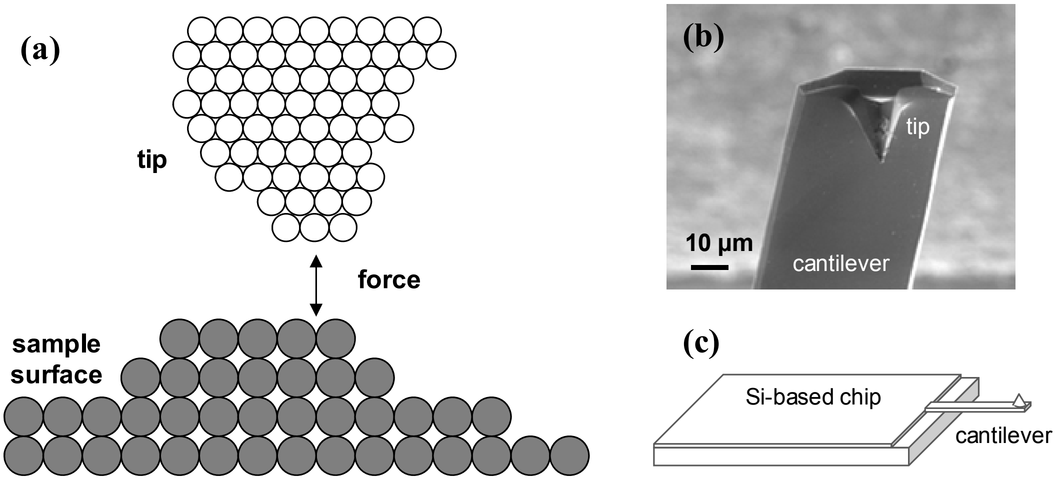

Figure 2.9 AFM probes: (a) interaction of tip and surface atoms, (b) SEM micrograph[42] of a cantilever and (c) a sketch of a probe.

Although there are several different operating modes in AFM, we discuss only contact mode operation which is used in this study. For a more extensive review, the reader is referred to the textbook by Bonnell.[43] Contact mode imaging is typically carried out by maintaining a constant force between the sample and probe by moving either the sample or probe to control the separation distance between the two. The instrumentation required for an atomic force microscope is relatively simple compared to other high resolution imaging techniques such as electron microscopy (Figure 2.10). As the probe is rastered across the sample surface via a piezoelectric scanner, the deflection of the cantilever is monitored by bouncing a laser signal off the top (reflective) surface of the cantilever. The reflected laser signal is measured by a four-quadrant photodiode detector, the signal from which is fed into the scanner to control the height of the sample to maintain a constant tip-sample separation/force. (Although the sample is being moved by the scanner in Figure 2.10, it is equally common to have the probe attached to the scanner and moved across an immobile sample.) The *x*-*y*-*z* movement of the piezoelectric is recorded to yield the final topography image. In order to perform a typical contact mode measurement, a desired force (or cantilever deflection) is specified by the user. Probes used for contact mode measurements are relatively compliant, with spring constants typically 0.1–1 N m^{-1} to minimize damage to the sample and tip.

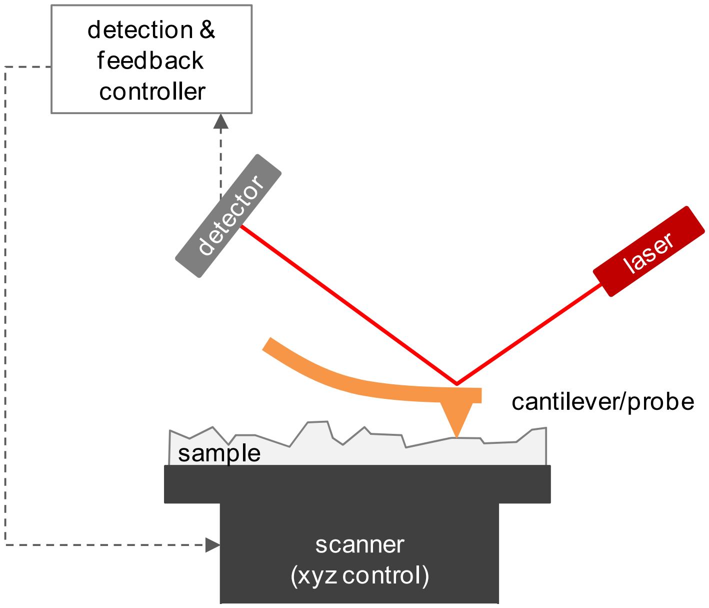

Figure 2.10 Operating principle of atomic force microscopy and basic components.

2.4.2 Electrical Atomic Force Microscopy

Electrical (or conducting) AFM is a technique in which a metal-coated AFM probe is used rather than an electrically insulated one. For electrical AFM, the system typically is operated in contact mode so that the probe is in physical contact with the sample surface. Given the proper instrumentation, the spatial variation of both topography and current can be recorded as the tip is rastered across a surface, and the local currents can be correlated to properties of the sample.

In this work, we extend such a technique to study materials which are ionic conductors. In this case, electrochemical reactions must occur at the probe | sample contact in order for current to pass. As such, the metal coating on the probe is one which is catalytically active, and the ionic conductor is fabricated with an active electrode at its underside to complete the circuit. Compared to conventional electrical AFM, measured currents can be significantly lower because the current is limited not only by the size of the probe but also the electrochemical activity of the probe | sample interface. Thus, a challenge of electrochemical AFM is its high system impedance, and thus great care must be taken to minimize spurious contributions to the electrochemical response. This includes reducing electrical and mechanical noise that causes fluctuations in the measured current and accounting for effects of stray capacitance.

Electrical AFM provides many advantages for exploring solid state electrochemical systems. The electrochemical activity of an ionic material at the nanoscale and its spatial heterogeneity can be readily explored. Not only this, AFM studies do not require vacuum, and, therefore, many materials can be examined under appropriate atmospheres and at elevated temperatures. Many metals/catalysts can be examined readily by simply changing the coating on the AFM probe, and current collection from the nanoscale probe, by design of the microscope, is automatic. Finally, as discussed in the Section 2.5.2 below, the small size of the probe enables electrochemical studies at the metal | solid electrolyte interface, under bias, without contributions from the second electrode (at the opposing side of the electrolyte).

2.5 Cell Geometries for Probing Solid State Electrochemistry

The impedance response of real systems often contains arcs that are not sufficiently well-separated in frequency. In such cases, analysis of data to identify the origin of the various electrode arcs can become difficult, and fitting with models can generate large errors and unreliable results. In this section, we discuss sample geometries and environmental conditions, relevant for solid state systems, which can alleviate some of the challenges associated with probing electrode reaction mechanisms. If chosen correctly, a specific cell configuration can greatly reduce the complexity of the impedance response, for example, by eliminating arcs or deconvoluting the impedance spectrum.

2.5.1 Symmetric vs. Asymmetric Gas Environments

Although fuel cell measurements are, by definition, operated in asymmetric gas environments, that is, with oxidizing conditions at the cathode and reducing conditions at the anode (Figure 2.11a), such a configuration is not commonly employed for electrochemical studies in the laboratory. One of the reasons for this is the experimental difficulty of sealing the two chambers to separate the two gases and holding a reproducible open-circuit voltage across the cell. Another reason is the possible ambiguity in identifying contributions from the anode and cathode which, in many cases, can be convoluted in the impedance response of the cell.

Symmetric cells are arguably the most widely used sample configuration for probing electrode properties of solid state fuel cell materials. In the symmetric cell configuration, identical electrodes are fabricated on both sides of the electrolyte membrane and placed in a uniform gas environment, either oxidizing or reducing, depending on the half-cell reaction of interest. In this configuration, unlike that for the fuel cell configuration, there exists no electrochemical potential gradient across the sample, so an electric field must be applied across the cell to induce an electrochemical response. Symmetric cell measurements are often studied near equilibrium conditions, that is, near the open-circuit voltage of zero, by using ACIS to apply a small perturbation about equilibrium. The resulting impedance response contains information about the resistance of the reaction of interest at equilibrium, that is, the slope of the polarization curve at 0 V. For example, for an electrode | electrolyte | electrode cell (with a proton-conducting electrolyte) in uniform hydrogen atmosphere, both the forward and reverse direction of $H_2 \rightleftharpoons 2H^+ + 2e^-$ at both electrodes are probed.

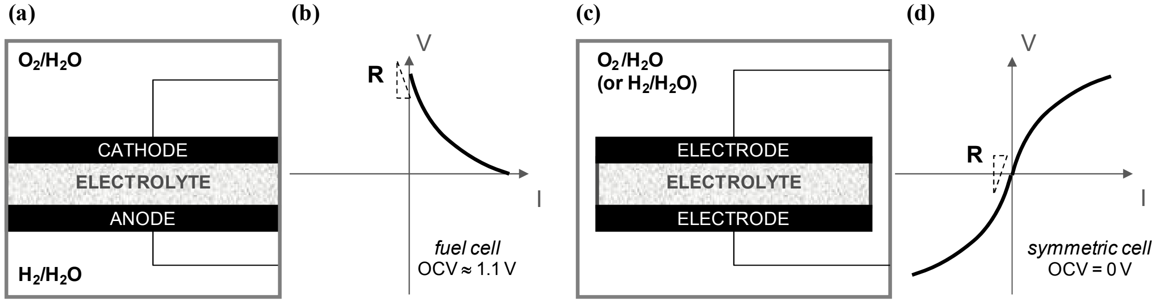

Figure 2.11 Schematics of and polarization curves for (a–b) fuel cell or asymmetric cell and (c–d) symmetric gas configuration. The total resistance measured at the open-circuit voltage corresponds to the slope of the polarization curve.

The relatively simple experimental setup required for symmetric cell studies makes it straightforward to gather a great deal of information about the electrode reactions. The main disadvantage of the symmetric cell configuration is the inability to probe a reaction under non-equilibrium conditions (i.e., away from the open-circuit voltage), which are considered more representative of the situation during fuel cell operation. Specifically, it is not useful to apply a non-zero net voltage across the cell; since the polarization curve for the symmetric cell is, itself, symmetric (Figure 2.11d), both hydrogen oxidation (occurring at one electrode) and proton reduction (occurring at the second electrode) will be occurring simultaneously. These two processes are rarely separable in the impedance spectrum, and, therefore, it is not easy to isolate the electrochemical response for the direction of interest, that is, hydrogen oxidation.

It should be noted there are no concerns with using symmetric cells for measuring the bulk properties (e.g., ionic conductivity) of the electrolyte; the electrolyte arc is usually well-separated from the electrode arc(s) and therefore can be identified easily. By the same argument, the choice of electrodes is not critical for bulk conductivity measurements since it does not impact ion conduction in the electrolyte.

2.5.2 Electrode Symmetry and Geometry

As mentioned in the previous section, it is not possible, with symmetric cell measurements, to extract the electrochemical response of a single electrode under a non-zero voltage. One might immediately suggest that the solution to this to use a three-electrode configuration (Figure 2.12a), in which the current is passed between the working electrode and counter electrode, but the voltage is measured against a reference electrode. Such a configuration commonly used in aqueous electrochemical systems. However, it has been shown that, in systems based on solid electrolytes, the placement of the electrodes can greatly affect the results and thus a small misalignment can influence the measured electrochemical response.[44, 45]

Another way to extract the response of a single electrode, while still retaining the experimental convenience of the symmetric gas environments, is to change the characteristics of the two electrodes. During measurement, the voltage applied across a cell comprised of an electrolyte sandwiched between two electrodes (denoted by subscripts 1 and 2) is given by the expression

$$V_{tot} = IR_{tot} = V_{el} + I\left(\frac{\tilde{R}_1}{A_1} + \frac{\tilde{R}_2}{A_2}\right) \tag{2.15}$$

where V_{tot} is the total voltage drop across the cell, V_{el} is the voltage drop across the electrolyte, I is the current that passes through the cell and R_{tot} is the total resistance of the system, a portion of which comes from the electrode resistances, $\tilde{R}_1 / A_1$ and $\tilde{R}_2 / A_2$. $\tilde{R}$ denotes the area-normalized resistance in units of Ω cm^2 (i.e., inverse activity of the electrode), and A denotes the electrode area. Equation (2.15) can be rearranged to obtain

$$V_{tot} = V_{el} + V_1\left[1 + \frac{\tilde{R}_2}{\tilde{R}_1}\left(\frac{A_1}{A_2}\right)\right] \tag{2.16}$$

For the symmetric cell case (Figure 2.11c), $A_1 = A_2$ and $\tilde{R}_1 = \tilde{R}_2$. Therefore,

$$V_{tot} = V_{el} + 2V_1 \tag{2.17}$$

showing that the voltage loss due to the electrodes are equally distributed between the two identical electrodes (i.e., $V_1 = V_2$).

From Equation (2.16), one can immediately see that the relative contributions of the two electrodes to the total voltage loss (overpotential) depends on their relative activities and areas. If $A_1 = A_2$ but $\tilde{R}_1 \gg \tilde{R}_2$ (Figure 2.12b), then

$$V_{tot} = V_{el} + V_1\left[1 + \frac{\tilde{R}_2}{\tilde{R}_1}\right] \approx V_{el} + V_1 \tag{2.18}$$

and the voltage drop across the entire cell is only comprised of that from the electrolyte and from Electrode 1. To achieve this in the laboratory, Electrode 2 would need to be fabricated with much higher performance than Electrode 1. This can be done by either increasing the active site density of Electrode 2 or increasing the inherent activity of the electrode/catalyst. Note that the two electrodes need not be comprised of the same material; for example, one can use, for Electrode 2, a catalyst with much higher inherent activity. In practice, such an approach is not particularly useful because it is limited to the study of low-activity electrode materials.

A more straightforward route is to keep the electrode activities exactly the same, $\tilde{R}_1 = \tilde{R}_2$, but change the relative areas of the electrodes, $A_2 << A_1$ (Figure 2.12c). Equation (2.16) then yields

$$V_{tot} = V_{el} + V_1 \left[1 + \frac{A_1}{A_2} \right] \approx V_{el} + V_1 \quad (2.19)$$

In both Equations (2.18) and (2.19), the overall voltage drop is dominated by that across the electrolyte membrane and only one of the electrodes. The electrode with the higher absolute resistance, $\tilde{R}_1 / A_1$ (Electrode 1, in this example), becomes the working electrode because it dominates the total electrode response of the cell. The electrode with the lowest absolute resistance, i.e, higher activity and/or larger area, contributes negligibly to the total cell resistance and essentially behaves as a reversible, reference electrode. Thus, one can apply a voltage with respect to this reference electrode and probe electrochemical reactions at the working electrode under fuel cell relevant potentials. The ohmic electrolyte contribution can be easily separated from the electrode contribution via impedance spectroscopy.

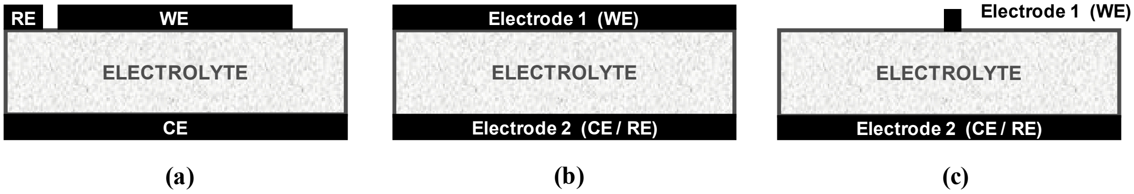

Figure 2.12 Possible electrode geometry configurations for solid state electrochemical measurements: (a) three-electrode configuration, (b) asymmetric activity electrodes, $\tilde{R}_1 \gg \tilde{R}_2$ and (c) asymmetric electrode geometry, $A_2 >> A_1$. WE = working electrode, CE = counter electrode and RE = reference electrode

In general, either of the geometries shown in Figure 2.12(b–c), or a combination of the two, can be used in symmetric gas conditions to isolate the electrochemical reactions occurring at a single electrode `under bias. The reference voltage corresponds to the electrochemical reaction which occurs in at the reference electrode, for example, $2H_{2(g)} \rightleftharpoons 4H^{+} + 4e^{-}$ if the measurement was performed under uniform H_2-H_2O atmospheres, or $O_{2(g)} + 4H^{+} + 4e^{-} \rightleftharpoons 2H_2O_{(g)}$ for uniform O_2-H_2O atmospheres. The choice of geometry for obtaining asymmetry depends on the situation, but as mentioned previously, fabrication of asymmetric electrode geometries is usually a more straightforward route. The main consideration, in this case, is to take into account the behavior of the equipotential lines which vary with the degree of asymmetry (Figure 2.13). For example, for a given electrode asymmetry, a thinner electrolyte membrane results in the utilization of a smaller portion of the counter/reference electrode (Figure 2.13a). While a thicker electrolyte membrane improves utilization of the counter electrode (Figure 2.13b), an increase in the ohmic losses can mask electrode response. A quantitative analysis of the geometric requirements can be found in work by Sasaki et al.[36]

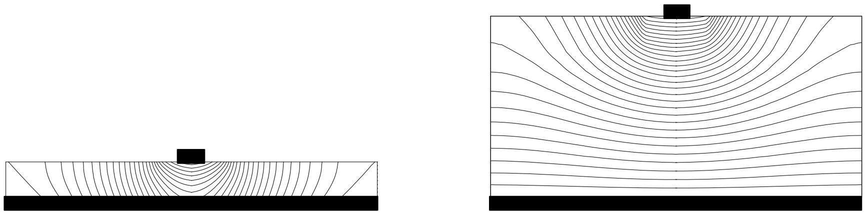

(a) **(b)**

Figure 2.13 Effect of electrolyte membrane thickness on equipotential lines in asymmetric geometry electrode configuration. In (a), a majority of the current is passing through a small region of the counter electrode whereas in (b), the current is more uniformly distributed throughout the entire counter electrode.

2.5.3 Electrode Microstructure

In the laboratory, there are several types of electrode structures which can be fabricated for use in fundamental electrochemical studies. The most obvious are composite electrodes which mimic those used in real fuel cells. However, while composite electrodes are application-relevant, they are often extremely complex, with random distributions of two-phase and three-phase boundaries (Figure 2.14a). Such a complicated microstructure prevents the correlation of the measured electrochemical response to the corresponding active sites which often are not known to begin with. Thus, there is an advantage to simplifying the microstructure to one in which the experimentalist has a specified level of control over the electrode microstructure and therefore the active sites. Figure 2.14(b–d) shows several examples of electrodes for which the microstructure can be controlled. Thin film techniques can be used to grow a film with a known microstructure, such as one with a porous columnar morphology (Figure 2.14b) for which the porosity and surface area can be controlled. In another case, photolithographic techniques can be employed to fabricate dense, patterned films[46–49] with defined edges and interfaces (Figure 2.14c). Given optimization of microfabrication conditions, patterned electrodes are extremely flexible because a wide range triple-phase and two-phase boundary sites can be fabricated. Also commonly employed are dense films for which the film thickness and/or perimeter can be controlled.[37, 50–55] These are the simplest of geometries and are relatively easy to fabricate in the laboratory.

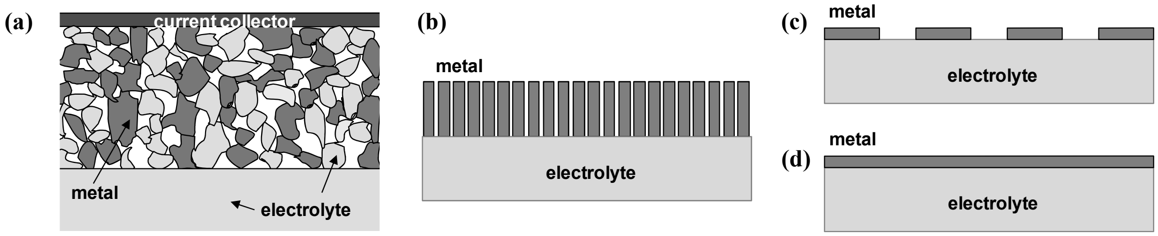

Figure 2.14 Various electrode microstructures in metal/catalyst-electrolyte system for electrochemical studies: (a) application-relevant composites, (b) electrode films with controlled microstructure, e.g., columnar, (c) patterned films and (d) dense films

2.6 Solid Acid Compounds for Electrode Studies: Challenges

2.6.1 Water Solubility

While patterned electrodes are ideal for fundamental electrode studies in the metal | solid acid system, the solubility of solid acid compounds in water precludes the use of photolithography which routinely involves the use acids and/or water-miscible solvents. In order to study electrocatalysis in systems based on water-soluble electrolytes, the most straightforward method is to fabricate thin dense metal films (Figure 2.14d) by shadow-masking. Although using shadow masks, particularly in conjunction with sputtering, results in metal edges which are not as well-defined as those made by photolithography, the technique provides good control of the film thickness and the fabrication procedure is straightforward. Thin film electrodes were fabricated using this technique for hydrogen electro-oxidation studies in Chapter 3.

There has been work to synthesize solid acid electrolytes which are not water-soluble and therefore amenable to further electrode fabrication techniques. For fundamental electrode studies, water-insoluble compounds provide an enormous advantage with respect to processing, for example, compatibility with wet polishing methods to generate smooth substrate surfaces and with photolithography processes to fabricate well-defined electrode | electrolyte boundaries. Some success was found for $Ba_{3-x}K_xH_x(PO_4)_2$ which crystallizes, with $x \approx 0.5–0.9$, in the trigonal phase, similar to known superprotonic compounds such as $Rb_3H(SeO_4)_2$.[24] However, its relatively poor proton conductivity, two to three orders lower than that those for typical superprotonic solid acids, may render it unsuitable as a representative electrolyte substrate for probing electrocatalysis in solid acid systems.

2.6.2 Mechanical Properties

Although the room temperature phases of solid acid compounds are brittle, superprotonic phases are plastic and susceptible to irreversible deformation under stress.[17–19, 56] This ductility has consequences in terms of application of pressure to electrochemical cells, sometimes done to make electrical contact to electrodes and avoid solvents in conductive paints (Appendix C.2.4). Over time, the cell may deform slightly, destroying carefully fabricated electrode structures.

2.6.3 Superprotonic Phase Transition

The superprotonic phase transition is a solid-to-solid phase transformation between two different crystal structures, and thus, incompatibilities between the two solid phases can cause cracks to form in the material. Cycling of the temperature through the phase transition (Figure 2.15) shows that the open-circuit voltage depends on whether the electrolyte is above or below the phase transition temperature; the open-circuit voltage corresponds closely to the theoretical (Nernst) voltage at superprotonic conditions but drops to voltages below 0.5 V at temperatures below the phase transition temperature.

The lower voltages suggest that fuel and oxidant may be meeting via microcracks formed in the relatively thin CsH_2PO_4 membrane, while high open-circuit voltages at high temperatures indicate that, should such microcracks form, they fortuitously heal under the plastic flow of the electrolyte. (An alternative explanation is that poor electrochemical kinetics below the phase transition temperature precludes accurate voltage measurements, resulting in an artificial drop in the measured voltage.)

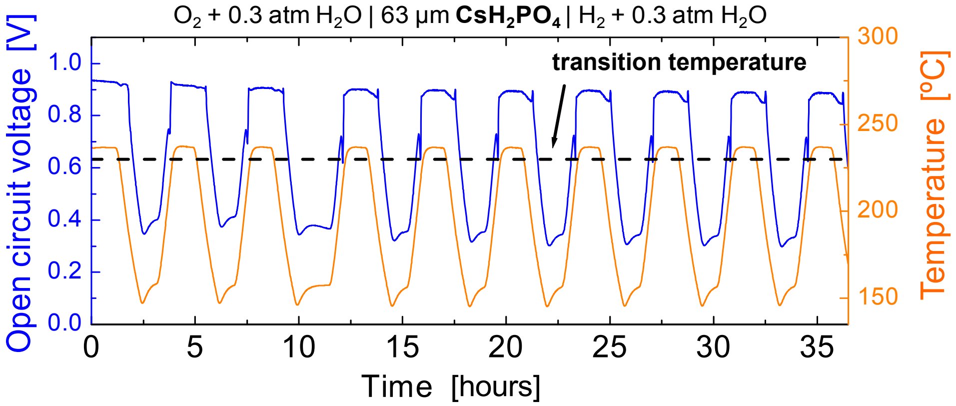

Figure 2.15 Fuel cell open-circuit voltage with temperature cycling.[57] The voltage drops on cooling across the phase transition and recovers on heating to the superprotonic phase.

Cracking also has implications in fundamental electrochemical studies. Cracks can be propagated to any conformal electrode structure that is fabricated on top of these solid acid electrolytes, lowering the efficacy of carefully-fabricated electrode structures. In Chapter 5, we examine the origin of the incompatibility between phases and explore ways to reduce incompatibility and cracking. The density of cracks varies between solid acid compounds, so it may be possible to use solid acid substrates which have little to no cracks. Solid acids which fall under this categories are $CsHSO_4$ and $Rb_3H(SeO_4)_2$.[19] $Ba_{3-x}K_xH_x(PO_4)_2$ compounds are also crack-free substrates because, by design, they do not undergo a superprotonic phase transition;[24] however, as mentioned previously, it is unclear whether the proton conductivity is high enough to be used for electrode studies.

2.6.4 Thermal and Chemical Stability

As the solid acid electrolyte of choice, CsH_2PO_4 is chemically stable in both oxidizing and reducing conditions. However, its tendency to dehydrate increases with temperature.[10, 15] As discussed in Chapter 1, such behavior is not problematic for fuel cell operation; however, it limits the temperature and water partial pressure range that can be used to probe activation energy and partial pressure dependences when performing fundamental electrode studies. Furthermore, the water partial pressure requirements preclude the use of CsH_2PO_4 in electrochemical AFM studies which cannot accommodate the water partial pressures required to suppress CsH_2PO_4 dehydration.

Several other systems can be used as representative substrates for studying electrocatalysis at electrode | solid acid interfaces, although they do not come without their own limitations. $CsHSO_4$ is very stable against dehydration and thus can be used in instrumentation that cannot accommodate high water vapor contents (e.g., electrochemical AFM, Chapter 4). However, studies cannot be performed in reducing conditions since sulfates (and selenates) can be reduced by hydrogen.[12] Low-temperature solid acids stable in reducing environments include $CsHPO_3H$ and related compounds,[11, 22, 23] although, in the case of $CsHPO_3H$, careful handling would be required because it is deliquescent at ambient conditions. Again, $Ba_{3-x}K_xH_x(PO_4)_2$ compounds for $x \approx 0.5–0.9$ has been found to be chemical and thermally stable up to ~ 300 ºC and remains an option for future studies, particularly for experiments via electrochemical AFM (as demonstrated in Appendix G).

Chapter 3 Hydrogen Electro-oxidation over Thin Film Pt Electrodes

Louie, M. W.; Haile, S. M. Platinum Thin Film Anodes for Solid Acid Fuel Cells. *submitted* **2011**

Abstract

Hydrogen electro-oxidation kinetics at the Pt | CsH_2PO_4 interface have been evaluated. Thin films of nanocrystalline platinum 7.5–375 nm thick and 1–19 mm in diameter were sputtered atop polycrystalline discs of the proton-conducting electrolyte, CsH_2PO_4, by shadow-masking. The resulting Pt | CsH_2PO_4 | Pt symmetric cells were studied under uniform H_2-H_2O-Ar atmospheres at temperatures of 225–250 ºC using AC impedance spectroscopy. For thick platinum films (> 50 nm), electro-oxidation of hydrogen was found to be limited by diffusion of hydrogen through the film, whereas for thinner films, diffusion limitations are relaxed and interfacial effects play an increasingly dominant role. Extrapolation to vanishing film thickness implies an ultimate interfacial resistance of 2.2 Ω cm^2, likely reflecting a process at the Pt | $H_{2(g)}$ interface. Films 7.5 nm in thickness displayed a total electro-oxidation resistance, $\tilde{R}$, of 3.1 Ω cm^2, approaching that of Pt-based composite anodes for solid acid fuel cells (1–2 Ω cm^2). In contrast, the Pt utilization ($\tilde{R}^{-1}$/Pt loading), 19 S mg^{-1}, significantly exceeds that of composite electrodes, indicating that the thin film approach is a promising route for achieving high performance in combination with low platinum loadings.

3.1 Introduction

Elucidation of electrochemical reaction pathways is essential for optimizing electrode microstructure as well as catalyst selection. However, as is the case for a majority of fuel cell systems, the mechanism for electrocatalysis in solid acid fuel cells is not known. Composite electrodes used in operating fuel cells are designed to maximize the number of active sites and improve electrode performance but are not suitable for mechanistic studies because the complex microstructure precludes an unambiguous analysis of the resulting electrochemical response. Accordingly, electrochemical cells for which the electrode | electrolyte boundaries are well-defined are ideal for studying fundamental electrochemistry in solid state systems. By varying the geometric parameters of the electrode, one can examine how the rate-limiting process varies with the number density of the active sites, e.g., triple-phase boundary (TPB) and two-phase boundary sites.

The thin film electrode | electrolyte interface has been used as a model system for examining reaction kinetics in solid state electrochemistry.[37, 38, 46, 47, 50, 53, 55, 58–62] At a minimum, such a configuration consists of a thin dense electrode film deposited on an electrolyte material,[37, 50, 53, 55, 58–60] either covering the entire surface or confined to a specific area, and provides control over the film thickness and/or area. In systems that require the examination of a larger range of geometric parameters, microfabrication techniques are employed to fabricate electrode films of various patterns,[38, 46, 47, 61, 62] enabling the manipulation of electrode dimensions such as the film thickness, perimeter (i.e., triple-phase boundary length) and the interfacial electrode | electrolyte area (i.e., two-phase boundary). While both uniform and patterned electrodes allow for precise control over electrode dimensions, patterned electrodes enable more flexible and independent control over the two-phase and three-phase boundary sites.

Although patterned electrodes are, in general, the preferred choice for kinetic studies, the water solubility and temperature sensitivity of CsH_2PO_4, that is, its tendency to dehydrate at elevated temperatures and low humidities,[15] precludes the use of most conventional microfabrication techniques for film deposition and pattern creation. In this work, we employed shadow masks, placing them over CsH_2PO_4 substrates to fabricate platinum film electrodes of various thicknesses and areas by sputter deposition. The resulting $Pt | CsH_2PO_4 | Pt$ symmetric cells were characterized by AC impedance spectroscopy and the rate-limiting step for hydrogen electro-oxidation probed as a function of the metal film dimension and environmental parameters, specifically, temperature and hydrogen partial pressure.

3.2 Experimental

3.2.1 Sample Preparation

Dense polycrystalline CsH_2PO_4 discs were fabricated by uni-axial compression of CsH_2PO_4 powders (synthesis detailed elsewhere[58]) at a pressure 138 MPa for 20 min. The discs were mechanically polished with silicon carbide sandpaper (grit sizes 600 followed by 800) and then sonicated in acetone, followed by isopropanol, before drying in air at ~ 100 ºC. The final discs were 19 mm in diameter and ~ 1 mm thick, with densities 95 ± 2% of theoretical.

Thin film Pt electrodes were deposited onto CsH_2PO_4 discs by DC magnetron sputtering at room temperature using a AJA International ATC Orion system (3 mTorr Ar, 150 W plasma power) or a Cressington 208HR system (~ 15 mTorr Ar, 80 mA plasma current). The CsH_2PO_4 substrates were shadow-masked to restrict the exposed area to that corresponding to 19, 15, 12.6, 10, 4.7, and 1.3 mm in diameter. The sputtering time was varied to obtain films with thicknesses ranging from 7.5 to 375 nm. The deposition of 10 nm Au films was carried out using the ATC Orion system, with sputtering conditions identical to those for Pt. All cells were fabricated with a symmetric geometry.

3.2.2 Characterization

The general crystallinity of the platinum films, adhered to the substrates, was evaluated using a Phillips X'Pert Pro powder X-ray diffractometer using Cu Kα radiation (45 kV, 40 mA) with a 2θ range of 15–90°. Additional analysis was performed using films that were isolated from the substrate. Double-sided tape was applied and the Pt film removed either mechanically or by dissolution of the substrate in water. Diffraction measurements were performed over the 2θ range of 38–42° to access the strongest, (111) peak of Pt, using a step size of 0.008° and various dwell times, depending on the film thickness, to collect sufficient signal intensity for analysis. The full-width half-max of the (111) peak was extracted from a Lorentzian fit and the grain size calculated using the Scherer equation,[63] $t \approx 0.9\lambda/B\cos\theta$, where t is the grain size, $\lambda = 0.1541$ nm, and B is the instrument-corrected full-width half-max at $2\theta \approx 40°$ at which instrument broadening was determined to be ~ 0.08°.

The morphology of the metal films both before and after electrochemical characterization was observed by scanning electron microscopy, SEM, (LEO 1550VP, Carl Ziess SMT) using a 3 kV accelerating voltage. Film thickness was measured by cross-sectional SEM imaging of fractured cells, and the deposition rate of Pt was determined to be 9.8 nm min^{-1}. Image analysis, specifically, evaluation of the number density of cracks in the films that formed due to thermal cycling, was performed using ImageJ software.[64] The film connectivity was assessed by measuring the sheet resistance of the films, using a hand-held multimeter, both before and after testing.

Impedance spectra were collected, in the majority of cases, using a Solartron Analytical 1260 frequency response analyzer with a 10 mV perturbation voltage about zero bias over frequencies of 10 MHz to 100 mHz configured with a four-probe measurement geometry. For experimental convenience, some spectra were collected using a Solartron 1250 analyzer equipped with a potentiostat (Princeton Applied Research, EG&G 273A). In this case, a three-probe configuration was used, and the high-frequency limit was 60 kHz. For the frequency range of interest, the two instruments yielded excellent agreement in the impedance response. Electrical connection to the cells was made using an in-house constructed sample holder in which the cells were sandwiched between two pieces of Toray carbon fiber paper (280 μm thick) placed between two stainless steel porous discs. Using the sample holder, adequate pressure was applied to the assembly to mechanically contact silver wire leads to the stainless steel discs. The use of carbon fiber paper, with estimated interfiber spacings of ~ 100 μm, ensured sufficient current collection for thin 7.5 nm Pt films. For a subset of the thicker films, electrical connection was made by the direct attachment of silver wires using colloidal silver paint (Ted Pella, #16032); such a method did not yield electrode responses different from that with Toray paper.

Electrochemical impedance measurements were collected under uniform H_2-H_2O-Ar atmospheres at temperatures between 225 and 250 ºC. The range of temperatures explored is limited, at one end, by the (reverse) phase transition temperature of ~ 221 ºC on cooling[65] and, at the other end, by the tendency for CsH_2PO_4 to dehydrate at elevated temperatures.[15, 66] Hydrogen partial pressures between 0.1 and 0.5 atm, for a fixed water partial pressure of 0.5 atm, were achieved by flowing inlet H_2-Ar mixtures through a heated water bubbler. The water partial pressure of the resulting gas stream was measured with a humidity sensor (HygroFlex 2 with IM 1 probe, Rotronic Instrument Corp). The total gas flow rate of ~ 160 mL min^{-1} was verified to be sufficiently high so as to eliminate possible mass transport effects, and the perturbation voltage of 10 mV was confirmed to yield a linear impedance response. Data presented in this work were acquired once the electrode resistance (arc width) exhibited a degradation rate below 2% h^{-1}.

Acquired impedance spectra were analyzed using the commercial software ZView (Version 2.9b, Scribner Associates, Inc.). In addition to fitting the electrode response, additional circuit elements were placed in series with the electrode circuit to account for contributions from wire resistance, system inductance and bulk transport properties of the CsH_2PO_4 substrate. The latter, based on the appropriate cell dimensions, was confirmed to yield a proton conductivity value of $2.8 \pm 0.7 \times 10^{-2}$ S cm^{-1} at 250 ºC, consistent with the value of 2.4×10^{-2} S cm^{-1} reported in literature.[10] For reasons of clarity and for ease of comparison between spectra, the high-frequency, non-electrode contributions are subtracted from all impedance data presented in this work. A detailed discussion of the high-frequency impedance response is presented in Appendix C.3.

3.3 Results and Discussion

3.3.1 Film Morphology and Structure

A typical X-ray diffraction pattern of Pt deposited on CsH_2PO_4 (Figure 3.1, 75 nm Pt) shows broad Pt peaks[67] overlaid with monoclinic CsH_2PO_4 peaks.[68] The presence of Pt diffraction peaks, observed even for films as thin as 7.5 nm (not shown), indicates that the deposited film is crystalline in nature, whereas the peak breadth suggests a small grain size.

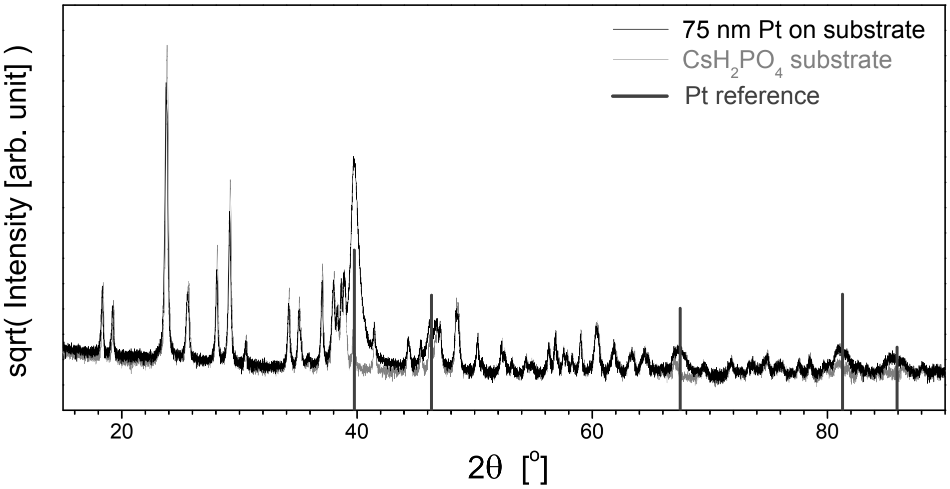

Figure 3.1 A representative X-ray diffraction pattern of as-deposited Pt films on a polycrystalline CsH_2PO_4 substrate. Visible are broad Pt peaks, the most prominent at 2θ = 39.8°, overlaid with monoclinic CsH_2PO_4 peaks. Pt film shown: 75 nm thick,15 mm dia.

Representative scanning electron micrographs of Pt on CsH_2PO_4 are shown in Figure 3.2. The plane-view image of an as-deposited 75 nm film (Figure 3.2a), shows that the Pt conforms to the substrate, revealing the underlying grains of CsH_2PO_4, 0.4–5 µm in size, as well as streaks due to polishing. From the cross-sectional image of a 375 nm film (Figure 3.2b), it is apparent that the films are dense and formed of nanometric grains. The film has slightly detached during fracture, giving rise to the small gap at the interface. The conformal and dense nature of the films (away from the edge) is further evident from Figure 3.2c, in which an SEM micrograph of the underside of a 7.5 nm Pt film isolated from its CsH_2PO_4 substrate is shown. As is the case for all films examined, the morphology of the substrate is replicated and the film appears free of pores.

The conformal and dense nature of the as-deposited films is ideal for the intended electrochemical study because the TPB sites are limited to the film perimeter region. The boundaries, however, are defined by sloped rather than sharp edges, Figure 3.2d, suggesting possible increases to the TPB length relative to an ideal boundary. The slope is so gradual, in fact, that the boundary is barely visible in the high magnification image. Furthermore, and perhaps more significantly, changes in film morphology were observed as a consequence of thermal cycling. The superprotonic transition in CsH_2PO_4 involves a large volume change and structural rearrangement, and this transformation was found to generate microcracks in the electrolyte, which then propagate into the Pt film. The SEM image in Figure 3.2e shows a representative image of the boundary region of Pt films on CsH_2PO_4 after thermal cycling. While microcracks were not, in any instance, observed in as-deposited films, cracks of the type evident in the figure were ubiquitous after thermal cycling. It is evident that microcracks extend from the Pt-free region of the substrate into that on which Pt has been deposited, indicating that the electrolyte is indeed the source of the cracks in the film. The density of TPB sites generated by such cracks is $\sim 0.018 \pm 0.004\ \mu m^{-1}$, estimated by measuring the number and lengths of cracks across ten SEM images. On average, the sheet resistance of the Pt films increased by ~ 35% after testing, consistent with the formation of microcracks through the film.

Based on observations of the film characteristics, the structure of the gas | Pt | CsH_2PO_4 half-cell differs from that expected for a perfectly dense film. Figure 3.3 shows a schematic of the structure.

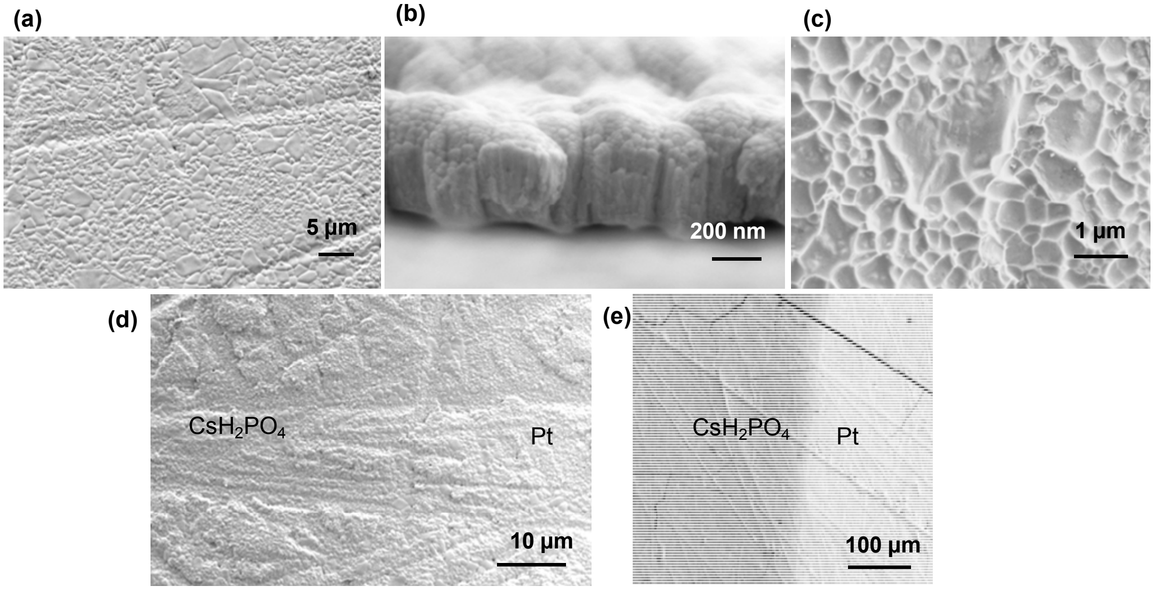

Figure 3.2 SEM micrographs of Pt films: (a) as-deposited 75 nm Pt on CsH_2PO_4, (b) as-deposited 375 nm thick Pt film in cross-section, (c) underside of as-deposited 7.5 nm film isolated from its substrate, (d) Pt-CsH_2PO_4 boundary for a 375 nm Pt film, and (e) Pt-CsH_2PO_4 boundary for a 375 nm film after electrochemical characterization at 250 ºC. Additional images of Pt films are shown in Appendix C.2.

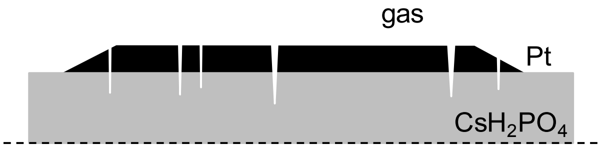

Figure 3.3 A schematic of the Pt | CsH_2PO_4 | Pt cell, with the plane of symmetry denoted by a dashed line. Microcracks, resulting from heating the substrate to above the superprotonic phase transition temperature, are generated in the Pt films.

High resolution SEM images and diffraction data, Figure 3.4 and Figure 3.5, respectively, indicate that the Pt grain size increases with film thickness. While difficult to quantify from the SEM micrographs, the increasing breadth of the (111) diffraction peak with decreasing film thickness is immediately evident in Figure 3.5a, in which the normalized diffraction intensities are compared for a series of films post electrochemical characterization. The particle size implied by the Scherer equation (microstrain effects are considered negligible) is plotted as function of thickness in Figure 3.5b. The grain size depends sharply on film thicknesses for films thinner than ~ 50 nm and then apparently tends towards a finite value with increasing thickness. Selected evaluations of as-deposited films revealed similar grain sizes, indicating that minimal Pt grain growth occurs under the electrochemical characterization conditions (250 ºC, total time ≈ 4 days), an expected result.

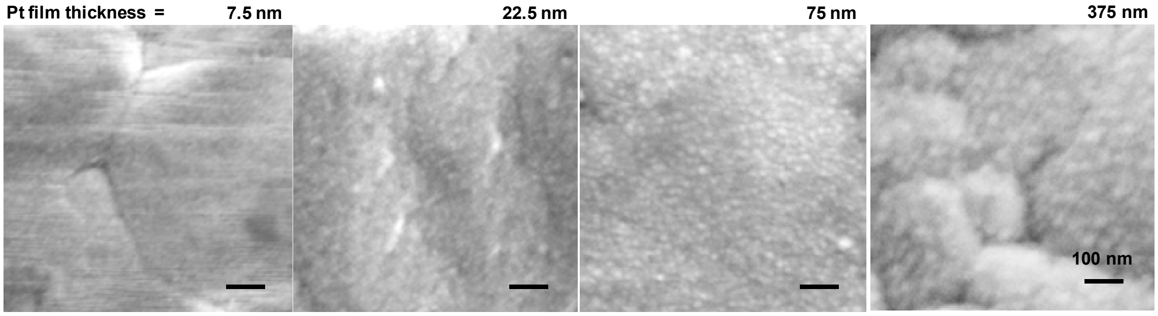

Figure 3.4 High magnification SEM micrographs of Pt of various thicknesses on top of CsH2PO4 (imaged after electrochemical characterization), showing the Pt grain structure.

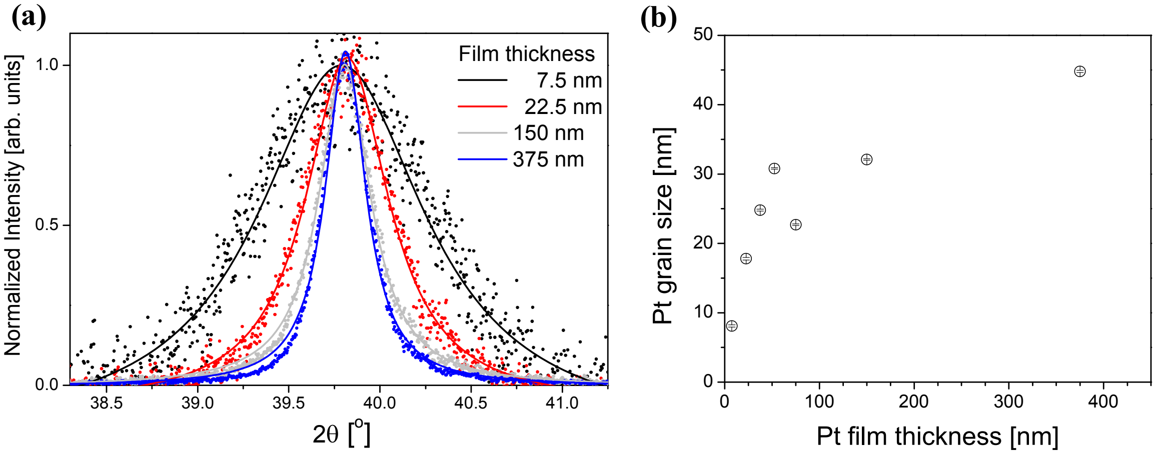

Figure 3.5 Correlation of grain size with Pt film thickness: (a) the broadening of the (111) diffraction peak for Pt at 2θ = 39.8°, shown here for select films, and (b) Pt grain size as a function of film thickness determined from (a). Films measured were isolated from CsH_2PO_4 substrate (after electrochemical characterization).

3.3.2 Impedance Response: Effect of Platinum Film Dimension

Representative impedance spectra collected from the symmetric Pt | CsH_2PO_4 | Pt cells are presented in Figure 3.6. For this series of spectra, in which the film diameter is held constant (15 mm) and the film thickness is varied, it is apparent that the nature of the impedance response differs between thick and thin films. Specifically, the thicker films displayed a response in the Nyquist representation (Figure 3.6a) that appeared as an asymmetric arc, with a 45° slope at high frequencies and circular appearance at low frequencies. This half-teardrop shape is functionally described by a “distributed” finite-length Warburg diffusion element, Z_{dFLW}, with impedance

$$Z_{\mathrm{dFLW}}(i\omega) = R_0 \frac{\tanh\left[(i\omega\tau)^n\right]}{(i\omega\tau)^n} \tag{3.1}$$

where i is $\sqrt{-1}$, ω is angular frequency, τ is the characteristic diffusion time, R_0 corresponds to the real impedance at the low-frequency limit (as indicated in Figure

3.6a), and n is a constant whose deviation from 0.5 reflects the dispersion of the response due to non-uniform diffusion.[34] The solid lines in Figure 3.6(a–b) show the high quality of the fit using this expression and thus the suitability of this function for representing the measured response. It is further apparent that for thicker films, R_0 increases with film thickness.

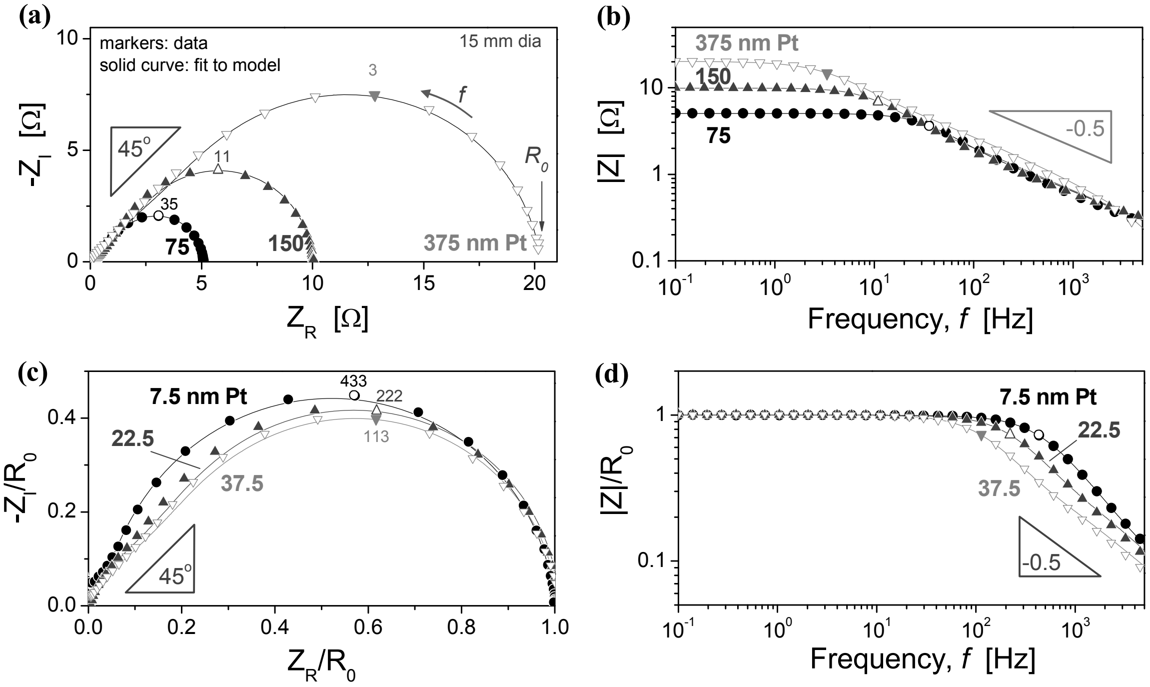

Figure 3.6 Impedance spectra for select Pt film electrodes of different thicknesses (15 mm dia.): (a) Nyquist and (b) Bode magnitude representations for thicker films, and (c) Nyquist and (d) Bode magnitude representations of thinner films. Thick Pt films yield a characteristic half-teardrop shape in the Nyquist plot (a), whereas thin Pt films yield a more symmetric response (c). For the thin films (c–d), the impedance response is normalized by the arc width to show the transition in arc shape from half-teardrop to semi-circle. Lines indicate fits to the distributed finite-length Warburg element, with the exception of the 7.5 nm Pt film which was fitted using two parallel RQ sub-circuits.

In contrast, the thinner films, Figure 3.6(c–d), displayed responses that are not adequately represented by Equation (3.1). With decreasing film thickness, the electrode arc became increasingly symmetric and the 45° slope at the high-frequency limit was almost absent for the 7.5 nm film. The solid lines in this case are fits using two parallel RQ sub-circuits, where R is a resistor and Q is a constant phase element ($Z_Q = 1/Y(i\omega)^n$, where Y is a constant and $0 \leq n \leq 1$) placed in series with one another. Moreover, although the spectra are presented in normalized form for ease of comparison of the shapes, it was found (as will be shown quantitatively below) that R_0 is almost independent of film thickness for films thinner than ~ 50 nm.

The characteristics represented by the spectra for 15 mm diameter Pt films in Figure 3.6 were observed to be independent of film diameter. That is, irrespective of diameter, all films with thickness ≥ 50 nm displayed the type of response shown in Figure 3.6(a–b), whereas all films thinner than 50 nm showed increasingly symmetric arcs, as shown in Figure 3.6(c–d). For either type of response, it is possible to evaluate the real impedance of the electrode in the DC limit, explicitly noted as R_0, in Figure 3.6a. The results are summarized in Figure 3.7, in which R_0 is plotted in double-logarithmic form as a function of film thickness (Figure 3.7a) and of film diameter (Figure 3.7b). The trends shown in Figure 3.7a reflect a clear differentiation between regimes. For thicker films (Regime I), which exhibited the half-teardrop response, the double-logarithmic plot displays an average slope of 0.9 ± 0.1, revealing that R_0 scales linearly with thickness. Thinner films (Regime II), in contrast, tend towards an apparently limiting value of R_0, with further reductions in film thickness having negligible impact. It is noted that reliable impedance measurements could not be made using films thinner than 7.5 nm because of loss of connectivity in the film (Appendix C.2.2). Turning to the diameter dependence of R_0 (Figure 3.7b), it is evident that for all films, the data fall along a line with an average slope of -2.1 ± 0.1, indicating that R_0 is inversely proportional to the area of the Pt film.

The behavior of R_0 as a function of temperature and hydrogen partial pressure (Figure 3.8) further suggests a mechanistic distinction between thicker (Regime I) and thinner (Regime II) films. Specifically, the reaction order for pH_2 (i.e., r in $R_0^{-1} \propto pH_2^{\,r}$) is roughly constant at ~ 0.4 for thicker Pt films (Regime I) but increases sharply with decreasing film thickness (Regime II), yielding a value of ~ 0.75 for 7.5 nm films. Likewise, the activation energy for R_0^{-1} is somewhat flat in Regime I, with a value of ~ 42 kJ mol^{-1} for film thicknesses ≥ 150 nm and decreasing with decreasing film thickness to ~ 27 kJ mol^{-1} at 7.5 nm.

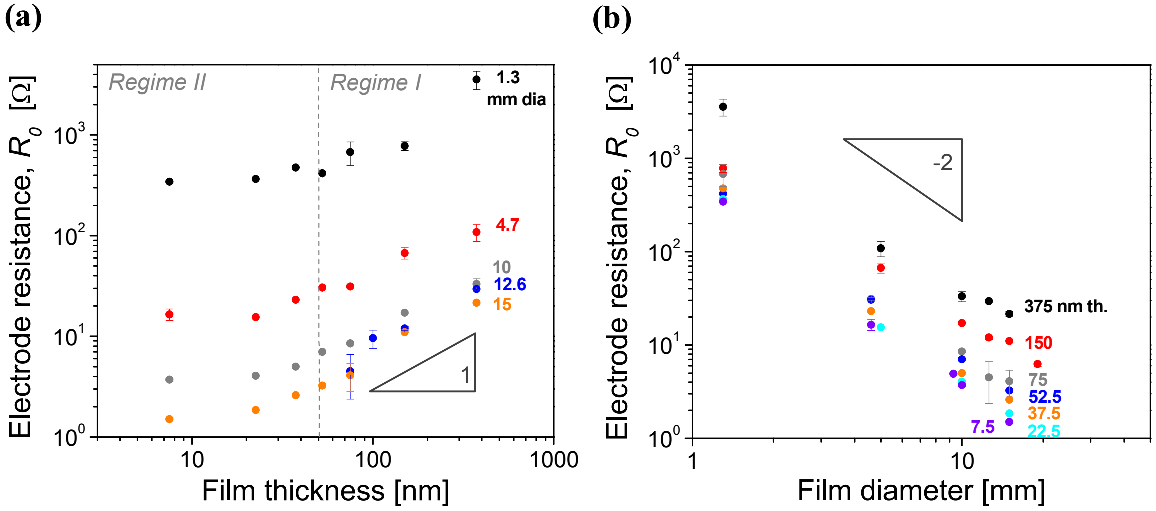

Figure 3.7 Double-logarithmic plots of Pt film electrode resistance, R_0, as a function of: (a) film thickness for various diameters and (b) film diameter for various thicknesses. The thickness dependence reveals two different regimes: data fall along lines with a slope of 1 for thicker films but show little dependence for films below ~ 50 nm. For all Pt films, R_0 scales with film area.

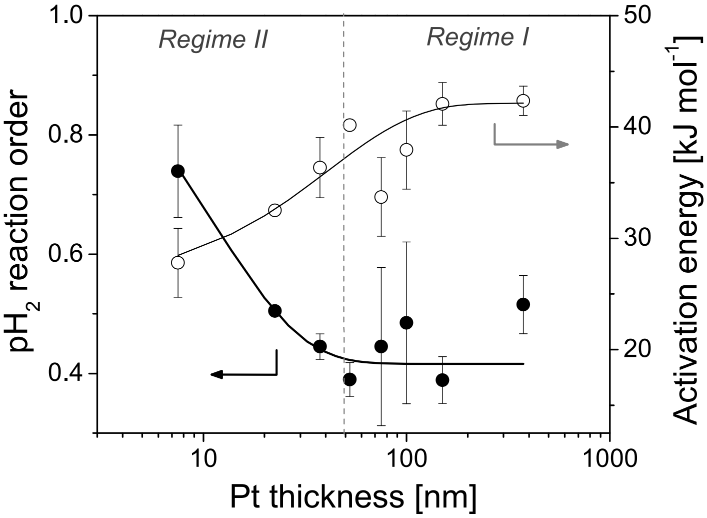

Figure 3.8 Plot of the pH_2 reaction order and the activation energy of the electrode process as a function of film thickness, showing a change in mechanism with film thickness.

The combination of the observed geometric (thickness and area) dependences of both the absolute value of R_0 and the form of the impedance response can be interpreted as follows. In all cases examined, the rate-limiting step occurs at sites that scale in number density with film area. For thicker films, diffusion to access these sites is rate limiting, giving rise to the linear dependence of R_0 on film thickness and the characteristic half-teardrop shape of the impedance response. For thinner films, diffusion no longer plays a role in limiting the rate of the process, however, the pathway continues to involve sites distributed through the film area. For truly dense films, one could readily conclude from these results that, for the range of film geometries examined, TPB sites do not contribute to the measured electrochemical activity. Even the sloped, irregular film boundaries do not create a significant concentration of active sites as this would lead to a diameter rather than area dependence of the overall activity. However, the existence of cracks throughout the films that cause an increase in the TPB site density in a manner that scales with film area precludes a definitive conclusion simply based on geometric arguments. To address this ambiguity, we turn to the results obtained from cells in which Au was applied atop the Pt films.

3.3.3 Impedance Response: Impact of Gold Overlayers

SEM imaging of Au | Pt films with ~ 10 nm Au deposited on 75 nm Pt (not shown) revealed that the bilayer films attained morphologies essentially identical to those with Pt only (e.g., Figure 3.2). That is, the as-deposited films were crack-free, but after a thermal cycle microcracks were evident throughout the film area. Given that the cracks formed after Au deposition, all TPBs generated as a result of cracking are taken to be free of Au and thus equally active as those formed in the absence of Au. The inferred geometry is presented in Figure 3.9.

A comparison of the impedance responses for samples (75 nm Pt) with and without an Au overlayer (10 nm Au) reveals the dramatic impact of changing the nature of the exposed metal surface on the overall reaction impedance, Figure 3.10. The two spectra overlap almost perfectly at high frequencies ($f > 600$ Hz) at which the spectra are linear with a 45º slope in the Nyquist representation (Figure 3.10a). They deviate substantially at intermediate and especially low frequencies, and the DC electrode resistance is over an order of magnitude higher in the presence of Au (Figure 3.10b). The retention of the linear, 45º phase angle response at high frequencies upon deposition of Au is evidence that the diffusive process is retained. The dramatic increase in the absolute resistance at low frequency, on the other hand, reveals that the overall electrochemical reaction pathway must involve a step at the Pt | Au | H_2 interfaces. That is, the diffusion step must occur in serial with a step at these interfaces, where the interfacial step(s) becomes extremely slow in the presence of Au. These results thus rule out the possibility that TPBs generated by cracking play any significant role on the electro-oxidation of hydrogen for the film geometries employed here.

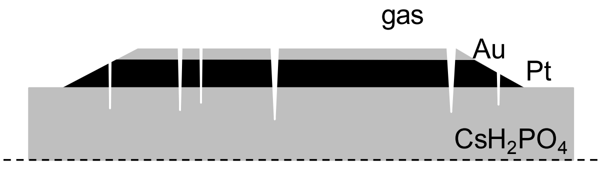

Figure 3.9 A schematic of the Au | Pt | CsH_2PO_4 | Pt | Au symmetric cell, with the plane of symmetry denoted by a dashed line. Microcracks, resulting from heating the substrate to above the superprotonic phase transition temperature, are propagated to the Pt | Au film.

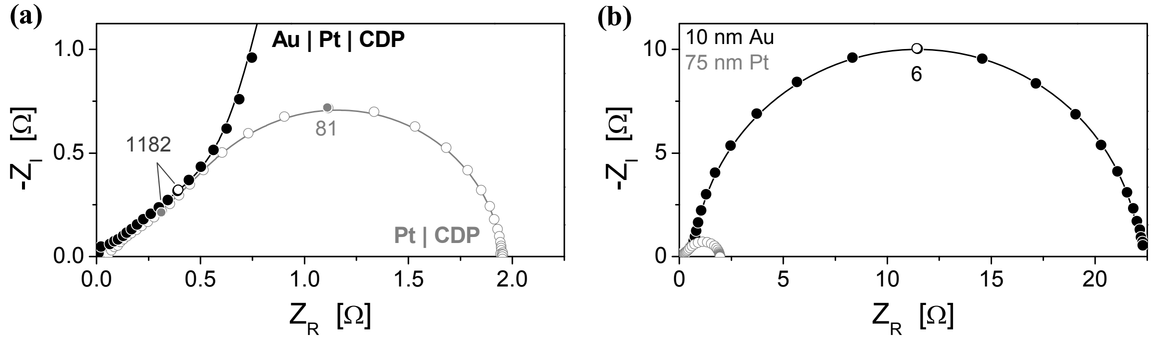

Figure 3.10 Comparison of electrode responses from Au | Pt | CsH_2PO_4 | Pt | Au and Pt | CsH_2PO_4 | Pt symmetric cells (15 mm dia. films, 10 nm Au, 75 nm Pt): (a) At high frequencies, both spectra overlap and exhibit a phase angle of 45º, while (b) at lower frequencies, the behavior the Au | Pt cell deviates significantly from that of the Pt cell.

3.3.4 Diffusion Analysis

With bulk diffusion through Pt having been revealed as the rate-limiting step for thicker films, the impedance data can be used for the determination of diffusion parameters. Specifically, the impedance response for the diffusion of a neutral species through a medium bounded by reversible planes/electrodes[33] has the form given in Equation (3.1), with $n = 0.5$ and $\tau = L_F^2 / \tilde{D}$, where L_F is the film thickness and $\tilde{D}$ is the (ambipolar) diffusion of a neutral species, taken here to be interstitial hydrogen (irrespective of possible dissociation into protons and electrons or into hydride ions and holes).[31, 69] When the solution furthermore behaves ideally (dilute solution limit), the resistance in the DC limit is given by

$$R_0 = \frac{k_B T}{e^2 D_H c_H} \frac{L_F}{A_F} \tag{3.2}$$

where k_B, T and e have their usual meanings, c_H is the concentration of hydrogen in the Pt film, and A_F is the film area. An absolute valence of 1 is assigned to the transported species which is ultimately incorporated as protons at the Pt | CsH_2PO_4 interface. (The derivation of Equations (3.1) and (3.2) are shown in Appendix A.2.) Although n in Equation (3.1) is strictly 0.5 for a finite-length Warburg diffusion response, treating it as a fitted parameter, as was done here, provides an indication of microstructural imperfections/variations present in the films. Across 44 samples, n ranged from 0.41 to 0.58, a relatively small deviation from 0.5, with an average value of 0.48 ± 0.03. Moreover, no correlation between n and any obvious experimental conditions or parameters was observed, suggesting that random sample-to-sample variations in film microstructure are responsible for the slight scatter.

Analysis of the impedance data of 44 symmetric cells in the manner described above yielded hydrogen diffusion coefficients (D_H) and concentrations (c_H) on the order of 10^{-12} m^2 s^{-1} and 10^{-4} H/Pt, respectively, Table 3.1. Over the relatively narrow temperature window explored, c_H was largely unchanged, whereas from the temperature dependence of D_H an activation energy of 47 ± 6 kJ mol^{-1} was determined. It is not possible to directly compare these values to those in the literature because all other reported studies address different temperature ranges. Extrapolation of literature values[70–73] to the temperatures examined here suggest a hydrogen diffusion coefficient in the range of 10^{-12} to 10^{-9} $m^2\,s^{-1}$ and a concentration in the range 10^{-8}–10^{-4} H/Pt. The present values, though apparently reflecting low diffusivity and high solubility, lie within these ranges and are physically realistic. Reported activation energies for Pt[70–73] are between 25 to 40 kJ mol^{-1}, the wide scatter likely being a consequence of the low solubility of hydrogen in this metal. While the value measured here, 47 ± 6 kJ mol^{-1}, is somewhat high relative to this range, given the uncertainty in the literature data and the atypical temperature regime of the present study, it is reasonable to accept that the measurement reflects the same general type of process.

Beyond the expected temperature dependence of D_H, an unexpected dependence on film thickness was observed, Figure 3.11. Notably, c_H displayed an approximately inverted dependence on film thickness such that the product $D_H \times c_H$ remained approximately constant (not shown). Given the dependence of average Pt grain size on film thickness, Figure 3.4 and Figure 3.5, such behavior immediately suggests that the hydrogen transport mechanism depends on microstructure in a systematic manner. Specifically, the combination of somewhat high activation energy for hydrogen transport, low value of D_H, and microstructure dependence all suggest bulk diffusion through the films with grain boundaries as trapping sites. More significant in the present context than the details of hydrogen transport through Pt, is the fact that the absolute values of D_H and c_H support the surprising conclusion that the hydrogen electro-oxidation pathway involves hydrogen diffusion through the bulk of the films. Thus, for the range of geometries explored, the process is limited by the quantity of two-phase boundary sites (either Pt | gas or Pt | CsH_2PO_4) rather than the quantity of three-phase boundary sites.

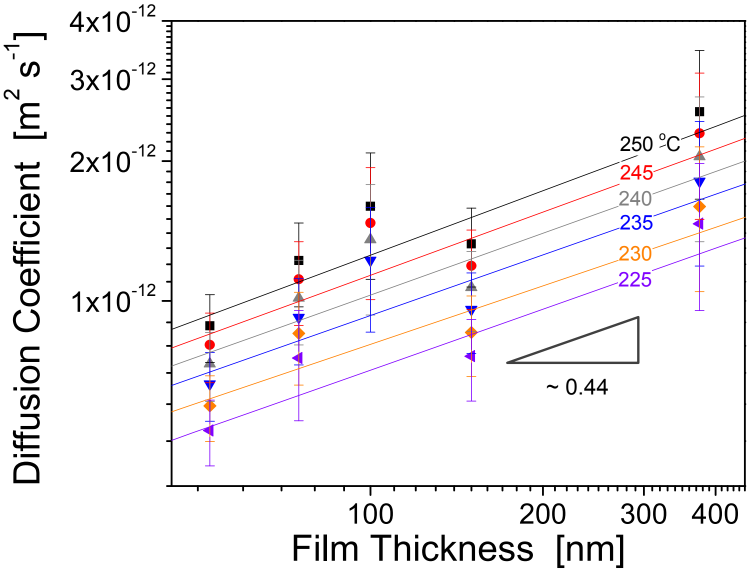

Figure 3.11 A plot of the extracted hydrogen diffusion coefficient as a function of film thickness for several temperatures. Error bars indicate the scatter of the value over several samples. Linear fits to each data set yield slopes with an average value of 0.44.

Table 3.1 Experimentally-determined parameters for hydrogen transport in Pt, shown for two temperatures. Values reported are taken from averaging over films greater than 50 nm in thickness.

T [ºC]	D_H [× 10^{-12} m^2 s^{-1}]	c_H [× 10^{-4} H/Pt]
250	1.6 ± 0.7	2.4 ± 0.8
225	0.9 ± 0.5	2.8 ± 0.8

3.3.5 Ultra-thin Platinum Films

For the thinnest films for which reliable data could be obtained (7.5 nm), the change in the features of the impedance response from those of thicker films is most certainly due to a change in the nature of the rate-limiting step. As the transport distance is decreased, diffusion limitations are relaxed, and interfacial effects at either or both the Pt | gas and Pt | CsH_2PO_4 boundaries become rate limiting. In the absence of transport of a neutral species as the dominant response, the impedance response is expected to adopt a characteristic symmetric shape in the Nyquist representation, and the Z_{dFLW} element becomes inadequate for representing the response. An equivalent circuit with two parallel RQ sub-circuits placed in series with one another was used to analyze the data, as shown in Figure 3.6(c–d). From this analysis, we find the total electrode resistance, across twelve different samples, to have a value of 3.1 ± 0.5 Ω cm^2.

For the serial set of steps suggested by this analysis, the total, area-normalized electrode resistance, $\tilde{R}$, is expected to be the simple sum of the interfacial reaction resistance(s), $\tilde{R}_{\mathrm{rxn}}$, and the thickness-dependent diffusion resistance, $\tilde{R}_D^* L_F$:

$$\tilde{R} = \tilde{R}_{\mathrm{rxn}} + \tilde{R}_D^* L_F \tag{3.3}$$

The area-normalized data from Figure 3.7a indeed collapse into a single curve, Figure 3.12, which, in the double-logarithmic plot, display the expected flat regime at small film thickness and regime of slope 1 at large film thickness. The fit to Equation (3.3), also shown in the figure, implies $\tilde{R}_{\mathrm{rxn}} = 2.2\ \Omega\ \mathrm{cm}^2$ and $\tilde{R}_D^* = 0.081\ \Omega\ \mathrm{cm}^2\ \mathrm{nm}^{-1}$. For the thinnest film that could be evaluated (7.5 nm) with a total electrode resistance of 3.1 ± 0.5 Ω cm^2, the diffusion contribution is 0.9 Ω cm^2, or approximately 27% of the total. Thus, both interfacial and bulk effects play a role even in very thin films.

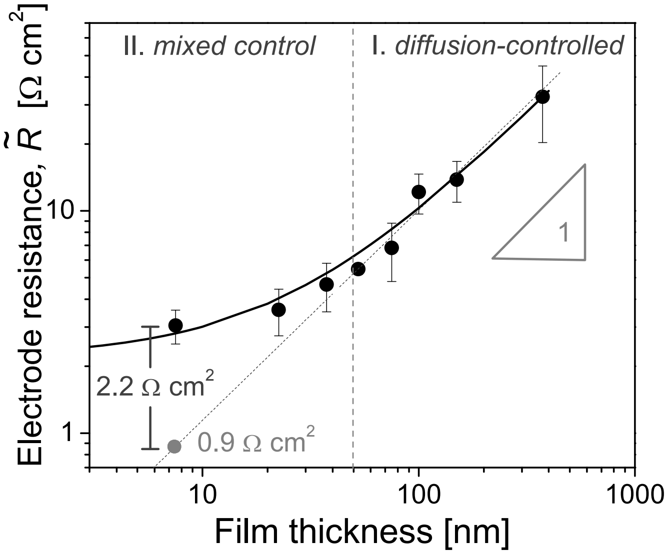

Figure 3.12 Area-normalized electrode resistance plotted against film thickness for all Pt | CsH_2PO_4 | Pt cells tested in this study. The solid curve corresponds to Equation (3.3), and the surface resistance was determined by extrapolation of the resistance due to diffusion to a Pt film thickness of 7.5 nm (dotted line).

3.4 Implications for Electrode Design

Platinum is known to display relatively poor hydrogen permeation characteristics and accordingly was not anticipated to facilitate hydrogen electro-oxidation via a bulk diffusion pathway. The dominance of the two-phase boundary pathway over the triple-phase boundary pathway results, in part, from the thin film geometry employed, which maximizes the Pt | CsH_2PO_4 interfacial area while minimizing the number of triple-phase boundary sites. In principle, the triple-phase boundary activity would be accessed by increasing the thickness platinum until the two-phase boundary pathway, governed by hydrogen diffusion through the film, is effectively blocked. However, because physical shadow masks are limited to relatively large areas (the smallest diameter used here was 1 mm), unrealistically thick films of Pt would be needed. An estimate of the lower bound for the resistance of the triple-phase boundary pathway is instead made using impedance data acquired from electrode films with configurations similar to that shown in Figure 3.9. Specifically, blocking studies with 50 nm Au films yielded electrode resistances as high as 225 Ω cm^2, while retaining diffusion characteristics at high frequencies of the type evident in Figure 3.10. The shape of the spectra implies that even with such extreme resistance in the blocking layers, the triple-phase boundary pathway is not favorable and can be used to establish the maximum activity of TPB sites. Based on a TPB density of ~ 180 cm^{-1}, the lower bound for the triple-phase boundary resistance is estimated at ~ 41 kΩ cm.

Irrespective of the absolute resistance values, one can expect the triple-phase boundary pathway to overtake the two-phase boundary pathway for Pt dimensions (diameter and thickness) which provide sufficient triple-phase site density relative to the two-phase interfacial area. One can speculate that a continuous Pt film with nanometric pores would lead to maximum overall activity. For a two-phase boundary resistance of 3.1 Ω cm^2 and a minimum TPB resistance of 41 kΩ cm, an area-to-perimeter ratio of ~ 7.6 μm or less is required to observe comparable total activity between two-phase and three-phase boundary sites in films with thickness 7.5 nm. While eventual fabrication of such structures could likely be achieved, because of the uncertainty with respect to the TPB site activity, there is no guarantee that such electrodes would, in fact, provide higher activity than the dense films examined here. Furthermore, films provide the inherent advantages of high electronic conductivity and good thermal stability.

These factors prompt a direct comparison of the activity of dense Pt thin films to state-of-the-art composite electrodes employed in solid acid fuel cells, Table 3.2. The absolute (area-normalized) resistance of the 7.5 nm film is within a factor of two of that of composite electrodes formed solely of nanoparticulate Pt and CsH_2PO_4. Specifically, electrodes fabricated by electrospray deposition[27] and by mechanical mixing[36] yield comparable resistance values of 1.5 and 1.7 Ω cm^2, respectively. Pre-commercial solid acid fuel cells, in which Pt/C is also an electrode component and thus take advantage of carbon to enhance electronic conductivity, have much smaller electrode resistances, just 0.06 Ω cm^2.[10] Although the thin film Pt electrode displays the highest resistance, the amount of Pt applied is the lowest (by a factor of 10–500 in mass) such that the Pt utilization or mass-normalized activity ($\tilde{R}^{-1}$/Pt loading) is the highest, 19 S mg^{-1}. The poor activity in the nanoparticulate cases suggests a large fraction of the Pt is not utilized because of the lack of electronic connectivity. The results further suggest that increasing the overall electrode activity can be increased simply by increasing the projected Pt | CsH_2PO_4 contact area. Promising results taking advantage of precisely such an electrode geometry, albeit targeting the cathode, have been recently reported.[3, 28] In that work, a uniform Pt coating is applied to sub-micron CsH_2PO_4 powders using a metal organic chemical vapor deposition method.[28] A decrease in the CsH_2PO_4 particle size led to a monotonic decrease in electrode resistance[3] indicating the importance of the total Pt | CsH_2PO_4 surface area. Using such techniques, one can readily envision a substantial increase in specific surface area over that of a flat interface, and from the quantitative studies reported here, the impact on performance metrics can be assessed. For CsH_2PO_4 particle-based electrodes of moderate thickness, we presume the activity will scale linearly with surface area, and thus, a 50-fold increase in the specific surface area, for example, will decrease the electrode resistance to a highly attractive value of ~ 0.06 Ω cm^2 for the 7.5 nm thick film. The Pt loading will also increase proportionally, but would remain at just 0.86 mg cm^{-2}. Thus, thin, continuous film electrodes have the potential to dramatically reduce Pt loadings while also enhancing power output.

Table 3.2 Comparison of platinum-based anodes for solid acid fuel cells at temperatures of 238–250 ºC. $\tilde{R}$ = area-normalized electrode resistance

Electrodes	$\tilde{R}$ *Ω cm^2*	Pt loading *mg cm^{-2}*	$\tilde{R}$ / Pt loading *S mg^{-1}*
7.5 nm Pt film – *sputtered (this work)*	3.1 ± 0.5	0.017	19
Pt:CsH_2PO_4 (1:2) – *electrosprayed* [27]	1.5	0.3	2.2
Pt:CsH_2PO_4 (1:2) – *mech. mix.*[36]	1.7	10	0.059
Pt:Pt/C:CsH_2PO_4 (3:1:3) – *mech. mix*[10, 25]	0.06	7.7	2.2

3.5 Summary

The rate-limiting step for hydrogen electro-oxidation over Pt thin film electrodes has been identified. Pt films between 7.5 and 375 nm thick were determined to electrocatalytically oxidize hydrogen via the two-phase boundary pathway. Pt films greater than 50 nm in thickness are rate-limited by diffusion of hydrogen through the film, whereas for films thinner than 50 nm, interfacial processes, with a resistance of 2.2 Ω cm^2, begin to overtake diffusion as the rate-limiting step. That the two-phase boundary pathway is preferred over that three-phase boundary pathway has significant implications for the design of electrodes in solid acid fuel cells. Specifically, electrodes based on 7.5 nm Pt films with electrode resistances of 3.1 Ω cm^2, have the potential to reach state-of-the-art performances while using one order of magnitude less Pt by mass. This improvement is a consequence of the inherent interconnectivity of the platinum in the thin film configuration and the resulting improvement in catalyst utilization compared to conventional electrodes based on Pt nanoparticles.

Chapter 4 Oxygen Electro-reduction at Nano-Pt | $CsHSO_4$

Adapted with permission from: Louie, M. W.; Hightower, A.; Haile, S. M. Nanoscale Electrodes by Conducting Atomic Force Microscopy: Oxygen Reduction Kinetics at the Pt | $CsHSO_4$ Interface. *ACS Nano* **2010**, *4,* 2811–2821.

Abstract

We quantitatively characterized oxygen reduction kinetics at the nanoscale Pt | $CsHSO_4$ interface at ~ 150 ºC in humidified air using conducting atomic force microscopy (AFM) in conjunction with AC impedance spectroscopy and cyclic voltammetry. From the impedance measurements, oxygen reduction at Pt | $CsHSO_4$ was found to be comprised of two processes, one displaying an exponential dependence on overpotential and the other only weakly dependent on overpotential. Both interfacial processes displayed near-ideal capacitive behavior, indicating a minimal distribution in the associated relaxation time. Such a feature is taken to be characteristic of a nanoscale interface in which spatial averaging effects are absent and, furthermore, allows for the rigorous separation of multiple processes that would otherwise be convoluted in measurements using conventional, macroscale electrode geometries. The complete current-voltage characteristics of the Pt | $CsHSO_4$ interface were measured at various points across the electrolyte surface and reveal a variation of the oxygen reduction kinetics with position. The overpotential-activated process, which dominates at voltages below –1 V, was interpreted as a charge transfer reaction. Analysis of six different sets of

Pt | $CsHSO_4$ experiments, within the Butler-Volmer framework, yielded exchange coefficients (α) for charge transfer ranging from 0.1 to 0.6 and exchange currents (i_0) spanning five orders of magnitude. The observed counter-correlation between the exchange current and exchange coefficient indicates that the extent to which the activation barrier decreases under bias (as reflected in the value of α) depends on the initial magnitude of that barrier under open-circuit conditions (as reflected in the value of i_0). The clear correlation across six independent sets of measurements further indicates the suitability of conducting AFM approaches for careful and comprehensive study of electrochemical reactions at electrolyte-metal-gas boundaries.

4.1 Introduction

The power output of high-performance, thin-electrolyte fuel cells is, by definition, limited by the rate of electrochemical reactions at the electrode rather than by ion transport through the electrolyte. Accordingly, substantial effort has been directed towards understanding electrochemical reaction pathways and identifying rate-limiting steps, with the ultimate aim of developing new electrode materials and/or structures with enhanced activity. The vast majority of such electrochemical studies have relied on fuel cell electrodes of macroscopic dimensions, in some cases with geometrically well-defined structures[36–38, 46, 50, 53, 55, 58–60, 62, 74, 75] and in others with composite electrodes more directly relevant to technological applications.[39, 40, 76, 77] While such studies have led to important insights and advances, a comprehensive understanding of reaction pathways remains elusive for virtually every fuel cell type. It is to be expected that electrochemical reactions, which occur on surfaces that naturally display nanoscale heterogeneity, themselves occur at rates that are heterogeneous on the nanometer length scale. Thus, the limitations of macroscale measurements, which, by definition, cannot probe such heterogeneity and instead provide ensemble-averaged data with little information even about the distribution range of properties, may inherently complicate elucidation of electrochemical reaction pathways. Despite the recognition that nanoscale heterogeneity may play an important role in fuel cell electrode kinetics, few studies have been directed towards explicitly uncovering variations in electrochemical reaction rates and possibly even mechanisms at the nanometer scale.

In this work, we utilize conducting atomic force microscopy (AFM) for quantitative electrochemical characterization of metal | solid electrolyte interfaces.

Configurationally, the approach is similar to that employed in recent studies in which conducting AFM has been employed to evaluate nanoscale heterogeneity in the transport properties of ion conducting electrolyte materials.[78–83] The electrolyte material is contacted over its entire area to an electrochemically active counter electrode, Figure 4.1, and the conducting AFM probe contacted to the opposite surface. Because the electrolyte is electronically blocking, net current flow through the system requires electrocatalysis to occur at sufficient rates at both the counter and working (AFM tip) electrode. For the study of the distribution of ion conducting and insulating regions, as has been done for polymers[78–82, 84, 85] and more recently for ceramics,[83] it is sufficient to scan the electrolyte surface and differentiate between regions of high and low current flow. From such measurements, it is also possible to characterize the nature of contact between the probe and electrolyte.[24–25] Here, we evaluate the complete current-voltage characteristics at each point of interest on the electrolyte surface to study directly the kinetics of the electrochemical reaction and its nanoscale heterogeneity.

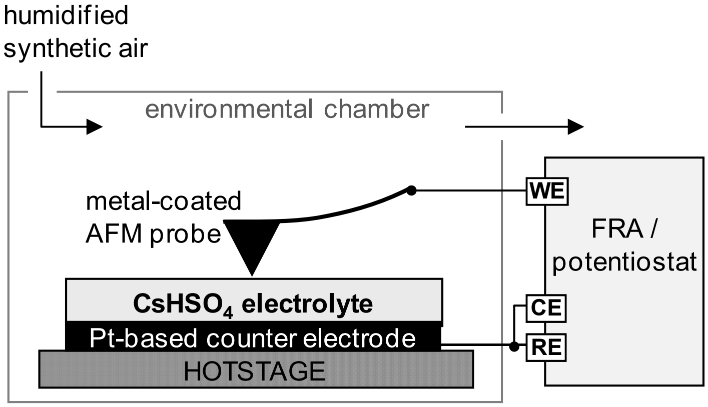

Figure 4.1 Schematic of nanoelectrode setup comprised of an atomic force microscope coupled with an external potentiostat and a frequency response analyzer capable of measuring fA current range. The hotstage can heat samples to temperatures as high as 240 ºC. The environmental chamber encloses the probe-sample assembly and is equipped with several inlet/outlet ports, enabling controlled atmospheres.

The electrolyte material selected for study in this work is $CsHSO_4$, a so-called superprotonic solid acid, which exhibits a proton conductivity of ~ 6×10^{-3} S cm^{-1} at a moderate temperature of 150 ºC.[6, 86] We consider it a representative material for superprotonic solid acids in general,[12] and specifically for those such as CsH_2PO_4 which have been demonstrated in fuel cells but require somewhat higher temperatures to attain comparably high proton conductivities.[1, 10] The electrochemical reaction of interest (examined at 150 ºC for all experiments in this study) is that of oxygen electro-reduction. The relevant global reaction for a proton-conducting electrolyte is given as

$$\tfrac{1}{2}O_{2(g)} + 2H^{+} + 2e^{-} \rightarrow H_2O_{(g)} \qquad (4.1)$$

An attractive feature of the conducting AFM geometry is the extreme asymmetry in the electrode areas. As discussed in detail elsewhere,[36] such asymmetry ensures that the overpotential (excess voltage drop relative to equilibrium) at the large counter electrode is negligible relative to that at the working (AFM tip) electrode. That is, because the current through each component of the cell is the same, the current density is orders of magnitude greater at the working electrode than it is at the counter electrode, and accordingly, the contribution of the counter electrode | electrolyte interface to the voltage drop measured across the system is negligible. Indeed, in the conducting AFM configuration, even the voltage drop across the electrolyte is negligible relative to that due to the finite kinetics at the working electrode. Thus, employing a nanoelectrode enables electrochemical studies of a single metal | electrolyte interface without the need for an external reference electrode, the placement of which has been shown to be problematic in solid electrolyte systems.[44, 45] Such a measurement directly yields the potential at the working electrode, referenced to the counter electrode, which, in turn, for the measurement temperature of ~ 150 ºC is at –1.13 V relative to $2H^+ + 2e^- \rightleftharpoons H_2$.

With this understanding, both cyclic voltammetry and AC impedance spectroscopy were used for quantitative electrochemical characterization. The former has the benefits of providing complete DC current-voltage characteristics at short timescales, before instrument drift becomes problematic, but cannot deconvolute resistance contributions resulting from multiple reaction steps. Impedance spectroscopy provides the benefits of deconvolution and, when carried out as a function of bias, can also provide complete current-voltage characteristics. The timescale of such measurements, however, is not sufficient to eliminate the possibility of a drifting probe | sample contact over the course of the experiment. The complementary information provided by these two techniques has proven to be indispensible in the present work.

4.2 Experimental

4.2.1 Half-cell Fabrication

$CsHSO_4$ powder was synthesized by rapid precipitation of a mixture of aqueous Cs_2SO_4 (99.99%, Alfa Aesar) and aqueous H_2SO_4 (95 wt% in water, EMD Chemicals) by acetone, followed by filtration and drying at ~ 100 ºC. Electrocatalyst mixtures were made from a toluene slurry comprised of Pt black (> 99.9%, fuel cell grade, Sigma Aldrich), Pt/C (40% on carbon black, Alfa Aesar), and $CsHSO_4$ in a Pt:Pt/C:$CsHSO_4$ weight ratio of 3:1:3; the slurry was sonicated and dried at ~ 100 ºC. Half-membrane electrode assemblies were fabricated by uniaxially pressing $CsHSO_4$ powder onto a

Pt:Pt/C:$CsHSO_4$ composite electrode supported on Toray paper (TGP-H-120) for 20 min at 490 MPa. The $CsHSO_4$ surface of the resulting half-cell was then polished with a ~ 2 μm grit silicon carbide cloth and blown with a dry air jet. Fabricated assemblies were 9.3 mm in diameter and 0.5–1 mm thick.

4.2.2 Experimental Conditions

Fabricated half-cells were mounted onto the hotstage of a PicoSPM atomic force microscope (Series 4500, Agilent Technologies) equipped with an environmental chamber and a scanner head with and *x-y* and *z* ranges of ~ 30 and ~ 6 μm, respectively. The temperature of the hotstage was set to ~ 170 ºC to attain a $CsHSO_4$ surface temperature of ~ 150 ºC. (The temperature gradient across the cell generated an open-circuit voltage of less than 1 mV.) Humidified synthetic air, generated by bubbling ~ 15 mL min^{-1} of air through water at room temperature (~ 0.02–0.03 atm H_2O), was continuously fed through the environmental chamber. Electrochemical characterization was carried out using an externally connected potentiostat equipped with a femtoammeter and a frequency response analyzer (ModuLab, Solartron Analytical) which were calibrated using high impedance circuits comprising of 0.01–100 GΩ resistors and 1–10 pF capacitors. Electrochemical characterization was carried out in potentiostatic mode; voltages are applied across the entire cell (probe | $CsHSO_4$ | composite electrode), with the probe as the working electrode and the large composite electrode serving as the counter and reference electrode. All voltages reported in this work are, therefore, with respect to the large composite counter electrode, that is, an air electrode reference which is –1.13 V relative to $2H^+ + 2e^- \rightleftharpoons H_2$ at ~ 150 ºC. To reduce contributions of external noise, the microscope was placed in a copper mesh Faraday cage which, like the shielding for the electrical leads, was grounded though the potentiostat ground. The microscope body, which was separately grounded, was electrically isolated from the cage. Stray capacitance and other spurious contributions were found to depend on the current range of the potentiostat, and therefore, open-circuit corrections were obtained by withdrawing the probe from the sample and taking impedance measurements at each current range. Point-wise open-circuit corrections were applied to all impedance spectra presented (Appendix F.2.1). Short-circuit measurements, obtained by contacting the conductive probe to a piece of gold foil, displayed the behavior of a pure resistor with a resistance on the order of 5 kΩ, negligible relative the high impedances of the nanoprobe setup employed in this work.

4.2.3 Measurement Conditions

Cyclic voltammograms were collected by sweeping between –1.1 and 0.5 V with scan rates, v, of 5–400 mV s^{-1}. Impedance measurements were carried out with a 100 mV perturbation about voltages ranging from –0.6 to –1.2 V with frequencies of 10^{6}–10^{-1} Hz. The acquisition time for each spectrum was ~ 2.5 min, and three spectra for each voltage were acquired. The working electrodes were metal-coated Si-based AFM probes (MikroMasch) with specifications shown in Table 4.1. A majority of the platinum data presented in this work are from Probes 1 and 3. Forces applied with the Pt probes were between 0.2 and 0.5 μN during electrochemical measurements and ~ 0.1 μN when rastering the surface for imaging. Stationary cyclic voltammograms collected as a function of position were comprised of three cycles at 100 mV s^{-1} (to attain stable voltammograms) followed by two cycles at 25 mV s^{-1} (used for quantitative analysis) for Probes 1–4, and five cycles at 100 mV s^{-1} for Probes 5–6. Impedance spectra at –1.0 and

–0.9 V were measured at select spatial positions to verify that that the primary features of the spectra had not changed. The thermal drift of ~ 0.1 nm s^{-1}, estimated by the imaging and tracking of surface features, impacts bias-dependent impedance measurements which required ~ 50 min acquisition time. On the other hand, cyclic voltammetry measurements required only several minutes of acquisition time (depending on the scan rate employed), and, moreover, the voltage range used for analysis only required ~ 30 s (corresponding to a drift of no more than 3 nm) to acquire.

Table 4.1 Conducting AFM probes employed in this study.

	Adhesion Layer	Spring Constant k [N m^{-1}]*	Total Tip Radius r_{tip} [nm]*
Probe 1	10 nm Pt on 20 nm Ti	5	40
Probe 2	10 nm Pt on 20 nm Ti	5	40
Probe 3	10 nm Pt on 20 nm Ti	5	40
Probe 4	10 nm Pt on 20 nm Ti	1.8	40
Probe 5	25 nm Pt on 5 nm PtSi	3.5	40
Probe 6	25 nm Pt on 5 nm PtSi	5	40
Probe 7	20 nm Au on 20 nm Cr	40	50

*nominal values

4.2.4 Data Analysis

Fitting of impedance spectra was carried out using the commercial package Zview (Version 2.9b, Scribner Associates, Inc.). Spectra were fitted using two parallel RQ sub-circuits in series. The value of n for the high-frequency arc, when treated as a free parameter during fitting, exceeded unity (by no more than 10%) and was therefore held fixed at 1. Such a fitting procedure yielded n values of 0.91–0.98 for the low-frequency process. Stray capacitance contributions, which are not negligible in such low current systems were accounted for by a point-wise open correction procedure, as shown in

Appendix F.2.1. Short-circuit measurements, obtained by contacting the conductive probe to a piece of gold foil, displayed the behavior of a pure resistor with a resistance on the order of 5 kΩ, negligible relative the high impedances of the nanoprobe setup employed in this work. The stability of the impedance measurements was verified by collecting the spectra by sweeping the frequency in both directions (Appendix F.2.2).

All cyclic voltammetry data were corrected for a non-zero offset current present in the system. Analysis of spatial variation of electrochemistry was done so using a voltammograms with a scan rate 25 mV s^{-1} which was determined to be sufficiently slow for measuring oxygen reduction kinetics but fast enough to minimize effects of thermal drift. (Appendix F.2.3). The magnitude of force applied between the probe and sample in the measurements was determined to have negligible impact on electrochemical results (Appendix F.2.4). To collect spatial variation data, the probe was lifted from the sample surface temporarily; we determined that this had no impact on the electrochemical measurements. (Appendix F.2.4)

4.3 Results and Discussion

4.3.1 Cyclic Voltammetry

An initial comparison between the behavior of Au and Pt was performed to verify that contact could be made between the electrolyte surface and the AFM probe. Cyclic voltammograms for Au | $CsHSO_4$ and Pt | $CsHSO_4$ are presented in Figure 4.2. The observation of low currents, ~ pA, is consistent with the small size of the AFM probe (tip radius ≈ 40 nm). Noise appearing in the voltammograms, resulting from a combination of the relatively low spring constant of the probe cantilever and elevated operating temperatures, is minimal and does not mask any of the salient characteristics. The voltammogram for Au | $CsHSO_4$ is featureless and displays less than 0.1 pA current across all voltages. In contrast, the voltammogram for Pt | $CsHSO_4$ exhibits a peak at –0.34 V (onset ≈ –0.1 V) overlaid with an overpotential-activated rise in current at negative biases. At –1.1 V, the measured current for Pt is ~ 15 pA, over two orders of magnitude higher than that for Au. These observations are consistent with the relative activities of bulk gold and platinum and confirm contact by the probe tip.

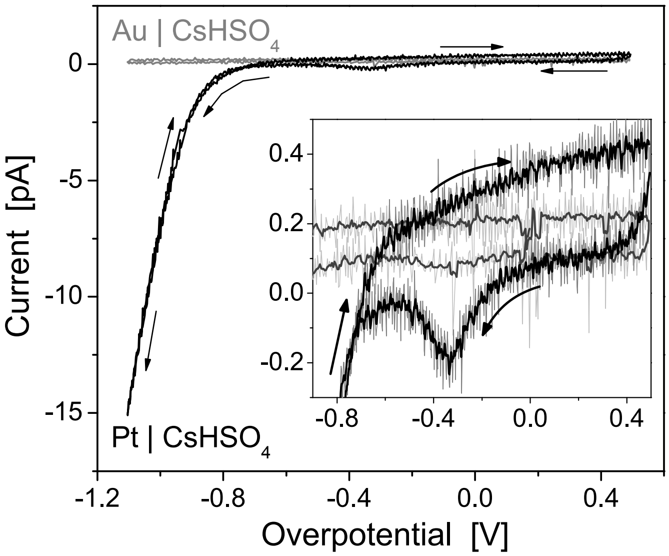

Figure 4.2 Comparison of typical cyclic voltammograms for Au | $CsHSO_4$ and Pt | $CsHSO_4$ collected at ~ 150 ºC in air (~ 0.03 atm H_2O) with a scan rate of 100 mV s^{-1}; the voltammograms shown are those obtained after cycling to ensure stability. Inset is an enlargement of the Pt oxide reduction peak at –0.34 V and displays both raw data (gray) and smoothed data (black). The applied force was ~ 2 and ~ 0.5 µN for Au and Pt, respectively. The Pt probe utilized is identified as Probe 3 in Table 4.1.

The peak evident in the Pt voltammogram is readily attributed to the reduction of platinum oxide. Based on calculations from thermodynamic data[87] for $T = 150$ ºC and $pO_2 = 0.21$ atm, reduction of PtO, PtO_2, and $Pt(OH)_2$ is expected to occur at –0.16, –0.14, and –0.06 V, respectively, whereas measured platinum oxide reduction potentials, for both smooth Pt surfaces in aqueous acidic electrolytes[88–90] and for Pt-carbon | Nafion systems,[84, 91, 92] range from –0.03 to –0.3 V, depending on temperature and experimental conditions. The total charge, ~ 0.5 pC, implied by the integrated area under the reduction peak and the scan rate, assuming the formation of any of the possible oxides, corresponds to the reduction of a plausible fraction of the Pt coating available on the AFM tip. The absence of a corresponding Pt oxidation peak on the reverse sweep indicates that chemical oxidation of Pt, which by definition, cannot generate a peak in the voltammogram, dominates the process of oxide formation over electrochemical oxidation.

While the Pt oxide reduction behavior on $CsHSO_4$ bears some similarities to that at the interface with aqueous and polymeric electrolytes, the Pt | $CsHSO_4$ system differs sharply from those in terms of interaction with hydrogen. In aqueous, acidic electrolytes or with polymer membrane electrolytes, hydrogen adsorption or desorption peaks are typically observed in the region between –0.8 and –1.2 V at temperatures between 25 and 150 ºC.[41, 84, 92–96] The absence of such peaks here suggests that hydrogen sorption onto the surface of Pt is negligible in the Pt | $CsHSO_4$ system. An unfortunate consequence of this behavior is that, in contrast to aqueous and polymer systems, hydrogen adsorption peaks cannot be used to estimate the surface area of Pt available for electrocatalysis in solid acid fuel cell electrodes. Similarly, without further information on the characteristics of

Pt oxide reduction, the corresponding peak in the voltammogram cannot be employed for determining the Pt | $CsHSO_4$ contact area.

4.3.2 Impedance Spectroscopy

Selected impedance spectra representative of oxygen reduction at the Pt | $CsHSO_4$ interface are presented as Nyquist plots in Figure 4.3 and Figure 4.4. While the bulk of the experimental details regarding acquisition of such spectra are provided in the Experimental section and in Appendix F.2, some aspects are highlighted here because the high impedance of the Pt | $CsHSO_4$ system in the nanoprobe geometry requires special consideration with respect to effects from external noise. All spectra collected were corrected with an open-circuit measurement which accounted for stray capacitance and other spurious contributions, and furthermore, the impedance analyzer was calibrated with precision circuits comprised of high resistance (0.01–100 GΩ) and low capacitance (1–10 pF) elements comparable in value to those measured in the present nanoprobe system. We also verified that the impedance response is stable, i.e., the spectra features are not transient artifacts, by examining the agreement between two spectra collected consecutively at –1.0 V, with one measured by sweeping the frequency in the opposite direction of the other (see Appendix F.2.2). With these precautions taken, the general features of the experimental data were found to be satisfactorily reproducible.

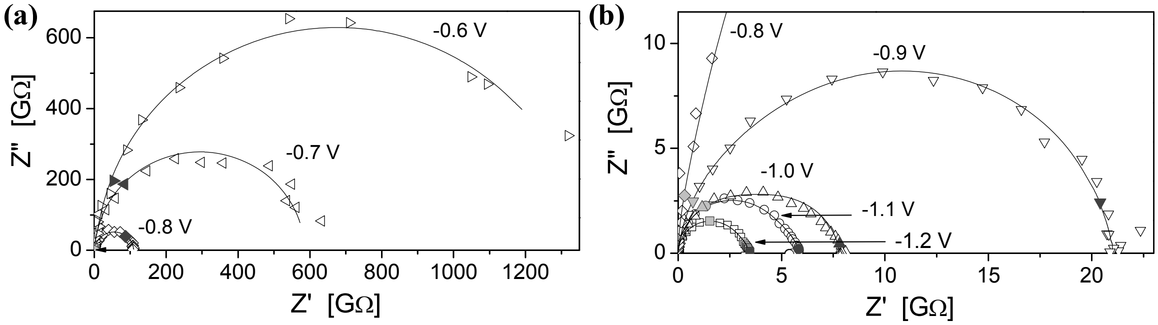

Figure 4.3 AC impedance spectra for Pt | $CsHSO_4$ as a function of overpotential, collected at ~ 150 ºC in humidified air (~ 0.03 atm H_2O), for overpotentials between (a) –0.6 and –0.8 V, and (b) –0.8 and –1.2 V. The filled data points correspond to frequencies of 200 and 2 Hz, and solid curves indicate equivalent circuit fits to two parallel *RQ* sub-circuits in series. The Pt probe utilized is identified as Probe 3 in Table 4.1.

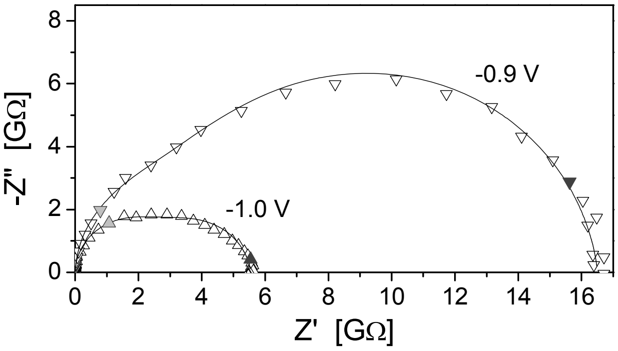

Figure 4.4 Typical impedance spectra for Pt | $CsHSO_4$ at overpotentials of –1.0 and –0.9 V, collected at ~ 150 ºC in humidified air (~ 0.03 atm H_2O), showing the presence of two processes. The filled data points correspond to frequencies of 200 and 2 Hz, and solid curves indicate equivalent circuit fits to two parallel *RQ* sub-circuits in series. The Pt probe utilized is identified as Probe 2 in the Table 4.1.

The Nyquist plots presented in Figure 4.3 and Figure 4.4 reflect data collected from two different Pt probes, where the response for each was examined as a function of the applied voltage. In both cases, the total polarization resistance is a strong function of bias, spanning almost three orders of magnitude in Figure 4.3, from ~ 3 GΩ at –1.2 V to ~ 1 TΩ at –0.6 V. Proton conduction through bulk $CsHSO_4$, typically manifested in bulk conductivity measurements as an ohmic offset at high frequencies,[10] is not visible in Figure 4.3 and Figure 4.4, since its contribution is negligible compared to the electrode processes.

In the absence of a physical model, impedance spectra are commonly analyzed by employing equivalent circuits, for which the simplest building block is a resistor (R) in parallel with a constant phase element (Q). The latter generally represents capacitive effects and has impedance

$$Z_Q = \frac{1}{Y\left(i\omega\right)^n} \tag{4.2}$$

where Y is a constant, ω is the angular frequency, and n ranges from 0 to 1. When $n = 1$, the constant phase element becomes a perfect capacitor with capacitance Y, and the parallel RQ sub-circuit is represented in the Nyquist plot as a semi-circle with its center lying on the real axes. Deviations of n from 1 are typically interpreted in terms of a distribution of relaxation times within a globally measured response.[32, 34]

The impedance spectra shown in Figure 4.3 are comprised of two arcs; the frequency overlap of the two processes varied with experiment and spatial position, with some measurements more clearly depicting the presence of two electrode processes (Figure 4.4). The impedance spectra were fitted to an empirical equivalent circuit model comprised of two parallel RQ circuits in series. Fitting results yielded $n > 0.9$ for both processes, indicating ideal capacitive behavior with a low dispersion in the characteristic frequency of each process. These n values are considerably higher than those observed for macroscale interfacial processes for which depression of the electrode arc in the Nyquist plot reflects n values in the range 0.6–0.8.[36–40] Low n values for interfacial processes are commonly attributed to spatial heterogeneities at the electrode | electrolyte interface.[32, 34] The observation of a low dispersion of relaxation times in the present measurement suggests that, at the nanoscale, averaging effects are eliminated. In turn, because of the low dispersion, it is possible from these measurements to clearly observe two processes, despite the similarity of their relaxation times. In a macroscopic measurement with low n, deconvolution of interfacial processes that are close in characteristic frequencies would likely not be possible.

The bias dependence of the resistances associated with the two processes (Figure 4.5) reveals that the resistance of the low-frequency process, R_{LF}, is strongly dependent on voltage, decreasing from 1 TΩ at –0.6 V to less than 1 GΩ at –1.2 V. In the semi-log plot, an apparent exponential dependence is evident. In contrast, the resistance of the high-frequency process, R_{HF}, is largely independent of bias, displaying an erratic voltage dependence between 1 and 10 GΩ that is almost within the noise of the measurement. The total electrochemical resistance, R_{TOT}, which is simply the sum of R_{LF} and R_{HF}, is accordingly dominated by R_{LF} at low bias and by the fixed value of R_{HF} at high bias. While the data here are presented for one representative set of impedance spectra, such behavior was observed in multiple measurements. An analysis of the capacitances associated with the two processes and their bias dependence is not presented here due to their relatively high fitting errors.

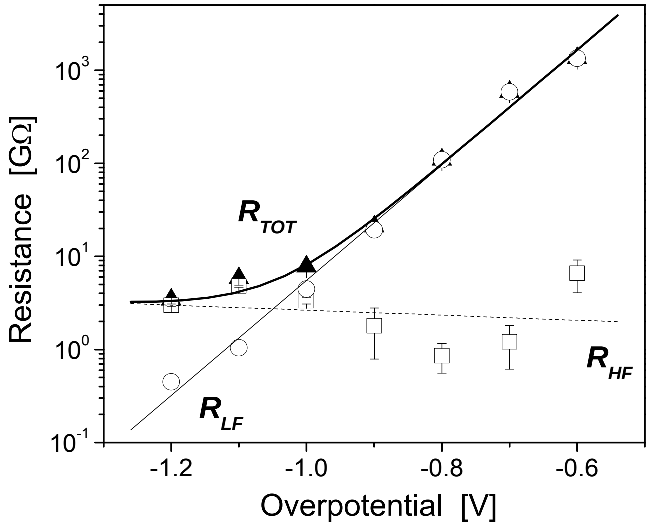

Figure 4.5 Total polarization resistance (R_{TOT}) and electrode resistances (R_{LF}, R_{HF}) determined by fitting AC impedance spectra (shown in Figure 3) to two parallel RQ circuits in series. Lines indicate the general trends of each parameter and were obtained by linear fits of R_{HF} and R_{LF} and their sum, R_{TOT}. Resistance is plotted on a logarithmic scale.

The electrochemical reaction of interest, Equation (4.1), is represented by the cathodic branch of the cyclic voltammogram. Cyclic voltammograms obtained at slow scan rates (such that capacitive and other transient effects are reduced) can be employed for quantitative analysis of oxygen reduction kinetics. For such an analysis, it is essential to recognize that the oxygen reduction reaction occurs on Pt metal only at voltages negative of that for the Pt-PtO$_x$ couple; at all other voltages, $O_2 + 4H^+ + 4e^- \rightleftharpoons 2H_2O$ occurs on platinum *oxide*. An implication of Pt oxide formation is that, for a fuel cell under open-circuit conditions, platinum catalyst at the cathode is oxidized, and the initial current drawn contains a contribution from Pt oxide reduction.

4.3.3 Analysis of Oxygen Electro-reduction Kinetics

The behavior revealed in Figure 4.5 suggests that the DC current across the Pt | CsHSO$_4$ interface should, like the AC resistance, display an exponential dependence on bias within an appropriate range of voltages. In Figure 4.6, we plot, on a semi-log scale, data obtained from the return sweep (implying the oxide has already been reduced to the metal) of the cathodic branch of a cyclic voltammogram collected at a 5 mV s^{-1} scan rate, and, indeed, linearity is observed between –1 and –0.6 V. At higher biases (beyond –1 V), the deviation from linearity in the semi-log plot is readily attributed to the increasing importance of the bias-independent resistance term (Figure 4.5). At smaller biases (less than –0.6 V), the scatter is a result of the overall low current and a non-zero offset current (correction procedures for which are described in the Appendix F.2.3). In principle, the results of Figure 4.5 and Figure 4.6 can be numerically converted from one form to the other, however, the thermal drift in the system (estimated to be ~ 0.1 nm s^{-1} at 150 ºC) precludes quantitative comparisons. Nevertheless, the overall agreement between the AC and DC measurements, in terms of the functional form of the data, demonstrates the robustness of the experimental approach pursued here for examining electrode kinetics. Both measurements methods are utilized, as AC impedance spectroscopy provides invaluable mechanistic information, i.e., the elucidation of multiple processes and their relative timescales, whereas cyclic voltammetry enables quantification of selected kinetic parameters.

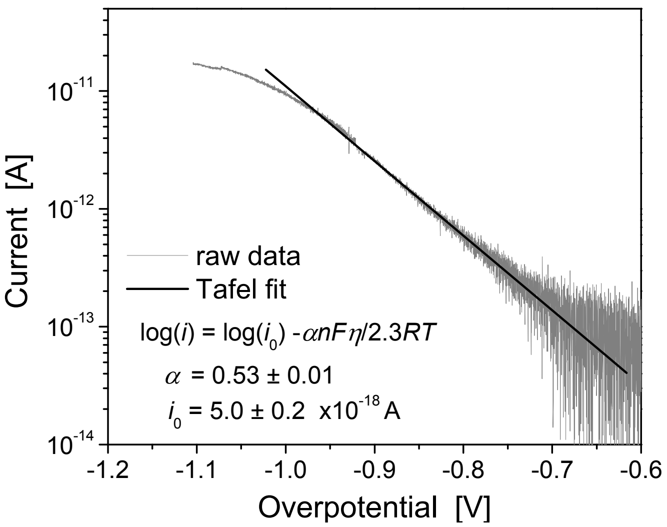

Figure 4.6 Semi-log plot of the cathodic branch of the cyclic voltammogram for Pt | $CsHSO_4$. The voltammogram was collected with a 5 mV s^{-1} scan rate at ~ 150 ºC in humidified air (~ 0.03 atm H_2O). The exchange coefficient and exchange current can be extracted from the slope and intercept, respectively, by fitting the linear regime to the Tafel equation, Equation (4.6). The Pt probe utilized is identified as Probe 3 in Table 4.1.

A voltage-dependent resistance is a typical feature of charge transfer electrochemical reactions, and the exponential dependence of R_{LF} on bias suggests analysis in terms of conventional Butler-Volmer reaction kinetics. In a generic sense, the charge transfer reaction associated with oxygen electro-reduction at the Pt | $CsHSO_4$ interface can be described as[41]

$$\mathrm{O} + \mathrm{e}^- \underset{k_a}{\overset{k_c}{\rightleftharpoons}} \mathrm{R} \tag{4.3}$$

where k_c and k_a are the rate constants for the cathodic and anodic directions, respectively, and a single-electron process has been assumed. The kinetics associated with this reaction can be expressed in terms of the Butler-Volmer equation (derived in Appendix A.1),

$$\frac{i}{i_0} = \exp\left[-\frac{\alpha F}{RT}\eta\right] - \exp\left[\frac{(1-\alpha)F}{RT}\eta\right] \tag{4.4}$$

where i_0 is the exchange current, $\eta = E - E_{eq}$ is the overpotential, α is the exchange coefficient which ranges from 0 to 1, and F, R and T have their usual meanings. At the large negative overpotentials selected for the analysis performed here (due to both Pt oxidation and significant offset current at small overpotentials), only the cathodic branch of the Butler-Volmer equation need be considered. For $\eta << 0$, Equation (4.4) reduces to

$$i = i_0 \exp\left(-\frac{\alpha F}{RT}\eta\right) \tag{4.5}$$

or, in Tafel form,

$$\log(i) = \log(i_0) - \frac{\alpha F}{2.3RT}\eta \tag{4.6}$$

Thus, from a linear fit to the semi-log data, one obtains the exchange current density (from the extrapolated intercept at zero bias or overpotential) and the exchange coefficient (from the slope). As an alternative to Equation (4.6), one can consider introduction of a term that accounts for the observation of an additional, bias-independent process (effectively accounting for R_{HF}). Attempts to fit an appropriately modified expression, however, were largely unsuccessful because of the insensitivity of the fit parameters, and hence the determination of properties associated with the high-frequency process from the voltammograms was not pursued.

For the specific data set presented in Figure 4.6 and a fit over the potential range from –0.65 to –1.0 V, we obtain $\alpha = 0.53 \pm 0.01$ and $i_0 = 5.0 \pm 0.2 \times 10^{-18}$ A. Because the area of electrochemical activity at the probe tip is unknown, the value determined for the exchange current cannot be readily interpreted quantitatively or compared to literature measurements. The exchange coefficient, in contrast, is independent of these uncertainties and its absolute value has significance. This parameter provides a measure of the asymmetry of the activation barrier for the charge transfer. For a single-electron process, α should lie between 0 and 1, with $\alpha = 0.5$ corresponding to perfect symmetry of the anodic and cathodic directions of the charge transfer step. A value of 0.53 as obtained here falls within the range typically observed in aqueous electrolyte systems ($\alpha = 0.3$–0.7).[41]

4.3.4 Heterogeneity of Electrochemical Kinetics

As already noted, conducting atomic force microscopy enables an exploration of the spatial variation of electrode kinetics at Pt | $CsHSO_4$ with relative ease. A scanning electron micrograph (Figure 4.7a) shows typical surface features of polycrystalline $CsHSO_4$ after testing. Alongside it is an AFM topography scan of a 5×5 μm^2 region, collected under operating conditions, that includes (nominal) spatial positions at which electrochemical measurements were acquired (Figure 4.7b). The electron micrograph shows large crystalline grains, 5–10 μm in size, whereas the topography scan, collected at higher resolution, reveals finer features (< 1 μm) and a RMS roughness of ~ 30 nm. Cyclic voltammograms measured at each position were stable upon cycling and, within a moderate range (Appendix F.2), insensitive to the value of the applied force, and therefore the data are considered reliable for evaluating the electrochemical response at each position. However, the extent of thermal drift after measuring several positions precludes a precise correlation of electrochemical reaction rates with surface features.

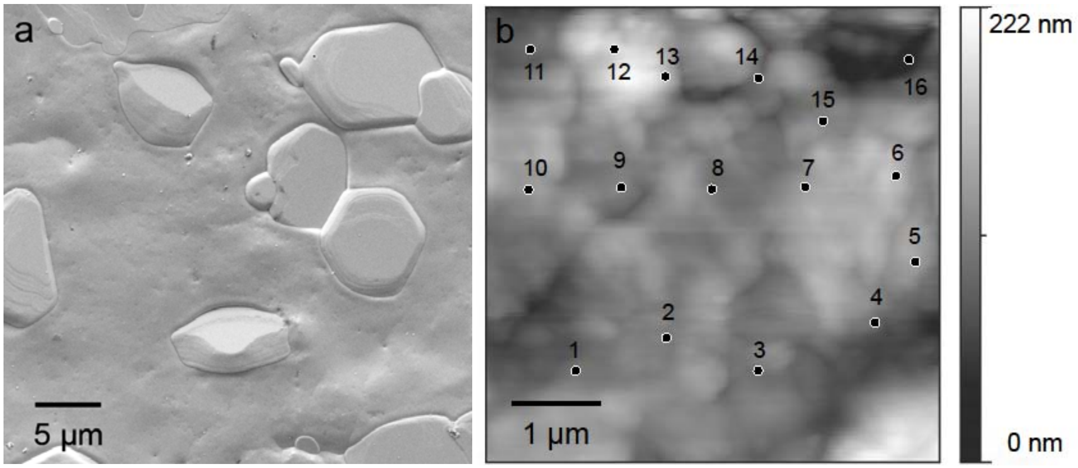

Figure 4.7 (a) Scanning electron micrograph of a typical $CsHSO_4$ surface acquired after electrochemical testing. (b) Topography scan of the polycrystalline $CsHSO_4$ surface collected at ~ 150 ºC in humidified air (~ 0.03 atm H_2O). Labels denote nominal positions at which electrochemical measurements were acquired (Figure 4.8).

The voltammograms obtained at 16 different points across the electrolyte surface (Figure 4.8a) exhibited features similar to that in Figure 4.6. Specifically, for each voltammogram, a plot of log(i) as function of bias revealed a linear regime at low bias followed by a decrease in the slope at high bias. Furthermore, impedance spectra collected at –1.0 and –0.9 V for select positions (not shown) were qualitatively similar to one another and to the results in Figure 4.4, indicating, in all cases, a high-frequency process with a (largely) bias-independent resistance and a low-frequency process with a resistance that decreased sharply with bias. Thus, one can conclude that the mechanistic steps involved in oxygen electro-reduction at the Pt | $CsHSO_4$ interface are maintained across the electrolyte surface.

While the general shape of the voltammograms and impedance spectra were reproduced at different locations, the specific values differed substantially. For example, in the voltammetry experiments, at –0.95 V, the measured current ranged between –1.5 and –4.5 pA, a three-fold variation. This variation is, in turn, manifested as notable variations of the exchange coefficient and exchange current across the electrolyte surface, as extracted from a Tafel analysis of the linear regime of each voltammogram, typically occurring at overpotentials between –1.0 and –0.6 V. For the specific surface shown in Figure 4.7b, α ranges from 0.22 to 0.39 and i_0 from 0.2 to 6 fA (Figure 4.8b), with the two parameters apparently counter-correlated (i.e., i_0 decreases as α increases). Rather remarkably, a summary of the data for measurements of six different Pt | $CsHSO_4$ interfaces (Figure 4.9) reveals a counter-correlation between α and i_0 that extends over several orders of magnitude in i_0 and a factor of six in α. Specifically, across the six experiments, α spans from 0.1 to 0.6, with an average value of 0.3 ± 0.1, and i_0 correspondingly spans from 5×10^{-14} to 5×10^{-19} A. The spatially-averaged exchange coefficient of 0.3 falls in the range, 0.35 ± 0.05, measured for the Pt-wire | CsH_2PO_4 system at ~ 240 ºC in humidified O_2 with ~ 0.35 atm H_2O (unpublished data). For Pt-wire | CsH_2PO_4, the working electrode was a 250 μm diameter Pt wire embedded in CsH_2PO_4, and thus, the exchange coefficient from such a geometry can be treated as representative of an area-averaged electrochemical response.

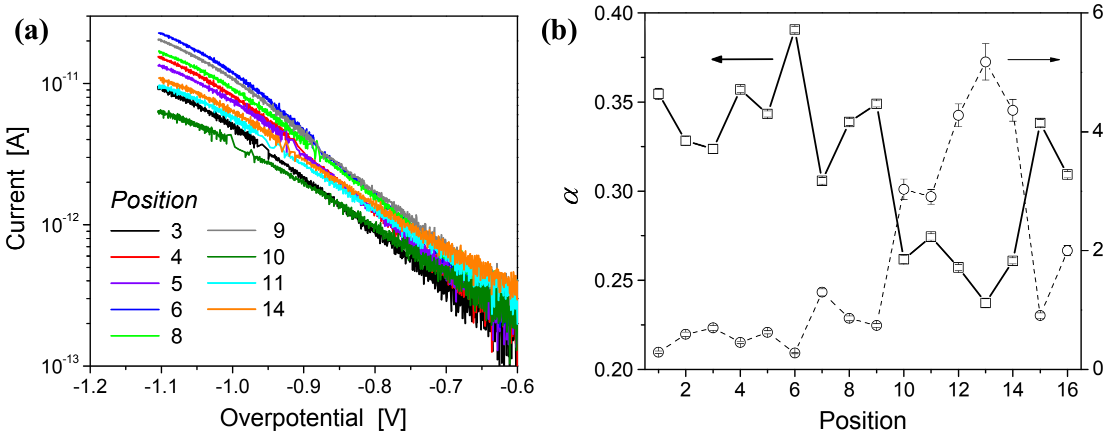

Figure 4.8 (a) Semi-log plot of cyclic voltammograms (cathodic branch) for Pt | $CsHSO_4$ at select points across the surface shown in Figure 4.7b. Data were acquired with a 25 mV s^{-1} scan rate at ~ 150 ºC in humidified air with ~ 0.03 atm H_2O (using Probe 1, Table 4.1). (b) Exchange coefficient, α, and exchange current, i_0, plotted as functions of position. Parameters were extracted from fitting the linear regime of each curve in (a) to the Tafel equation (Equation (4.6)). In some instances, the error bars for α are smaller than the data markers.

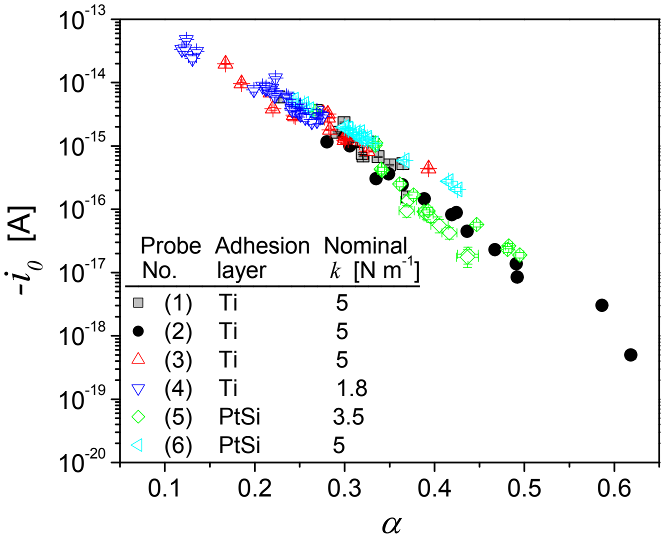

Figure 4.9 Semi-log plot of i_0 as a function of α, showing a linear relationship across six different data sets, with the probe type indicated in the legend. Data were collected at ~ 150 ºC in humidified air (0.01–0.03 atm H_2O). In some instances, the error bars for i_0 and α are smaller than the data markers.

Ignoring for the moment the counter-correlation between α and i_0, the simple observation that these parameters vary so substantially with position demonstrates that electrochemical reaction rates at Pt | $CsHSO_4$ are indeed highly influenced by nanoscale surface features of the polycrystalline electrolyte. Because variations in applied force produced no detectable change in the features of the voltammograms (see Appendix Figure F.11a), changes in the extent of electrochemical reaction area are unlikely to be responsible for the large variations in i_0 or α. The relevant surface features may include the crystallographic orientation of the surface termination and the occurrence of grain or domain boundaries, or even dislocations with surface termination. Any of these features may influence the residual surface charge and be a means of influencing electrochemical reaction rates. As stated at the outset, because the electrochemical reactions in solid electrolyte fuel cells involve surface reaction steps, nanoscale heterogeneity is to be expected. The clear counter-correlation between α and i_0, however, is unexpected. The observation of a common correlation between α and i_0 for six different Pt | $CsHSO_4$ interfaces, furthermore, leaves little doubt that the phenomenon is real and suggests a common mechanism for these different interfaces. Within the Butler-Volmer framework, a large value of i_0 corresponds to a small reaction barrier between oxidized and reduced states, Equation (4.3), under equilibrium conditions. A small value of α, which occurs for those reactions sites with large i_0, corresponds to a minimal decrease in the activation barrier under bias. The counter-correlation thus reflects a physical situation in which reaction pathways with small barriers under equilibrium conditions are relatively unaffected by the applied bias, whereas those with high barriers under equilibrium conditions are strongly decreased under bias. While there is no fundamental basis for expecting such a result, *a priori*, the counter-correlation creates a situation in which, under a given bias, all reaction sites attain a comparable level of electrochemical activity, as reflected in the value of the current (under bias) rather than the exchange current (under zero bias). A direct correlation between α and i_0, in contrast, would imply that sites with low barriers under open-circuit conditions become even more active relative to other sites, under bias, and hence an immediate divergence in activity. An extensive search of the relevant literature did not uncover any studies showing such a wide-ranging, systematic and correlated variation of α and i_0 within a given electrochemical system, although, in some instances, variations as a function of a third parameter (e.g., temperature, electrode/electrolyte composition, or electrode particle size)[97–104] have been explored. Further study to explicitly identify the surface features that influence electrochemical reaction kinetics at the Pt | $CsHSO_4$ interface and electrolyte-metal-gas boundaries in general is under way.

4.4 Summary

We demonstrate the use of conducting atomic force microscopy as a tool to quantitatively probe oxygen reduction kinetics in controlled environments and at elevated temperatures. We employ AC impedance spectroscopy to gain insight into the mechanism of electrocatalysis and cyclic voltammograms for quantitative analysis of oxygen reduction kinetics in the Pt | $CsHSO_4$ system. The oxygen reduction reaction is limited primarily by an overpotential-activated process that exists at low frequencies, with an additional impedance contribution, at high overpotentials, from a process that is weakly overpotential-dependent. Our ability to deconvolute these two processes derives, we believe, from the nanoscale measurements. At this scale, the measurements are free of averaging effects, leading to near-ideal capacitive behavior and minimal dispersion in the frequency response. The overpotential-activated step was interpreted as charge transfer and evaluated using the Butler-Volmer equation. Within the Butler-Volmer framework, a spatial variation in kinetics, represented by the exchange coefficient and exchange current, was observed across six independent measurements. That the correlation between $\log(i_0)$ and α for all six experiments collapses into a single line demonstrates the robustness of our experimental approach.

Chapter 5 Phase Transformation Hysteresis in Solid Acid Compounds

Adapted with permission from: Louie, M. W.; Kislitsyn, M.; Bhattacharya, K.; Haile, S. M. Phase Transformation and Hysteresis Behavior in $Cs_{1-x}Rb_xH_2PO_4$. *Solid State Ionics* **2010**, *181,* 173–179.

Abstract

A new theory on the origin of hysteresis in first order phase transformations was evaluated for its applicability to the phase transformation behavior in the $Cs_{1-x}Rb_xH_2PO_4$ solid solution system. Specifically, the correlation between λ_2, the middle eigenvalue of the transformation matrix describing the cubic-to-monoclinic superprotonic transition, and the transformation hysteresis was examined. The value of λ_2 was estimated from a combination of variable temperature diffraction data and thermal expansion measurements obtained for select compositions in the solid solution system. The transformation hysteresis was determined for $Cs_{1-x}Rb_xH_2PO_4$ compositions (x = 0, 0.25, 0.50, and 0.75) by single-frequency impedance measurements. It was found that the transition temperature increases monotonically with increasing Rb content, from 227.6 ± 0.4 ºC for the end-member CsH_2PO_4 to 256.1 ± 0.3 ºC for $Cs_{0.25}Rb_{0.75}H_2PO_4$, as does the hysteresis in the phase transition, from 13.4 ºC to 17.4 ºC. The computed values of λ_2 were far from 1, ranging from 0.932 (for $x = 0$) to 0.919 (for $x = 0.5$). The observation of λ_2 decreasing with Rb content is consistent with the theoretical expectations.

We furthermore examined the phase transformation characteristics of CsH_2PO_4 and $CsHSO_4$, and assessed the correlation between microstructure and the phase transformation hysteresis. $CsHSO_4$ was found to undergo phase transformation with significantly fewer cracks compared to CsH_2PO_4, consistent with its lower transformation hysteresis of ~ 5 ºC. Domain patterns were observed on the surface of $CsHSO_4$ single crystals after thermal cycling through the phase transition. However, domain patterns were not readily visible in single crystals of CsH_2PO_4.

5.1 Introduction

Many solid acid compounds undergo a solid-to-solid phase transition, typically from a monoclinic phase to a cubic, tetragonal, or trigonal phase on heating. Discontinuous changes in the lattice parameters (or volume) and enthalpy, etc. across the transition have been observed for many solid acid compounds,[9, 11, 22, 105–108] and, moreover, solid acid compounds, particularly $Rb_3H(SeO_4)_2$, have been observed to form domain patterns upon heating from the room temperature phase.[109] In this chapter, we evaluate the applicability and utility of a newly introduced theory of martensitic phase transformations[110, 111] to solid acid compounds. This theory predicts hysteresis behavior (and microstructure) solely from arguments of crystal symmetry and geometric compatibility between the high- and low-temperature phases. Specifically, the criterion for zero hysteresis is the direct compatibility between the two phases, mathematically described by the condition, $\lambda_2 = 1$, where λ_2 is the middle eigenvalue of a transformation matrix that maps the transformation of the high-temperature, high-symmetry phase to the low-temperature, low-symmetry phase. A clear relationship between the measured hysteresis and the middle eigenvalue has been demonstrated for the shape-memory alloy system, Ni-Ti-Cu,[110] enabling the identification of a low-hysteresis alloy with unprecedented durability in thermal cycling.[112]

Solid acid compounds are ideal for evaluating the broader applicability of the theory of martensitic transformations. Many solid acid compounds can be chemically modified as a way to tune the lattice parameters for compatibility. For example, the compounds $Rb_2(HSO_4)(H_2PO_4)$, $(NH_4)_2(HSO_4)(H_2PO_4)$, $K_2(HSO_4)(H_2PO_4)$ are all isostructural with $Cs_2(HSO_4)(H_2PO_4)$ which has been shown to undergo a monoclinic-to-cubic transition at ~ 91 ºC and a reverse transition on cooling at temperatures as low as ~ 30 ºC.[9] The possibility of forming solid solutions renders solid acids a useful class of materials with which to further explore the principles of crystallographic compatibility.

In turn, the investigation of the phase transformation behavior of solid acid compounds can shed light on the effect of hysteresis on the robustness of solid acid compounds as electrolytes in electrochemical devices. A consequence of crystallographic incompatibility between the high- and low-temperature phases is the formation of strain energy during phase transformation, released in the form of cracks. As evident in Chapter 3, the formation of microcracks in CsH_2PO_4 prevents the fabrication of well-defined and well-controlled electrode | electrolyte interfaces and active sites. Not only this, the existence of cracks in the electrolyte membrane may have implications for fuel cell operation, as shown in Figure 2.15. Although cracks which form on heating though the transition heal under fuel cell operating conditions, it is unclear how robust such a system is for long-term operation and repeated on-off (temperature) cycling.

In this chapter, we gain an understanding of reversibility of the superprotonic phase transition in solid acid compounds and its implications for using solid acids as electrolytes for electrochemical applications. As CsH_2PO_4 is presently the electrolyte of choice for solid acid fuel cells, we have chosen to investigate the phase transformation behavior of $Cs_{1-x}Rb_xH_2PO_4$ and its correlation to the compatibility condition, $\lambda_2 = 1$. $Cs_{1-x}Rb_xH_2PO_4$ has been shown to crystallize into the $P2_1/m$ structure of the end-member CsH_2PO_4 for x up to ~ 0.8.[113, 114] All of the crystal chemical parameters (cell volume, lattice parameters, hydrogen bond length, etc.) vary gradually and monotonically with an increase in Rb content. Furthermore, a superprotonic phase transition has been shown to occur for these compounds at temperatures between ~ 220 ºC and ~ 250 ºC. Combined, the high solubility of Rb into CsH_2PO_4 and the ease with which transition behavior can be evaluated via proton conductivity measurement renders $Cs_{1-x}Rb_xH_2PO_4$ an attractive system for exploration. Because incorporation of Rb into CsH_2PO_4 does not detrimentally lower the proton conductivity,[113] $Cs_{1-x}Rb_xH_2PO_4$ compounds may also prove to be useful as electrolytes, particularly if such materials exhibit greater phase transition reversibility.

We furthermore explore the widespread applicability of the compatibility condition by comparing the phase transformation characteristics of $CsHSO_4$ and CsH_2PO_4. We examine the physical characteristics of these two solid acid compounds, specifically the effect of the superprotonic phase transition on crack density and microstructure. With hysteresis and microstructure studies, combined, we evaluate the applicability of the theory of crystallographic compatibility to the superprotonic phase transition and discuss the implications of these studies on the rational design of solid acid electrolytes with minimal hysteresis and strain energy during transformation.

5.2 Theory of Crystallographic Compatibility

Martensitic transformations are diffusionless, solid-to-solid transitions between phases of different crystalline structures. It has recently been proposed and demonstrated that the structural relationship between the two phases establishes not only the microstructural patterns that emerge upon cooling from the high-temperature austenite phase to the low-temperature martensite phase[115] but also the degree of hysteresis associated with the transition.[110, 111] Here, we present the mathematical framework for the theory of crystallographic compatibility, specifically for the $Cs_{1-x}Rb_xH_2PO_4$ system which undergoes a monoclinic-to-cubic transformation.

To evaluate the geometric compatibility of the two crystalline phases, we examine the crystallographic relationship between the high-temperature superprotonic and low-temperature paraelectric phases of CsH_2PO_4 (Figure 5.1). The superprotonic (austenite) phase adopts the CsCl structure type, with Cs atoms arranged at the corners of a simple cubic unit cell and an orientationally disordered polyanion group located at the cell center, whereas the paraelectric (martensite) phase is monoclinic and the $(H_2PO_4)^-$ groups reside in fixed orientations. Shown in Figure 5.1 is just one way in which the paraelectric phase can emerge from the superprotonic phase upon cooling through the transition. Due to the relative symmetries of the two phases, there are exactly twelve ways in which the cubic phase can be transformed to the monoclinic phase. In general, the number of ways the transformation can occur, that is, the number variants (N) is

$$N = \frac{\#\, rotations\ in\ P_a}{\#\, rotations\ in\ P_m} \tag{5.1}$$

where P_a and P_m are the point groups of the austenite and martensite phases, respectively. In the case of CsH_2PO_4, $N = 24/2 = 12$.

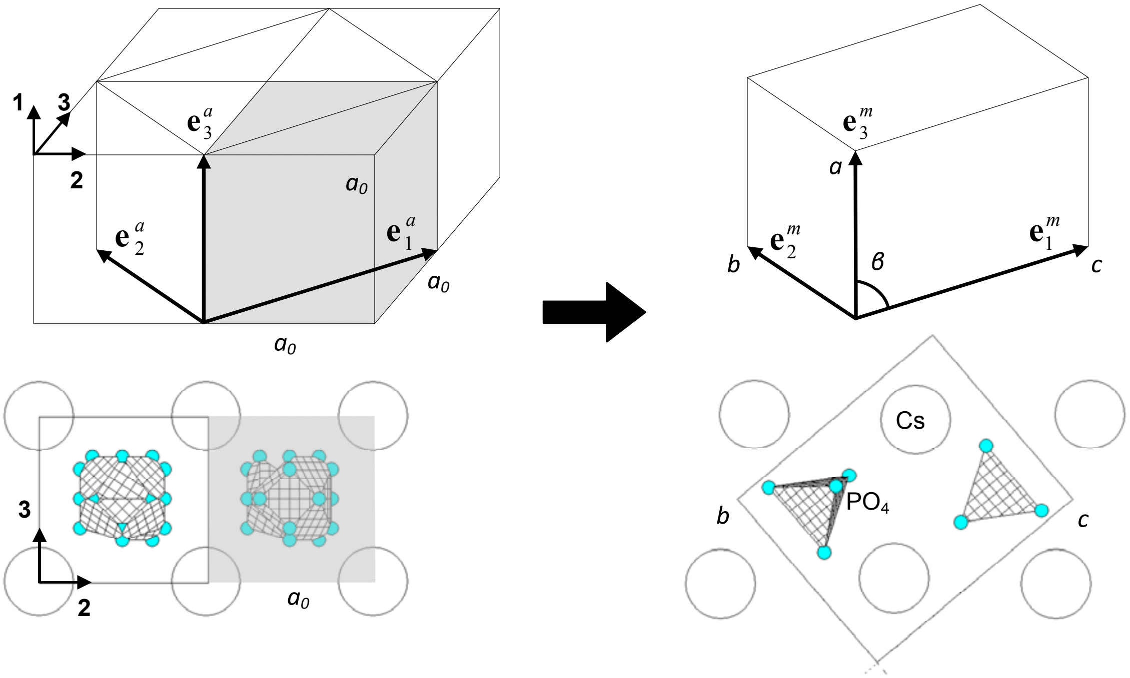

Figure 5.1 Schematic of one of twelve ways the high-temperature cubic phase can transform to the low-temperature monoclinic phase: the relationship between the lattices (top) and with atomic sites for CsH_2PO_4 (bottom). In the high-temperature phase (left), the PO_4 groups are orientationally disordered, taking on one of six possible orientations, whereas in the low-temperature phase (right), the PO_4 groups reside in fixed orientations. (Hydrogen atoms are not shown.)

The mapping of the lattice of the austenite to that of the martensite can be described by the homogeneous deformation matrix, $\mathbf{U_j}$, defined by

$$\mathbf{e_i^m} = \mathbf{U_j e_i^a} \tag{5.2}$$

where the subscript j refers to the twelve possible martensite variants. (By convention, $\mathbf{U_j}$ is chosen to be symmetric. The procedure for satisfying this criterion is detailed in Appendix I.) For CsH_2PO_4, the lattice vectors of the austenite, $\mathbf{e_i^a}$, are chosen to be the edges of a tetragonal unit cell constructed from the contents of two cubic unit cells. Those of the martensite, $\mathbf{e_i^m}$, are taken to correspond directly to the monoclinic unit cell. Using an orthonormal basis parallel to the cubic unit cell, we obtain for the specific variant indicated by Figure 5.1,

$$\mathbf{e}_1^a = a_0\begin{pmatrix}0\\1\\1\end{pmatrix} \qquad \mathbf{e}_2^a = a_0\begin{pmatrix}0\\-1\\1\end{pmatrix} \qquad \mathbf{e}_3^a = a_0\begin{pmatrix}1\\0\\0\end{pmatrix} \tag{5.3}$$

$$\mathbf{e}_1^m = \frac{c}{\sqrt{2}}\begin{pmatrix}\sqrt{2}\cos\beta\\ \sin\beta\\ \sin\beta\end{pmatrix} \qquad \mathbf{e}_2^m = \frac{b}{\sqrt{2}}\begin{pmatrix}0\\-1\\1\end{pmatrix} \qquad \mathbf{e}_3^m = a\begin{pmatrix}1\\0\\0\end{pmatrix} \tag{5.4}$$

The deformation matrix, $\mathbf{U_1}$, then becomes

$$\mathbf{U_1} = \begin{pmatrix}\gamma & \varepsilon & \varepsilon\\ \varepsilon & \alpha & \delta\\ \varepsilon & \delta & \alpha\end{pmatrix} \tag{5.5}$$

where

$$\gamma = \frac{a(\sqrt{2}a + c\sin\beta)}{a_0\sqrt{2a^2 + c^2 + 2\sqrt{2}ac\sin\beta}} \tag{5.6}$$

$$\varepsilon = \frac{1}{\sqrt{2}a_0}\left(\frac{ac\cos\beta}{\sqrt{2a^2 + c^2 + 2\sqrt{2}ac\sin\beta}}\right) \tag{5.7}$$

$$\alpha = \frac{1}{2\sqrt{2}a_0}\left(\frac{c(c + \sqrt{2}a\sin\beta)}{\sqrt{2a^2 + c^2 + 2\sqrt{2}ac\sin\beta}} + b\right) \tag{5.8}$$

$$\delta = \frac{1}{2\sqrt{2}a_0}\left(\frac{c(c + \sqrt{2}a\sin\beta)}{\sqrt{2a^2 + c^2 + 2\sqrt{2}ac\sin\beta}} - b\right) \tag{5.9}$$

Once $\mathbf{U_1}$ is known, the other variants can be obtained by applying the rotations of the cubic austenite lattice to this matrix. Variants, $\mathbf{U_1}$, $\mathbf{U_2}$, …, $\mathbf{U_N}$ have the form

$$\mathbf{U_j} = \mathbf{R}^{\mathrm{T}}\mathbf{U_1}\mathbf{R} \tag{5.10}$$

where **R** is a rotation in the point group of the austenite. All twelve variants are shown in Table I.3. Because these twelve variants are related by symmetry, they are energetically equivalent, with equal likelihood of forming on cooling from the austenite phase. Furthermore, they all share the same eigenvalues, λ_1, λ_2, λ_3, where $\lambda_1 < \lambda_2 < \lambda_3$ are the ordered eigenvalues of $\mathbf{U_j}$. The condition for the middle eigenvalue, $\lambda_2 = 1$, implies compatibility between a single variant of martensite and the austenite. In this case, the two phases coexist during transformation by the formation of a perfect, strain-free interface, and the transformation is expected to be reversible. However, the more frequently observed scenario is one in which $\lambda_2 \neq 1$. In this case, the low-temperature phase is not compatible with the high-temperature phase, and the material transforms on cooling by adopting multiple variants of the low-temperature phase (i.e., twinning) in an attempt to minimize strain at the interface. The observed transformation hysteresis is attributed to additional driving force required on cooling in order for the material to transform by way of this incompatible interface. Additionally, by similar compatibility arguments, the microstructure of the martensite, namely geometrically compatible variant pairs can be identified, and their orientations with respect to one another and with the austenite phase can be predicted. The procedure for determining the possible variant pairs and austenite-martensite interfaces is presented in Appendix I.

5.3 Experimental

5.3.1 Synthesis and Fabrication

The end-member compounds CsH_2PO_4 and RbH_2PO_4 were individually prepared from aqueous solutions of Cs_2CO_3 (99.9%, Alfa Aesar, 12887) and Rb_2CO_3 (99.9%, Alfa Aesar, 12893), respectively, and H_3PO_4 (85%, Mallinckrodt, 2796). These aqueous solutions were introduced into methanol to induce rapid precipitation, and the resulting precipitates dried at ~ 100 ºC. Materials in the solid solution series, $Cs_{1-x}Rb_xH_2PO_4$, were synthesized by dissolving CsH_2PO_4 and RbH_2PO_4 powders in water in the desired molar ratios corresponding to $x = 0.25, 0.50, 0.75$ and then injecting the mixed aqueous solution into a sonicated methanol bath. The resulting precipitates were dried at ~ 100 ºC to remove surface water and methanol. Polycrystalline discs ~ 9.3 mm diameter, ~ 0.7 mm thick and > 93% of theoretical density, were prepared for conductivity measurements by uni-axially pressing at ~ 491 MPa for 20 min. Colloidal silver paint (Ted Pella, 16032) was applied to both sides of the dense compacts for electrical contact.

Single crystals of CsH_2PO_4 and $CsHSO_4$ were grown from their respective aqueous solutions. (The synthesis of CsH_2PO_4 and $CsHSO_4$ powders is detailed in Chapters 3 and 4, respectively.) Solutions were filtered through a 0.2 μm syringe filter to remove dust particles and then placed at ambient conditions, partially covered, to allow for water evaporation and crystal growth. As-grown crystals were pulled directly out of solution and rinsed quickly with water; for imaging studies presented in this chapter, these crystals were denoted "as-grown". In some cases, crystals were polished with fine 2 μm grit size sandpaper before use, while others were fractured using a sharp razor blade. Polished crystals were sanded uni-directionally so that the resulting streaks could be easily distinguished from any microstructural changes that appeared due to heating.

5.3.2 Characterization

Synthesized $Cs_{1-x}Rb_xH_2PO_4$ powders were characterized with a Phillips X'Pert Pro powder X-ray diffractometer (XRD) using Cu Kα radiation (45 kV, 40mA) with a 2θ range of 5–70° and a step size and dwell time of 0.017° and 50 s, respectively. Variable temperature diffraction data were collected for CsH_2PO_4 using an Anton Parr HTK1200 furnace at temperatures up to ~ 256 ºC, well above the superprotonic phase transition temperature. Lattice parameters were obtained by Rietveld refinement (Phillips X'Pert Plus software) with initial references structures for the monoclinic[116] and cubic[117] phases respectively. Chemical compositions were verified by an Oxford INCA 300 X-ray energy dispersive spectrometer (EDS) utilized in conjunction with a scanning electron microscope (LEO 1550 VP) at an accelerating voltage of 10 kV.

Phase transformation behavior was studied by single frequency AC impedance measurements at 10 kHz and with a perturbation of 50 mV (HP 4284 precision LCR meter). While a full range of frequencies is desirable for determining sample conductivity via equivalent circuit fitting, transformation behavior is more appropriately captured by rapid, single-frequency measurements. The frequency of 10 kHz was selected on the basis of preliminary measurements of complete impedance spectra which demonstrated this value to accurately reflect bulk transition characteristics. The samples were placed in a tube furnace and sandwiched between two sheets of Toray carbon paper which, in turn, was mechanically contacted to silver mesh connected to silver wires. In order to mitigate potential dehydration effects[15], measurements were made under high water partial pressure (≥ 0.5 atm), achieved by bubbling inlet N_2 (~ 2.5 mL min^{-1}) through a water bath held at temperatures of 82–95 ºC. The temperature was measured with a thermocouple located ~ 3 mm from the sample. The majority of the measurements were carried out at a heating rate of 1 ºC min^{-1}, with data recorded at 5 s intervals. The reproducibility of the transition behavior was established by collecting data upon repeated temperature cycling. From the impedance data, the transition temperatures were defined as the onset of a change in conductance, determined from the intersection of lines fitted to the linear regions of the conductivity curves.

To evaluate the influence of the phase transition on the microstructure of solid acid compounds, single crystals of CsH_2PO_4 and $CsHSO_4$ were heated to temperatures above the superprotonic phase transition temperature, specifically to 235 ºC under flowing synthetic air with ~ 0.35 atm H_2O for CsH_2PO_4 and to 155 ºC in ambient air for $CsHSO_4$. Macroscale images of entire single crystals were taken using a digital camera in conjunction with a Nikon optical microscope. Additional examination of the microstructure before and after heat treatment were carried out using scanning electron microscopy (LEO 1550VP, Carl Ziess SMT) with a 3 kV accelerating voltage. For $CsHSO_4$, topographical imaging, in situ at superprotonic conditions, was carried out using a PicoSPM atomic force microscope (Series 4500, Agilent Technologies) operated in contact mode. The microscope was equipped with a hotstage heated to temperatures between room temperature and 160 ºC. A thermocouple was attached to the top surface of the crystal by Kapton tape to monitor the temperature of the crystal surface.

5.3.3 Determination of Eigenvalues

Using the expressions developed in Section 5.2, the eigenvalues for the transformation matrix were computed using the software Mathematica (Wolfram Research). Essential to such a computation is knowledge of the lattice parameters just above and below the transformation. Variable temperature diffraction data for CsH_2PO_4 to temperatures as high as 256 ºC was obtained (see Section *5.4.1*). Dehydration effects in the Rb-containing samples (in the dry atmosphere of the XRD hot stage) made direct measurements of the high-temperature cell constants for these compositions challenging, particularly for compounds with high Rb content. Lattice parameters for $Cs_{1-x}Rb_xH_2PO_4$ for $x = 0.25$ and 0.50 were taken from the work of Kislitsyn.[19] In this referenced work, the lattice parameters for $Cs_{0.75}Rb_{0.25}H_2PO_4$ across the phase transition were determined by high-temperature diffraction. However, the dehydration of compounds with higher Rb content was too severe for diffraction measurements of the high-temperature cubic phase. In the case of $Cs_{0.5}Rb_{0.5}H_2PO_4$, it was possible to collect diffraction data at temperatures up to the phase transition before dehydration took over; by estimating the phase transition volume change via dilatometry, the lattice parameters of the cubic phase could be estimated.

5.4 Results and Discussion: $Cs_{1-x}Rb_xH_2PO_4$

5.4.1 Phase and Chemical Characterization

The X-ray diffraction patterns for compounds synthesized with nominal Rb compositions of $x = 0$, 0.25, 0.50, and 0.75 (Figure 5.2) indicate the formation of single phase monoclinic structures with clear shifts in peak positions with increasing Rb content, consistent with the formation of a solid solution. Room temperature lattice parameters, Table 5.1, are comparable to previously reported values in this system, and the measured Rb contents, also reported in Table 5.1, confirm, within error, that the desired stoichiometry has been obtained.

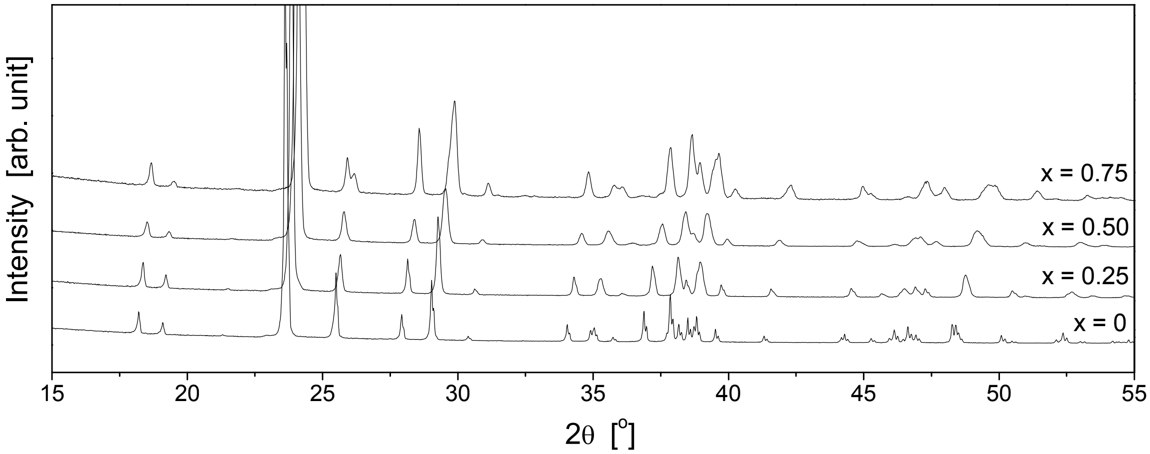

Figure 5.2 Powder X-ray diffraction patterns of $Cs_{1-x}Rb_xH_2PO_4$ at room temperature for nominal compositions x = 0, 0.25, 0.50, and 0.75. Patterns indicate the formation of single phase monoclinic structures with shifts in peak positions upon Rb incorporation.

Table 5.1 Lattice parameters and chemical compositions for the $Cs_{1-x}Rb_xH_2PO_4$ solid solution series. Compositions determined by EDS are averages of at least ten measurements on powder samples.

mol % Rb nominal	**mol % Rb (EDS)**	***a*** **[Å]**	***b*** **[Å]**	***c*** **[Å]**	***β*** **[°]**
0	Not detected	4.8768(2)	6.3867(3)	7.9057(3)	107.705(2)
25	23 ± 2	4.8538(3)	6.3363(3)	7.8416(4)	107.865(3)
50	48 ± 5	4.8414(3)	6.3002(3)	7.7940(7)	108.126(6)
75	74 ± 5	4.8035(6)	6.2561(7)	7.736(1)	108.527(5)

High-temperature diffraction data and thermal expansion behavior of CsH_2PO_4 are shown in Figure 5.3 and Figure 5.4, respectively. The lattice expansion on heating is clearly evident from the shift in the diffraction peaks, as is the transition to a cubic phase by a temperature of 231.5 ºC. Rietveld analysis indicates a high-temperature cubic structure with $a_0 = 4.9653(1)$ Å at 243.5 ºC (where the number in parentheses indicates the uncertainty in the final digit), similar to previously reported values of the cell constant ranging from 4.9549(4) to 4.961(3) Å at temperatures between 237 and 242 ºC.[117–119] The volume change at the transition is found here to be 1.7%, which is measurably larger than that in $CsHSO_4$, 0.54%.[56] In contrast, the volumetric thermal expansion coefficient of the paraelectric phase of CsH_2PO_4, $1.12(3) \times 10^{-4}$ K^{-1}, is comparable to the values of 1.62(3) and $1.76(2) \times 10^{-4}$ K^{-1} for phase III and II, respectively, of $CsHSO_4$.[56] The expansion coefficient of the superprotonic phase of CsH_2PO_4, estimated from just three data points, is $1.98(2) \times 10^{-4}$ K^{-1}, again similar to that reported for superprotonic $CsHSO_4$, $2.66(6) \times 10^{-4}$ K^{-1}. The complete thermal expansion behavior of CsH_2PO_4 is summarized in Table 5.2. It is apparent (Figure 5.4 and Table 5.2) that the effect of temperature on the *a* and *c* parameters of the monoclinic phase is small compared to that on *b*.

While the structures of the superprotonic phases of $Cs_{1-x}Rb_xH_2PO_4$ for $x = 0.50$ and 0.75 have not been explicitly determined, based on the similarity to CsH_2PO_4 and $Cs_{0.75}Rb_{0.25}H_2PO_4$, and based on the widespread occurrence of the cubic CsCl structure type in superprotonic phases with a cation:polyanion ratio of 1:1,[2, 5, 22] we assume for this study that all Rb-substituted superprotonic phases are isostructural to that of superprotonic CsH_2PO_4.

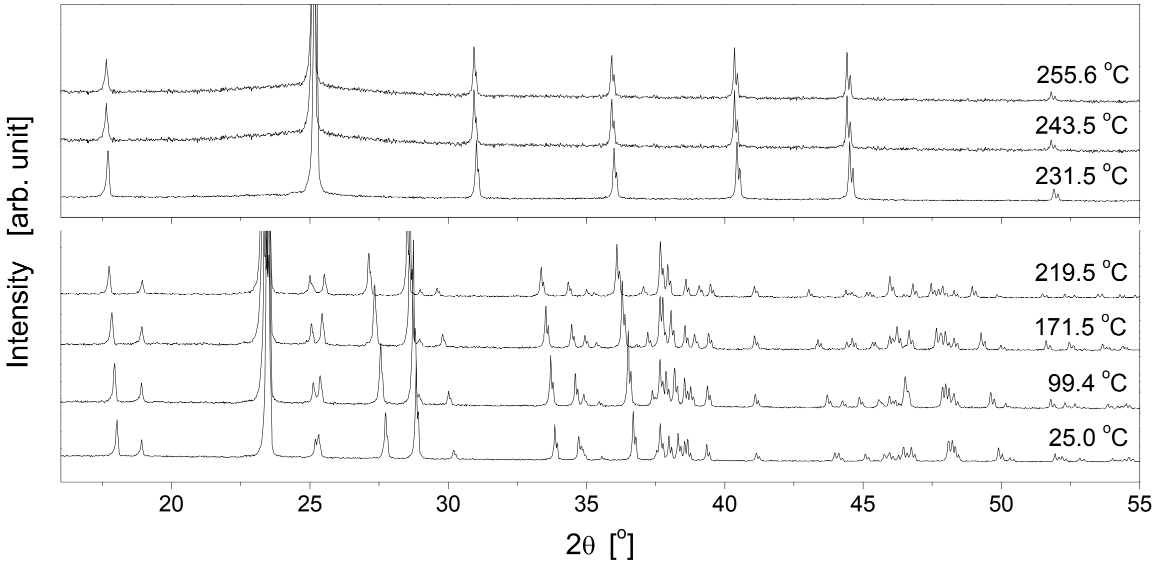

Figure 5.3 Powder XRD patterns for CsH_2PO_4 as a function of temperature for the low-temperature monoclinic phase (bottom) and the high-temperature cubic phase (top).

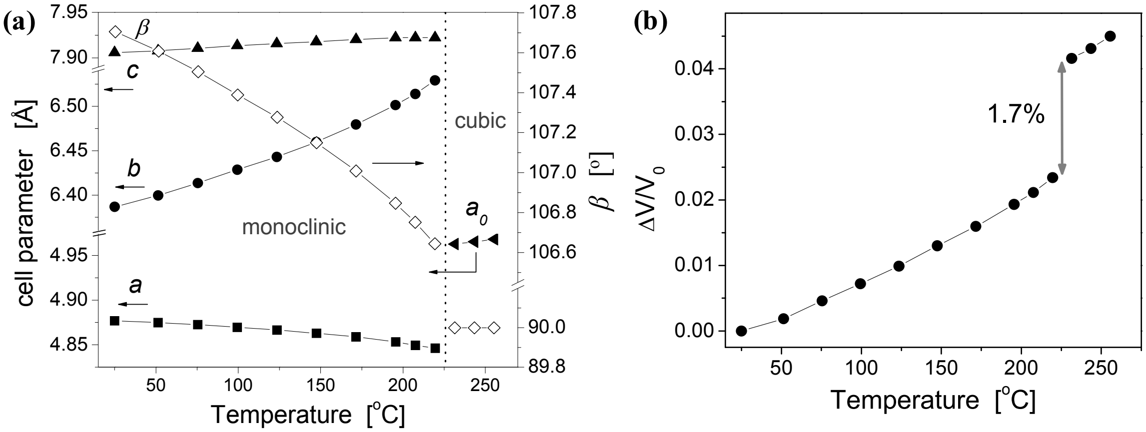

Figure 5.4 Thermal expansion of CsH_2PO_4 (25–256 ºC) determined by powder XRD: (a) Anisotropic thermal expansion in the monoclinic phase and isotropic thermal expansion in the cubic phase. Error bars are within the size of data markers. (b) Relative thermal expansion $\Delta V/V_0$ (V_0 taken at 25.0 ºC). The volume change during transformation is 1.7%.

Table 5.2 Thermal expansion parameters for CsH_2PO_4 corresponding to: $\Delta a/a_0 = A(T–T_0) + B(T–T_0)^2$, where $T_0 = 25.0$ ºC

Relative thermal expansion	$A \times 10^{-4}$ **[K^{-1}]**	$B \times 10^{-7}$ **[K^{-1}]**	T_{meas} **[ºC]**
$\Delta a/a_0$	–0.102(13)	–1.10(8)	25–220
$\Delta b/b_0$	0.662(30)	2.38(18)	25–220
$\Delta c/c_0$	0.145(8)	–0.167(50)	25–220
$\Delta \beta/\beta_0$	–0.303(11)	–1.00(7)	25–220
$\Delta V/V_0$ (monoclinic)	0.804(23)	1.99(14)	25–220
$\Delta V/V_0$ (cubic)	1.98(2)	0*	232–256

* For the cubic phase, relative volumetric thermal expansion is taken to be linear with temperature.

5.4.2 Conductivity and Phase Transformation Hysteresis

The hysteresis behavior of CsH_2PO_4 at a temperature ramp rate of 1 ºC min^{-1} is shown in Figure 5.5, in which the inverse of the real component of the impedance (effectively the conductance because the imaginary component of the impedance is small at this frequency) is presented as a function of temperature in Arrhenius form. The sharp transition behavior is immediately evident, with the superprotonic phase displaying a conductance that is three orders of magnitude higher than the paraelectric phase. As demonstrated in the figure, extrapolations from linear portions of the data were utilized to define the transition temperature, and, overall, the transition behavior was slightly more gradual on heating than on cooling, an effect observed for all compositions examined. For the measurement of CsH_2PO_4 shown in Figure 5.5, the superprotonic transition occurs at 227.9 ºC upon heating, whereas the reverse transformation occurs at 214.0 ºC. Repeated cycling (at 1 ºC min^{-1}) demonstrated highly reproducible behavior, both in terms of the magnitude of the conductance and the temperature of the transition (Figure 5.6). From an average over almost 20 cycles, the superprotonic transition of CsH_2PO_4 is found to be 227.6 ± 0.4 ºC on heating, consistent with previous studies[119–122] and 214.2 ± 0.8 ºC on cooling. For all compositions a slightly higher variability in the transition temperature was observed on cooling (± 0.4–0.8 ºC) than on heating (± 0.2–0.4 ºC).

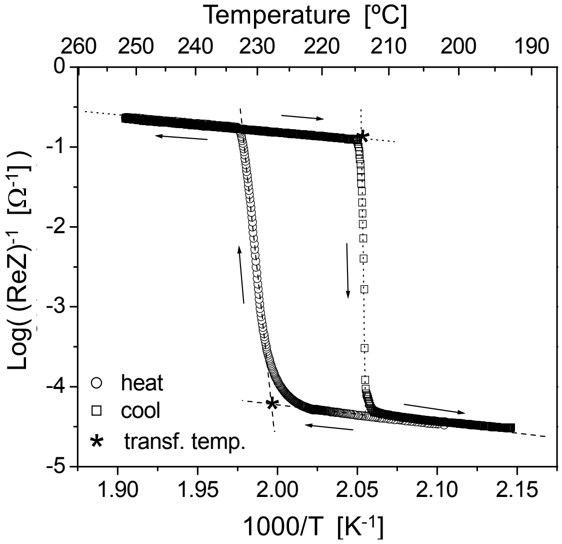

Figure 5.5 Arrhenius behavior of the proton conductivity of CsH_2PO_4 measured at a heating rate of 1 ºC min^{-1} under flowing N_2-H_2O gas (~ 0.5 atm H_2O). Arrows indicate heating and cooling cycles. The phase transition temperatures, denoted by *, are determined by the intersection of fitted lines to be 227.9 ºC on heating and 214.0 ºC on cooling.

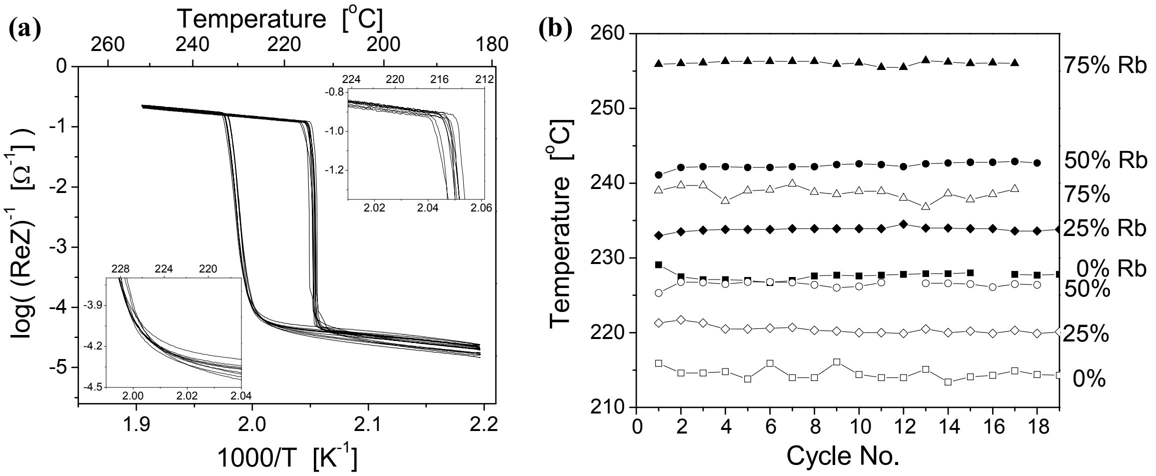

Figure 5.6 Reproducibility and stability of the $Cs_{1-x}Rb_xH_2PO_4$ system upon repeated temperature cycling at 1 ºC min^{-1} under flowing N_2-H_2O gas (~ 0.5 atm H_2O): (a) Conductivity behavior of CsH_2PO_4 and (b) transformation temperatures on heating (filled markers) and on cooling (open markers) demonstrate stability.

It is widely appreciated that finite heating rates can impact transformation temperatures, and ideally one extrapolates to a zero heating (or cooling) rate on the basis of measurements carried out at several different rates. Here, the transformation temperature on heating was found to be largely independent of heating rate for measurements at 0.1, 0.2, 0.5, and 1.0 ºC min^{-1} rates. In contrast, the transition on cooling displayed a somewhat erratic dependence on cooling rate. It is possible this behavior, along with the overall greater variability of the occurrence of the reverse transition even under a given cooling rate (Figure 5.6b), reflects a fundamental characteristic of the material behavior. Specifically, transformations on cooling between equilibrium phases are exothermic and local heat release may influence, for the $Cs_{1-x}Rb_xH_2PO_4$ system, the kinetics of transformation in an unpredictable manner. Given the difficulty in obtaining hysteresis values under zero heating rate conditions from an extrapolation procedure and the acceptable reproducibility of the results at a rate of 1 ºC min^{-1}, the data collected under this rate were used for additional analysis.

As summarized in the phase diagram presented in Figure 5.7a, the superprotonic transition temperature (onset on heating) increases with Rb content, from 227.6 ± 0.4 ºC for CsH_2PO_4 to 256.1 ± 0.3 ºC for $Cs_{0.25}Rb_{0.75}H_2PO_4$. Similarly, the hysteresis (the difference between the onset of the transition on heating and on cooling) also increases with Rb content (Figure 5.7b). However, the impact here is slight, with the hysteresis increasing from 13.4 ± 0.8 ºC for CsH_2PO_4 to only 17.4 ± 0.8 ºC for $Cs_{0.25}Rb_{0.75}H_2PO_4$.

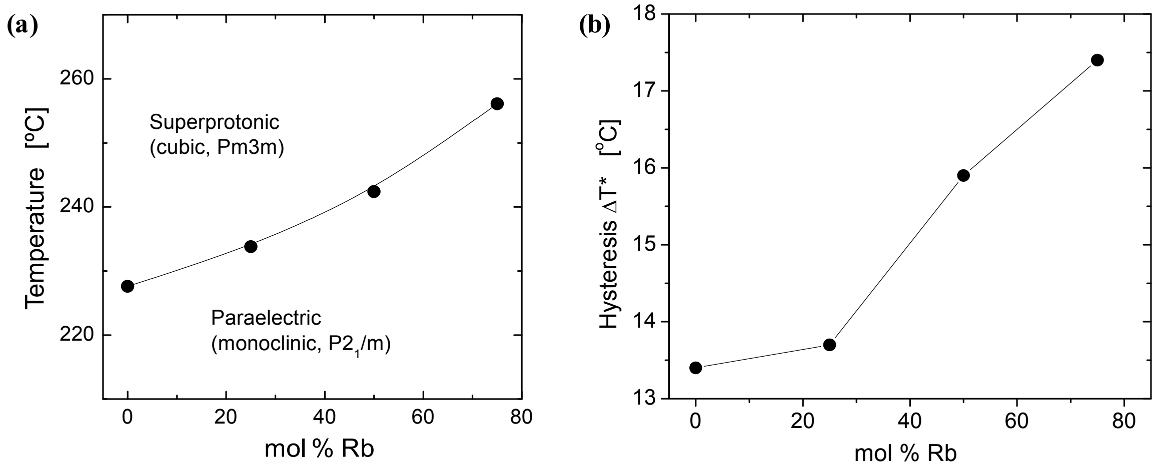

Figure 5.7 (a) Temperature-composition diagram for the $Cs_{1-x}Rb_xH_2PO_4$ system and (b) hysteresis width as a function of composition, as determined by impedance measurements at a heating rate of 1.0 °C min^{-1} under flow N_2-H_2O mixtures (~ 0.5–0.85 atm H_2O).

5.4.3 Eigenvalues and Correlation to Hysteresis

From the expression of $\mathbf{U_1}$ given in Equations (5.5)–(5.9), it is possible to obtain analytical expressions for the eigenvalues. Given the particular lattice parameters of the $Cs_{1-x}Rb_xH_2PO_4$ system, the ordered eigenvalues of the cubic-to-monoclinic transformation matrix yield a middle eigenvalue that depends only on two crystallographic parameters, b (low-temperature phase) and a_0 (high-temperature phase).

$$\lambda_2 = \frac{b}{a_0\sqrt{2}} \tag{5.11}$$

The computed dependence of λ_2 on Rb content,[19] is shown in Figure 5.8a. The data indicate that λ_2 decreases with Rb content from 0.932 for CsH_2PO_4 to 0.919 for $Cs_{0.5}Rb_{0.5}H_2PO_4$. Thus, while there is some sensitivity to composition, the range of λ_2 values encountered here ($\Delta\lambda_2 < 0.015$) is smaller than the previously studied ternary shape-memory alloy systems in which the eigenvalues could be readily manipulated from ~ 0.95 to 1.02.[110] The theory of martensite predicts that transformation hysteresis decreases as λ_2 approaches 1, implying in this case that the hysteresis should increase with Rb content. This is precisely what is observed (Figure 5.7b). The correlation between the hysteresis and the middle eigenvalue is more clearly depicted in Figure 5.8b. As the middle eigenvalue increases toward 1, indicating the superprotonic cubic phase becomes more compatible with the monoclinic phase, the hysteresis width decreases.

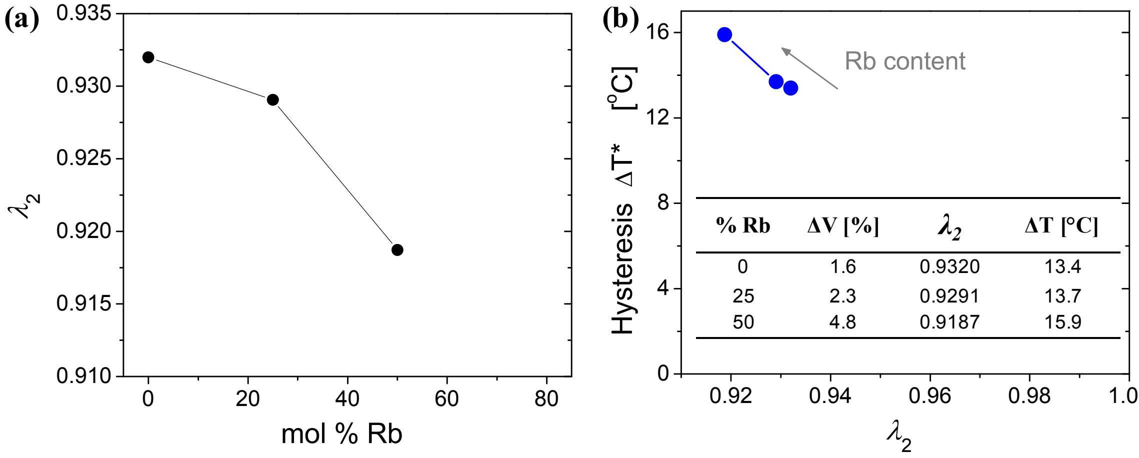

% Rb	ΔV [%]	λ_2	ΔT [°C]
0	1.6	0.9320	13.4
25	2.3	0.9291	13.7
50	4.8	0.9187	15.9

Figure 5.8 (a) Middle eigenvalue, λ_2, as a function of composition showing a decrease in λ_2 with Rb content and (b) hysteresis with as a function of the middle eigenvalue, λ_2, showing a decrease in hysteresis as λ_2 increases towards 1. Inset table shows values for the middle eigenvalue, phase transformation volume change (on heating) and hysteresis width.

The observed hysteresis widths for $Cs_{1-x}Rb_xH_2PO_4$ system are rather narrow (Figure 5.8b) given the fact that the middle eigenvalues are considerably far from 1. For example, previous studies of ternary shape-memory alloys revealed hysteresis widths as large as 63 ºC for a middle eigenvalue of ~ 0.96.[110] Such an observation may indicate that elastic compliance can allow otherwise incompatible phases to coexist and thus undercooling need not proceed to such great extents to induce the martensite transformation. (It is interesting to note that physical observations of the $Cs_{1-x}Rb_xH_2PO_4$

discs before and after testing indicate the plasticity of the high-temperature phase increase with Rb content.)

That the behavior of hysteresis with the middle eigenvalue is consistent with the theory of crystallographic compatibility indicates the theory is applicable to materials beyond shape-memory alloys and furthermore is a promising tool for studying additional solid acid compounds. It is important to note, however, that the observation of increasing hysteresis (and incompatibility between phases) with Rb incorporation implies that, Rb-containing compounds are not likely to replace CsH_2PO_4 as crack-free electrolytes for use in fuel cells.

5.5 Results and Discussion: Microstructure of CsH_2PO_4 and $CsHSO_4$

5.5.1 Microcrack Formation

SEM micrographs of single-crystal surfaces of CsH_2PO_4 and $CsHSO_4$ after heating to the high-temperature phase are shown in Figure 5.9. In CsH_2PO_4, cracks are clearly visible, varying in width and length and occurring with relatively high density, consistent with observations made for polycrystalline CsH_2PO_4 (Figure 3.2). Cracks in $CsHSO_4$ are narrow and barely visible.

Optical images of single crystals before and after heat treatment reveal the influence of cracking on the clarity of CsH_2PO_4 and $CsHSO_4$ crystals (Figure 5.10). The as-grown CsH_2PO_4 crystal was transparent, with some visible defects due to inclusions of solution, but was almost completely opaque after heat treatment and was comprised of many facets (Figure 5.10a). The $CsHSO_4$ single crystal was also transparent initially, although the clarity of the crystal was not as well-captured as that for CsH_2PO_4 because of the presence of fine crystallites/precipitates on the surface. Even so, the $CsHSO_4$ crystal exhibited a less dramatic change in its clarity, appearing hazy but retaining some transparency after heat treatment (Figure 5.10b). The observation of higher clarity in $CsHSO_4$ is consistent with lower crack densities and the smaller phase transformation hysteresis width of 5.2 ºC[19] compared to 13.4 ºC for CsH_2PO_4.

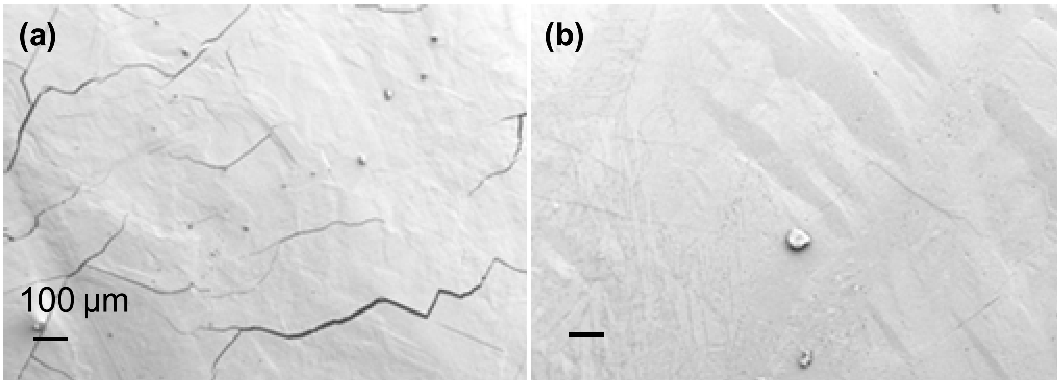

Figure 5.9 SEM micrographs of polished surfaces of (a) CsH_2PO_4 and (b) $CsHSO_4$ single crystals, taken after heat treatment at temperatures above the phase transition temperature (235 ºC and 155 ºC, respectively).

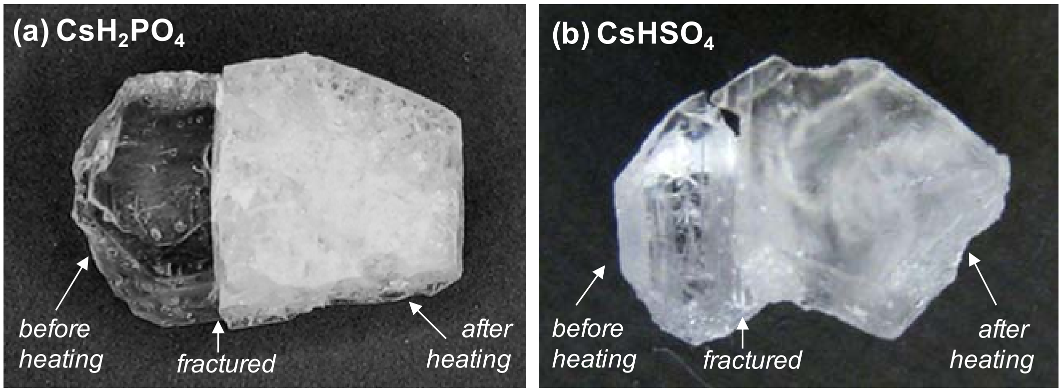

Figure 5.10 Optical images of two halves of a fractured single crystal of (a) CsH_2PO_4 and (b) $CsHSO_4$. The right half for each crystal was heat-treated at above its phase transition temperature.

5.5.2 *Microstructure of Single-crystal Surfaces*

Micrographs of single-crystal CsH_2PO_4 surfaces, both polished (Figure 5.11a) and fractured (Figure 5.12a), show that surfaces were smooth before heat treatment. In the case of polished crystals (Figure 5.11a), streaks running diagonally in the image are visible to the uni-directional polishing of the crystals. As-fractured crystal surfaces contained crystal steps in the plane of the image but were smooth otherwise (Figure 5.12a). For samples prepared by both methods, changes in the CsH_2PO_4 surface after heating were clearly visible. Figure 5.11(b–c) and Figure 5.12(b–c) are SEM images of polished and fractured surfaces, respectively, showing that the surfaces appeared faceted after heat treatment. Polishing streaks visible in Figure 5.11 are relatively easy to distinguish from features that appeared due to heat treatment. However, without any noticeable patterning or symmetry, it is unclear if these features correspond to twins of monoclinic phase. Higher magnification images generally revealed little additional information, with the exception of Figure 5.13 collected for a fractured crystal. In this image, patterning at the micron-scale is visible, and an angle of ~ 45º can be extracted for the two sets of patterns. It is interesting to note that the surface of the crystal appeared roughened with uniformly distributed sub-micron particulates. The formation of CsH_2PO_4 particles on the surface of the fractured crystal likely occurred at superprotonic temperatures at which CsH_2PO_4 is relatively mobile.

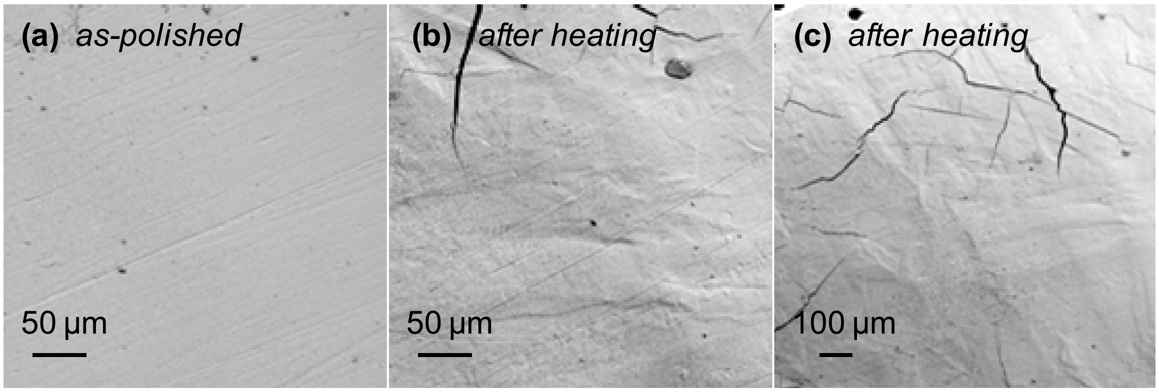

Figure 5.11 SEM micrographs of a polished surface of a CsH_2PO_4 single crystal (a) before and (c) after heating to 235 ºC in synthetic air with ~ 0.35 atm H_2O.

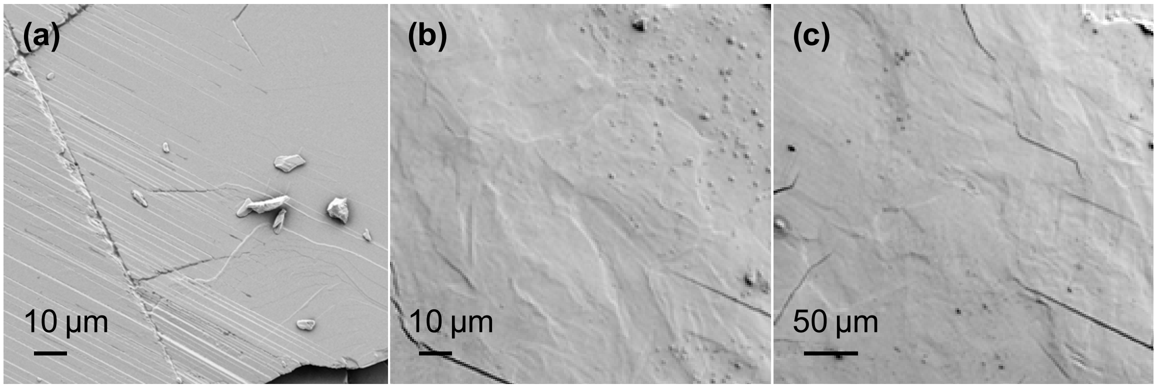

Figure 5.12 SEM micrographs of a fractured surface of a CsH_2PO_4 single crystal (a) before and (c) after heating to 235 ºC in synthetic air with ~ 0.35 atm H_2O.

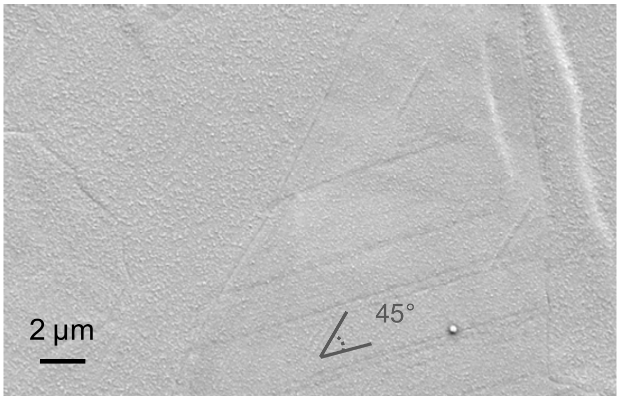

Figure 5.13 SEM micrograph of a fractured CsH_2PO_4 single crystal after heat treatment at 235 ºC under flowing synthetic air with ~ 0.35 atm H_2O. Features appear to be twins, with internal twins at an angle of 45º to larger twins.

$CsHSO_4$, on the other hand, formed twinned regions that were easily visible regardless of the method used to prepare the single-crystal surface. Untreated, as-grown $CsHSO_4$ single-crystal surfaces before and after heat treatment at superprotonic conditions are shown in Figure 5.14a and Figure 5.14(b–c), respectively. The surface of the as-grown crystal was smooth in most regions. Some contoured crystal steps are evident in Figure 5.14a; elsewhere, small crystallites had grown from the surface, characteristic of the surfaces of solid acid crystals taken directly out of solution. Overall, the crystal was considered sufficiently smooth for use in microstructures studies. After heat treatment, patterning of the surface was clearly visible; triangular-shaped features, with widths of 10–50 µm, emerged from the surface (Figure 5.14c). The edges of these features ran in the same direction, diagonally through the image. The surface also appeared to be roughened at a smaller length scale (Figure 5.14b); ignoring these imperfections, some internal twinning on the order of ~ 1 µm is visible within the larger ~ 10 µm twins.

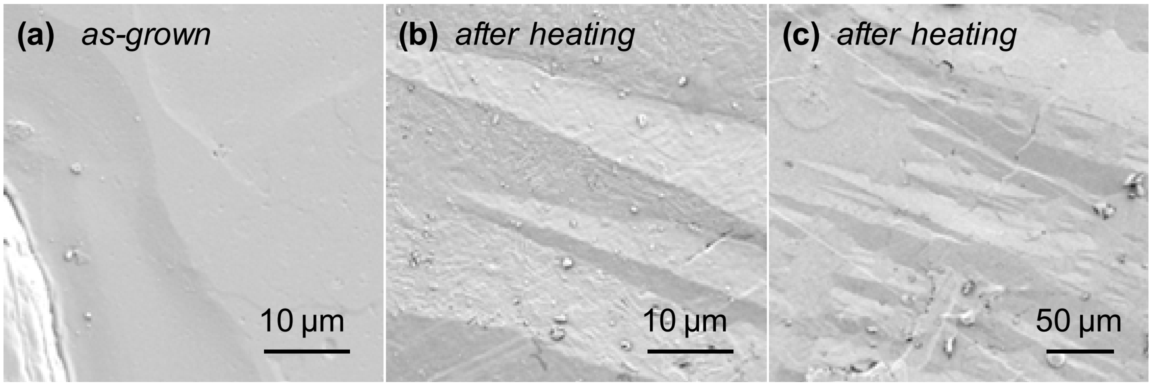

Figure 5.14 SEM micrographs of the surface of an as-grown $CsHSO_4$ single crystal (a) before and (b,c) after heating to 155 ºC in ambient air.

The complexity of the microstructure is more clearly shown for polished crystals (Figure 5.15). Crystal surfaces before testing, Figure 5.15(a–c), revealed polishing streaks but were otherwise relatively featureless. The microstructure of crystal after heat treatment, Figure 5.15(d–f), can be assessed easily due to the high contrast in the image, the origin of which remains unknown. Visible in these three images are features of several scales, from hundreds of microns down to under ten microns in size, the latter appearing to be internal twins within the former (Figure 5.15f). Closer examination revealed that the large twins intersect at angles of 95 (or 85º), as noted in the Figure 5.15e.

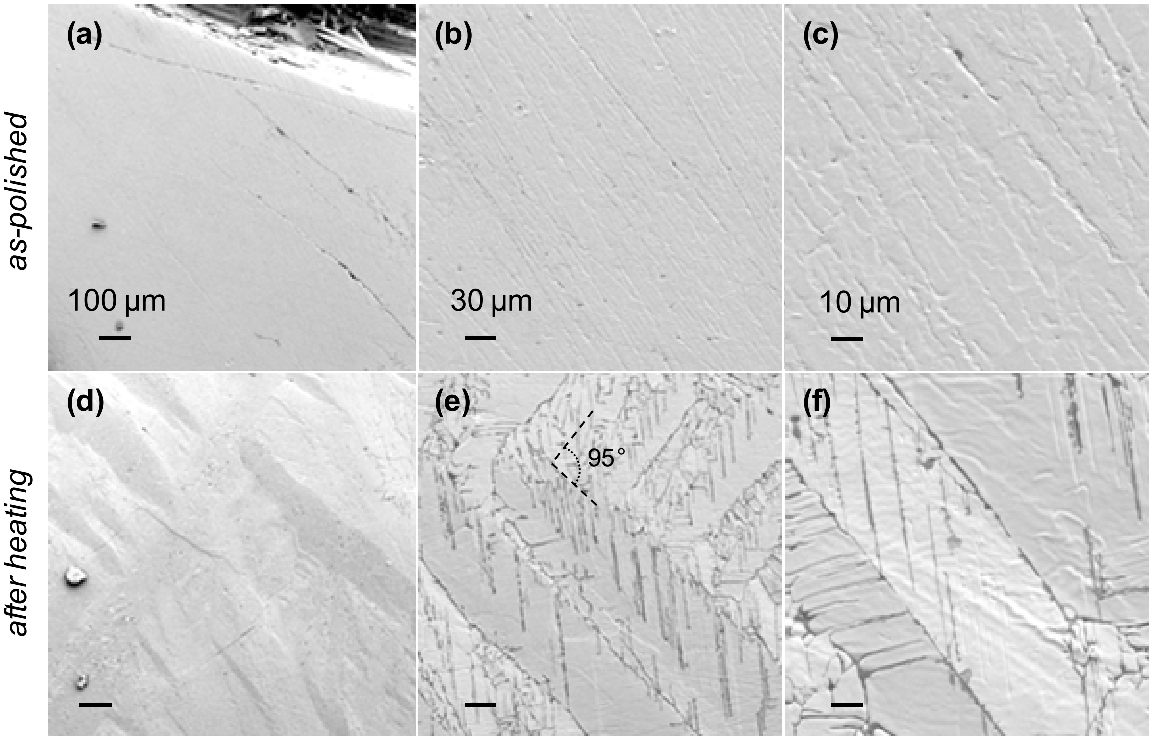

Figure 5.15 SEM micrographs of a polished surface of a $CsHSO_4$ single crystal (a–c) before and (d–f) after heating to 155 ºC in ambient air.

5.5.3 In situ Imaging of $CsHSO_4$

A more reliable assessment of the microstructure can be obtained by topography images measured by AFM. Although the maximum *x-y* range of ~ 35 μm for AFM prevented the mapping of the larger features which could be observed by SEM, AFM enabled the capture of finer features. Shown in Figure 5.16 are planar and three-dimensional representations of the surfaces of two different single crystals obtained by fracturing. The features presented in these images are considered representative of those found using AFM in general. The features in all three images were qualitatively similar and revealed twinning with well-defined patterns. The larger feature sizes on the order of 10 μm are consistent with those in Figure 5.14 and Figure 5.15. Finer features which appeared as steps ~ 1 μm in size were also visible in all three images in Figure 5.16.

From Figure 5.16(b–c), for which the intersections of twins are visible, an angle of ~ 95° (or 85°) was extracted; this angle is consistent with observations made by SEM (Figure 5.15e). Topographical profile analysis of the twins (not shown) provided the angles at which the two variants met, out of the x-y plane, to form an apex (right column of Figure 5.16). From profile analysis of the images in Figure 5.16, we determined this angle to be 170°. This value is twice that for the in-plane angles of ~ 85° (or, ~ 95°). The measured angles of select features are marked in the figure.

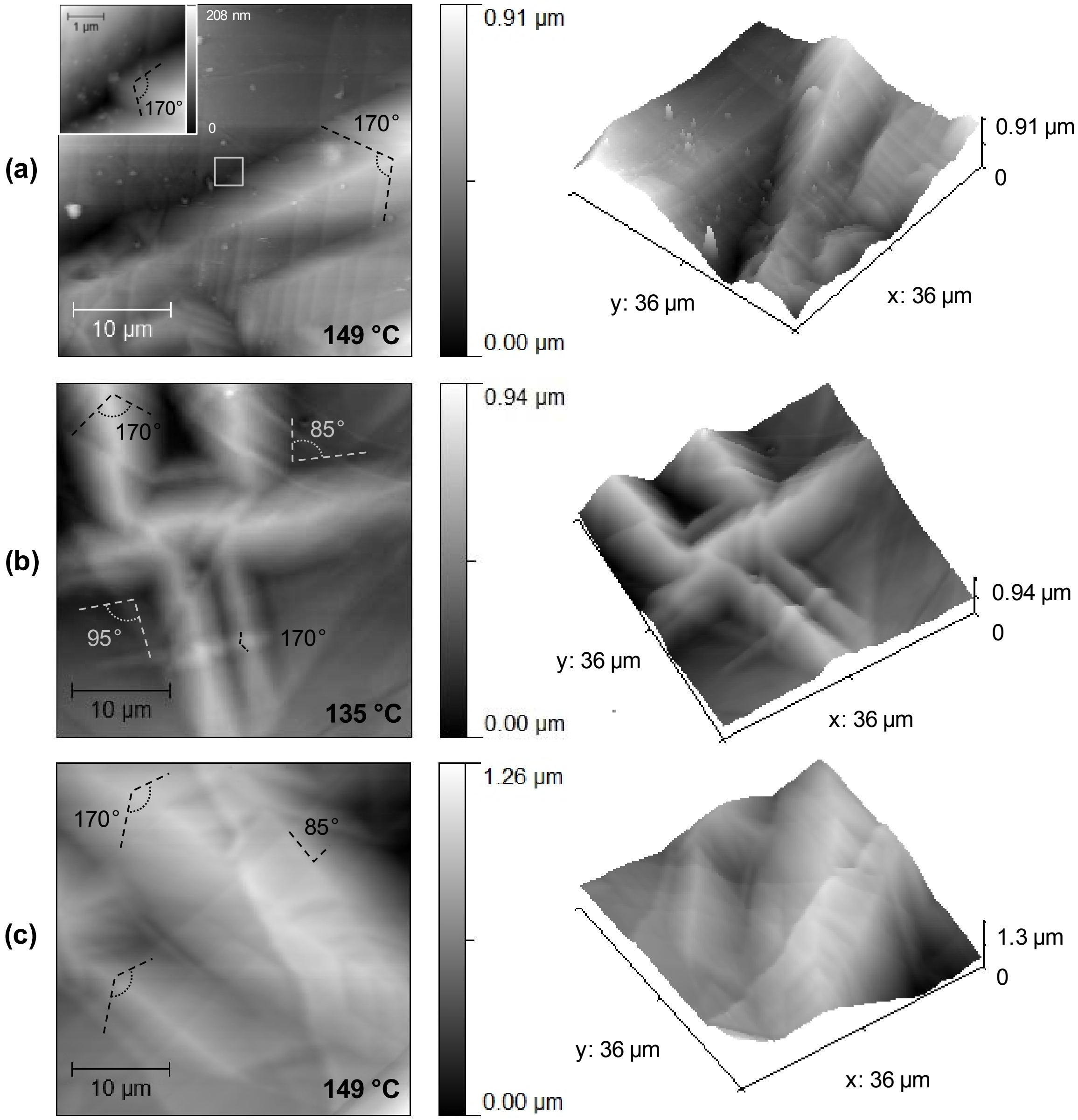

Figure 5.16 Topography of a $CsHSO_4$ single-crystal surface obtained by fracturing. Images were acquired in synthetic air with 0.03 atm H_2O at superprotonic temperatures of (a) 149 ºC for one crystal and (b) 135 ºC and (c) 149 ºC for a second crystal. Horizontal features in the 2D representations are scan lines and not topographical features. In the 3D representations, *z* is not to scale with *x*/*y*.

The observation of twins at high temperature at which the high-symmetry tetragonal phase of $CsHSO_4$ is expected to exist is somewhat surprising. The image in Figure 5.16(a), which clearly revealed twinning, was taken after five hours at temperatures between 145 and 149 ºC, above the superprotonic transition temperature of ~ 141 ºC. For the single crystal in Figure 5.16(b–c), twins were visible both before and after transition, with the different features being imaged being due to thermal expansion and sample movement as the temperature was heated from 135 to 149 ºC.

We further explored this phenomenon by mapping the topography of a fractured $CsHSO_4$ crystal as it was heated and cooled through the phase transition (Figure 5.17). For this particular crystal, the as-fractured surface revealed contoured steps running through what appeared to be grain boundaries. As the temperature approached the phase transition temperature of ~ 141 ºC, a "crease" appeared at the left-hand side of the image (Figure 5.17b) and remained visible, albeit less defined, even at 145 ºC (Figure 5.17d). The apparent "smoothing" of this feature at higher temperatures could be indicative of the transformation of $CsHSO_4$ to the high-temperature tetragonal phase, or alternatively, an artifact of poor image quality due to the plasticity of the superprotonic phase and/or contamination of the AFM probe. From topographical profile analysis, the crease has a slight rise from the x-y plane, with an apex angle of 177º, slightly larger than the value of 170º determined above. This deviation is a likely a consequence of the noise in the images, making accurate determination of the angle difficult.

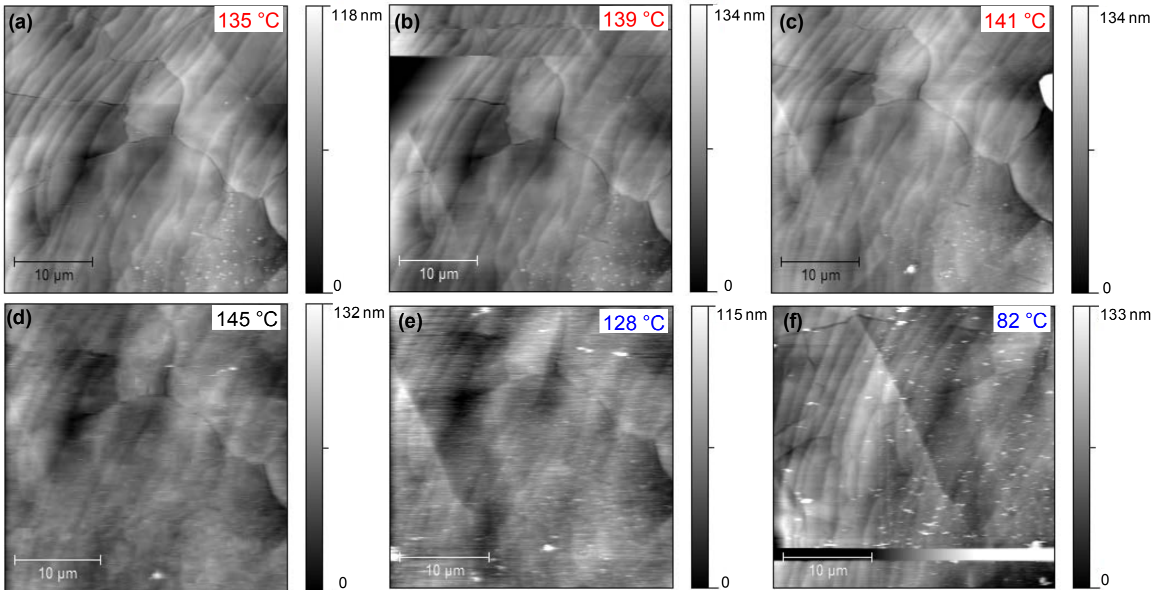

Figure 5.17 Topography of a CsHSO4 single-crystal surface obtained by fracturing, examined as a function of temperature. On heating (a–c), a feature appeared on the left-hand side of the image. The feature was less prominent at the maximum temperature (d), but then reappeared on cooling (e–f). Small white spots in (e) and (f) are due to either a damaged sample or a contaminated AFM probe.

Twinning is expected to occur on heating and cooling through the phase transition, that is, at any condition in which both the low-temperature (monoclinic) and high-temperature (tetragonal) phases co-exist. The observation of twinning in the superprotonic (austenite) phase may be a consequence of a temperature gradient which exists across the single crystal such that the surface temperature of the crystal is lower than that at the AFM hotplate. Thus, despite high setpoint temperatures, 10–20 ºC in excess of the phase transition temperature of 141 ºC, the crystal surface may not have been completely transformed. Another possible explanation for the existence of twins at high temperatures can be explained by arguments of crystallographic compatibility, that is, the strain existing between the monoclinic and cubic phases during transformation prevents the martensite phase from transforming. In the case of $CsHSO_4$, it is unclear whether such a phenomenon can exist. Because of the plasticity of the superprotonic, tetragonal phase of $CsHSO_4$,[17, 19, 56] the austenite phase may be able to accommodate strain present in the system. To address these issues, additional in situ studies of twinning are required. Capturing twinning as a function of temperature is non-trivial due to the limited scan range in AFM. As shown in previous SEM micrographs (Figure 5.14 and Figure 5.15), twinned regions can be dispersed, and thus, finding a region of a single crystal that will twin on heating is not guaranteed.

5.6 Summary and Outlook

The phase transformation behavior of the solid acid solution series, $Cs_{1-x}Rb_xH_2PO_4$, as determined by AC impedance measurements, was explored with respect to the principles of crystallographic compatibility between phases. The hysteresis of $Cs_{1-x}Rb_xH_2PO_4$ was found to increase with Rb content, from ~ 13.4 ºC for the end-member CsH_2PO_4 to ~ 17.4 ºC for x = 0.75. The middle eigenvalues varied from 0.932 to 0.919 for x = 0 to 0.50. The increase in the hysteresis width and the corresponding decrease in λ_2 (away from unity) are consistent with the theory of crystallographic compatibility. However, the broadening of the hysteresis with Rb incorporation implies that we cannot minimize cracking of the electrolyte by Rb substitution, and the end-member, CsH_2PO_4, still remains the electrolyte of choice for solid acid fuel cells (and electrochemical studies).

The physical properties of CsH_2PO_4 and $CsHSO_4$ single crystals correlated well with their measured hysteresis widths. $CsHSO_4$ (~ 5.2 ºC hysteresis, λ_2 = 1.010[19]) displayed a far lower crack density than CsH_2PO_4 (~ 13.4 ºC hysteresis, λ_2 = 0.932) when taken through the phase transition. Although $CsHSO_4$ is not a practical fuel cell electrolyte due to instability under reducing conditions,[56] $CsHSO_4$ may prove valuable as a substrate for fundamental cathode studies due to its low crack density and its relative stability with respect to dehydration. Microstructure changes due to the superprotonic phase transition were observed for both crystals, but twinned regions were not easily observable in CsH_2PO_4. Further exploration of the orientation of twinned domains in $CsHSO_4$ is required, specifically, the existence of frequently occurring angles of 170º and 85º and, more curiously, the persistence of martensite twins at temperatures above the phase transition temperature.

Although we have demonstrated that the hysteresis behavior of $Cs_{1-x}Rb_xH_2PO_4$ and $CsHSO_4$ can be explained by the theory of crystallographic compatibility, we have not ruled out effects of strain due to differences in the volume of the two phases. In the case of the $Cs_{1-x}Rb_xH_2PO_4$ solid solution series, as more Rb was incorporated, the volume change at transition also increased from 1.7% to 4.8% on heating.[19] Similarly, the lower hysteresis width of $CsHSO_4$ relative to $Cs_{1-x}Rb_xH_2PO_4$ can be explained by the lower volume change of $CsHSO_4$ across the phase transition (~ 0.5%) compared to that for the $Cs_{1-x}Rb_xH_2PO_4$ series. $Rb_3H(SeO_4)_2$ is presently the only solid acid compound we have examined in the context of crystallographic compatibility that, when compared to CsH_2PO_4 and $CsHSO_4$, displays lower phase transformation hysteresis, a computed λ_2 value closer to unity, and a *larger* volume change across the phase transition. The hysteresis width and its correlation with λ_2 and volume change are summarized in Figure 5.18. The middle eigenvalues for CsH_2PO_4, $CsHSO_4$, and $Rb_3H(SeO_4)_2$ were found to be 0.932, 1.010, and 1.007 corresponding to hysteresis widths of 13.4, 5.2,[19] and 2 ºC,[108] respectively. A plot of hysteresis against λ_2 (Figure 5.18a) shows a lowering of the hysteresis as the eigenvalue approaches unity from both sides, consistent with theory. However, while CsH_2PO_4 and $CsHSO_4$ exhibited volume changes of 1.7 and 0.5%, respectively, on heating, $Rb_3H(SeO_4)_2$ exhibits a large negative volume change of –2.7%. Consequently, a plot of hysteresis against the phase transformation volume change (Figure 5.18b) shows $Rb_3H(SeO_4)_2$ falling off the trend, implying that strain existing between the austenite and martensite phases during transformation does not originate from a volume difference between the two. The correlation of the hysteresis with the middle eigenvalue, despite the differing crystal transformations (i.e., monoclinic-to-cubic, monoclinic-to-tetragonal, and monoclinic-to-trigonal for CsH_2PO_4, $CsHSO_4$ and $Rb_3H(SeO_4)_2$, respectively), is an indication of the widespread applicability of the theory to solid acid systems.

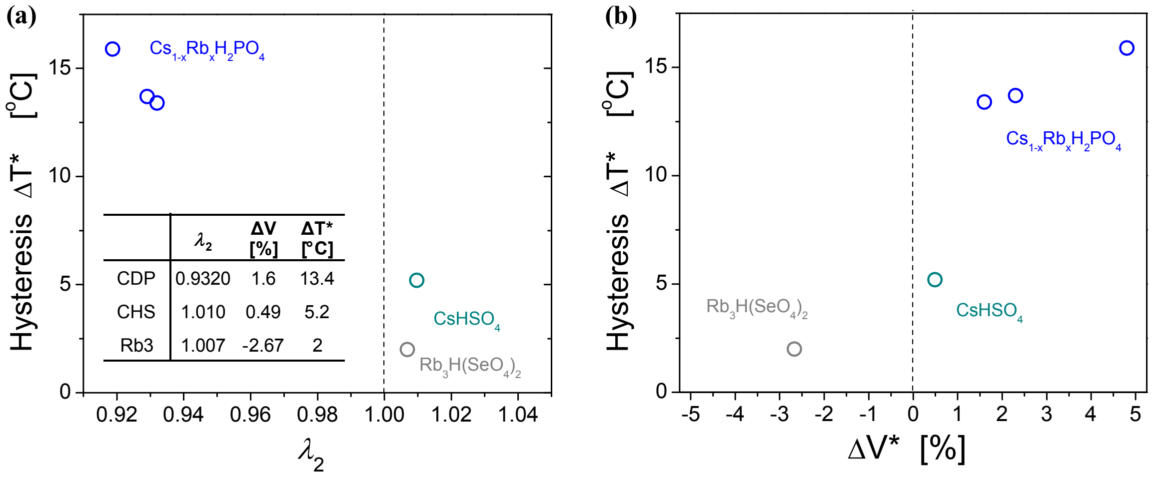

	λ_2	ΔV [%]	ΔT* [°C]
CDP	0.9320	1.6	13.4
CHS	1.010	0.49	5.2
Rb3	1.007	-2.67	2

Figure 5.18 Plot of superprotonic phase transition hysteresis as a function of (a) the middle eigenvalue, λ_2 and (b) the phase transformation volume change (on heating) for three classes of solid acid compounds.